DISSERTATIONES CHIMICAE UNIVERSITATIS TARTUENSIS
93

DISSERTATIONES CHIMICAE UNIVERSITATIS TARTUENSIS
93

TAVO ROMANN

Preparation and surface modification of bismuth thin film, porous, and microelectrodes

TARTU UNIVERSITY
PRESS

Institute of Chemistry, Faculty of Science and Technology, University of Tartu, Estonia

Dissertation is accepted for the commencement of the Degree of Doctor of Philosophy in Chemistry on May 3th, 2010 by the Council of Institute of Chemistry, University of Tartu.

Supervisor: Prof. Enn Lust, University of Tartu

Opponents: Prof. Kyösti Kontturi,
Helsinki University of Technology, Finland

Prof. Andres Öpik,
Tallinn University of Technology, Estonia

Commencement: June 21th, 2010, Ravila 14A (Chemicum), room 1021, 09:30

ISSN 1406–0299
ISBN 978–9949–19–390–5 (trükis)
ISBN 978–9949–19–391–2 (PDF)

Tartu Ülikooli Kirjastus
www.tyk.ee
Tellimuse nr 259

CONTENTS

1. LIST OF ORIGINAL PUBLICATIONS

I. **T. Romann**, E. Lust, Electrochemical properties of porous bismuth electrodes, Electrochim. Acta, doi:10.1016/j.electacta.2010.05.012 (accepted, in press).

II. **T. Romann**, E. Anderson, S. Kallip, H. Mändar, L. Matisen, E. Lust, Electroless deposition of bismuth on Si(111) wafer from hydrogen fluoride solutions, Thin Solid Films 518 (2010) 3690.

III. **T. Romann**, M. Väärtnõu, A. Jänes, E. Lust, In situ infrared spectroscopic characterization of a bismuth-ethanol interface, Electrochim. Acta 53 (2008) 8166.

IV. **T. Romann**, S. Kallip, V. Sammelselg, E. Lust, Bismuth microelectrode system with in situ renewable surface for electroanalysis and adsorption studies, Electrochem. Comm. 10 (2008) 1008.

V. **T. Romann**, V. Grozovski, E. Lust, Formation of the bismuth thiolate compound layer on bismuth surface, Electrochem. Comm. 9 (2007) 2507.

VI. **T. Romann**, K. Lust, E. Lust, Adsorption of 1,6-hexanediol on Bi single crystal electrodes, Electrochim. Acta 52 (2007) 2612.

Author's contribution:

Performed all electrochemical measurements and analysis of data. Participated in preparation of all manuscripts. In addition:

Paper I: Performed electron microscopy measurements.
Paper II: Developed thin film preparation method. Participated in AFM, Raman and photoluminescence measurements.
Paper III: Constructed the measurement cell and performed infrared spectroscopy measurements.
Paper IV: Constructed microelectrodes and the measurement cell.
Paper V: Performed optical microscopy and infrared spectroscopy measurements as well as thiolate synthesis.

2. ABBREVIATIONS AND SYMBOLS

A	constant phase element coefficient
ac	alternating current
AFM	atomic force microscopy
ATR	attenuated total reflectance
B13DT	Benzene-1,3-dithiol
BiCCE	bismuth cleaved capillary electrode
c	concentration
c^0	bulk concentration
C	capacitance
C_a	faradaic adsorption capacitance
C_{dl}	double layer capacitance
CPE	constant phase element
CPE_R	constant phase element with exponent value close to 0
C_s	series capacitance
CV	cyclic voltammetry
D	diffusion coefficient
DSC	differential scanning calorimetry
E	electrode potential
EC	equivalent circuit
EtOH	ethanol
f	ac frequency
F	Faraday's constant
FDT	3,3,4,4,5,5,6,6,7,7,8,8,9,9,10,10,10-heptadecafluoro-1-decanethiol
HD	1,6-hexanediol
HER	hydrogen evolution reaction
i	current density
IPR	ideally polarizable region
i_0	exchange current density
j	imaginary unit ($\sqrt{-1}$)
k_s	electron transfer rate constant
L	effective diffusion layer thickness
MCT	mercury-cadmium-telluride (highly sensitive infrared detector)
MHDA	16-mercaptohexadecanoic acid
n	number of electrons

OCP	open circuit potential
ODIT	1,8-octanedithiol
ODT	1-octadecanethiol
OM	optical microscopy
ox	oxidized form
P_{BiH3}	bismuth hydride partial pressure
pzc	potential of zero charge
q	charge
R	roughness factor
R_D	limiting diffusion resistance
red	reduced form
R_{ct}	charge transfer resistance
R_a	adsorption resistance
S	surface area of electrode
SAXS	small-angle X-ray scattering
SEIRAS	surface enhanced infrared absorption spectroscopy
SEM	scanning electron microscopy
SNIFTIRS	subtractively normalized interfacial Fourier transform infrared spectroscopy
STEAR	1-octadecanoic acid
STM	scanning tunnelling microscopy
T	temperature
t	time
x	distance from the electrode
XRD	X-ray diffraction
XPS	X-ray photoelectron spectroscopy
Z	summary impedance
Z_W	Warburg-like diffusion impedance
Z'	real part of impedance
Z''	imaginary part of impedance
α	CPE fractional exponent
α_t	transfer coefficient
α_w	Warburg diffusion impedance fractional exponent
Φ	phase angle
θ	contact angle
Δ^2	weighted sum of the squares
τ_{max}	characteristic relaxation time

σ	mass-transfer coefficient
χ^2	the square of the standard deviation between the original data and the calculated spectrum
ω	angular frequency (equal to $2\pi f$)
v	potential scan rate

3. INTRODUCTION

Electroanalytical chemistry needs systems like dropping mercury electrode, because it has an easily renewable smooth surface with the connection of wide potential region of ideal polarizability, but it is loosing interest because of the high toxicity of Hg [1]. Instead, in this work [1–11] we used bismuth that behaves electrochemically similarly to the mercury electrode except oxidizing slightly more easily [12–15]. Bismuth is non-toxic metal and the solid surface has some advantages over liquid interface: it is not so sensitive to the mechanical vibration and solution movement (thus high solution flow rates can be used) and the cleavage of the solid Bi electrode is quicker than the Hg drop removal procedure opening new possibilities for studying electrochemical surface processes. Also, the solid bismuth surface can be studied by several modern methods, including scanning tunnelling microscopy (STM) [16,17] and in situ infrared reflectance spectroscopy [6], more easily than the liquid mercury surface. The bismuth film electrode has been attracting increasing attention in the field of analysis of some trace metal cations like anodic stripping analysis of Pb, Cd, Zn, Tl, In, Cu and Sn, adsorptive stripping analysis of Ni, Co, U and Cr [12, 18–20] and also for direct cathodic electrochemical detection of organic compounds [21–22]. This work reports the construction of the renewable surface bismuth microelectrode system, usable in electrochemical analysis, double layer and adsorption studies [1–2].

Semimetallic bismuth has some unusual electronic properties that results from Bi highly anisotropic Fermi surface, large Fermi wavelength, low charge carrier concentrations, small effective carrier mass, and long carrier mean free path [23–33]. Thus, thin Bi films, nanowires, and nanoparticles have been extensively investigated for quantum transport and quantum-confinement effects [23–33]. For Bi films, semimetal-to-semiconductor transition is expected to take place at film thicknesses from 23 to 32 nm [23,24]. Interesting electrical properties have been reported for thin Bi films, like change of conduction mechanism from p type for Bi(111) film to n type for Bi(110) film (the indexes for rhombohedral cell setting are used throughout this paper), and oscillating resistivity dependence on the film thickness [23,25,27]. Large magnetoresistance effects of the Bi films suggest that Bi could be used for magnetic field sensors [23–33]. Because of the strong spin-orbit splitting effect, Bi interfaces could be promising candidates for the construction of spin sources or filters [23]. We prepared thin Bi films and porous Bi materials that could find applications in nanoelectronics [2,4].

Self-assembled thiol monolayers on gold have been studied extensively and various interesting nanotechnological applications have been demonstrated [34–35]. Thiols also interact with other metal surfaces and thiol monolayers have been detected on Ag, Cu, Pt and other metal electrodes [34–38]. In this work, bismuth was modified with different thiols and the properties of the surface layers formed have been characterised by various methods [3,5,8]. In

addition, the synthesis method of formed new bismuth thiolates has been worked out.

The main aim of this work was to develop methods for preparation and surface modification of bismuth electrodes and to propose some practical uses for these. The properties of prepared Bi single crystals, microelectrodes, thin films, porous surfaces and thiol modified surfaces were studied mainly with cyclic voltammetry, electrochemical impedance and in situ infrared spectroscopy as well as surface imaging techniques – scanning electron microscopy (SEM), optical microscopy (OM) and atomic force microscopy (AFM). The collected information [1–11] also gives some new knowledge about the electrochemical behaviour of Bi.

4. LITERATURE OVERVIEW AND INTERPRETATION OF DATA

4.1. Cyclic Voltammetry (CV)

In cyclic voltammetry method, the working electrode potential E is changed with constant speed $v = dE / dt$, and the resulting current is recorded and analyzed. For a simple redox reaction, it is possible to express the temporal development of the current through the electrode:

$$i = nFD\left(\frac{\partial c_{red}}{\partial x}\right)_{x=0} \tag{4.1.1}$$

where i is current density, n is number of electrons, D is diffusion coefficient, $\delta c_{red}/\delta x$ is the reduced species concentration gradient [39–41]. For a reversible one electron transfer process ($n = 1$) when $D_{ox} = D_{red}$ (ox – oxidized form, red – reduced form), the difference between oxidation and reduction peaks should be 58 mV [39–41].

The form of the curve is qualitatively explained as follows: at the beginning of the experiment, essentially no current flows since we start from an equilibrium situation. Scanning potential induces a change in c_{ox}/c_{red} at $x = 0$. Red is converted into ox at the electrode, resulting in a current. The concentration of red is depleted in the immediate vicinity of the electrode surface, while the concentration of ox increases. Thus, red diffuses towards the electrode, while ox diffuses to the bulk. Further increase of E causes a decrease of c_{red} and increase of i [39–41]. Qualitatively, the peak current density i_p is given by Randles-Sevčik equation [39]

$$i_p = (2.69 * 10^5) n^{3/2} c_{red}^0 \sqrt{v D_{red}} \tag{4.1.2}$$

The constant in equation (4.1.2) corresponds to temperature of 298 K. At high potential scan rates v, the diffusion-controlled current is increased over that for lower scan rates. This is due to the fact that the concentration gradient and the flux of reactant to the electrode increase with increasing v [39–41].

The exact shape and quantitative features of the voltammograms depend on a variety of parameters, e.g. the adsorption isotherm followed, the surface concentration of the redox species, or on the presence or absence of intermolecular forces between the adsorbed molecules [39].

A finite rate constant k_s of the electron transfer derives from Butler-Volmeri equation

$$i = i_0 \left\{ \exp\left[\frac{-\alpha_t nF}{RT}(E - E_0) \right] - \exp\left[\frac{(1-\alpha_t)nF}{RT}(E - E_0) \right] \right\}, \quad (4.1.3)$$

where

$$i_0 = nFk_s c_{red}^0 \quad (4.1.4)$$

is the exchange current density (i_0 ja k_s is defined at $E = E^0$) and α_t is the transfer coefficient [39]. Depending on the relative magnitudes of D and k_s, we move from a situation in which diffusion control predominates (reversible case) through a mixed-control regime (quasi-reversible) to a situation in which the rate of electron transfer controls the overall reaction (large D, small k_s, irreversible case) [39–41].

Bismuth electrode oxidation to non-conducting solid Bi_2O_3 and reduction back to metallic Bi is a quasi-reversible process as shown in Fig. 1 [6]. The thickness of formed Bi_2O_3, calculated from the peak area, is hundreds of monolayers. Therefore, the noticeable roughening takes place during potential cycle, shown in Fig. 1.

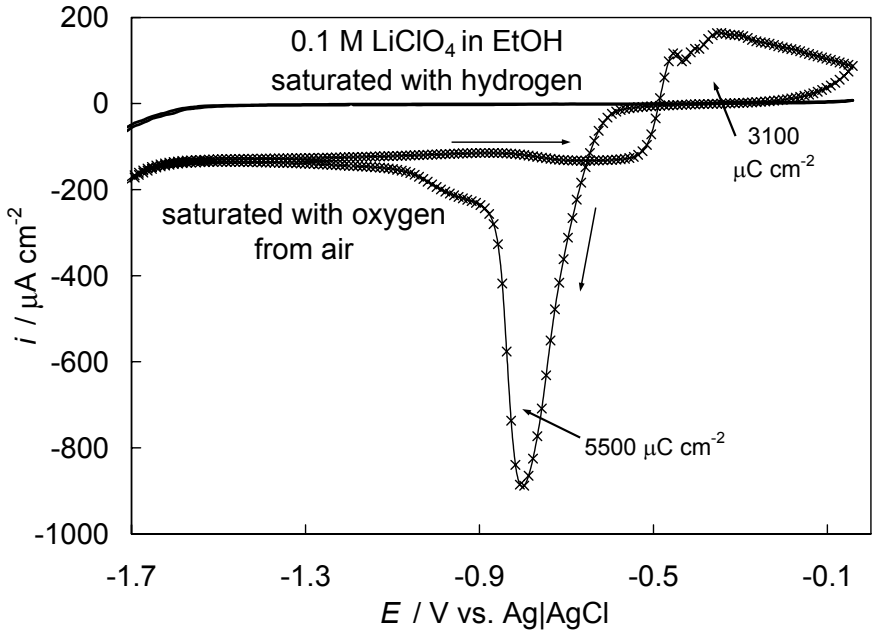

Figure 1. CVs (10 mV s^{-1}) for Bi(001) electrode in the absence and presence of dissolved oxygen.

Hydrogen evolution reaction (HER) can proceed by two different mechanisms: through hydrated proton in acidic solution and at more cathodic potentials by direct water decomposition in neutral solutions [11]. For Bi electrode, these processes are both completely irreversible, because there are no positive oxidation peaks in CVs (Fig. 2).

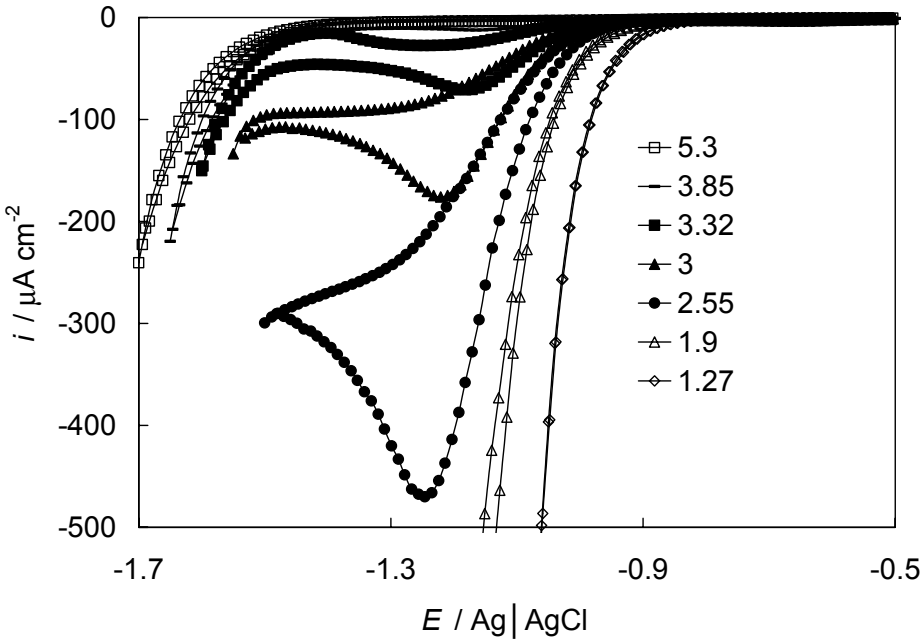

Figure 2. CVs for Bi(001) electrode in 0.1 M $LiClO_4$ aqueous solution with $HClO_4$ addition (pH values are given in graph) at scan rate of 10 mV s^{-1}.

4.1.1 Capacitive current peaks

Double layer charging adds to the *i*,*E* curve in the most simple case a constant current that dominates at high potential scan rates. In this study, the CV method was tested for 1,6-hexanediol (HD), n-pentanol, and pyridine aqueous solutions, and at higher potential scan rates (v > 0.1 V s^{-1}) the reversible adsorption and desorption peaks were observed [9,10].

For 0.04 M HD solution, there are current peaks (Fig. 3) corresponding to adsorption at positive and for desorption at negative potential scan direction (noticeable at potential scan rates above 100 mV s^{-1}). The area under *i*,*E* peak is obtained as $q = iEt = iE / v$. Integrating the cyclic voltammetry peak (at v = 1 V s^{-1}) area between base electrolyte and HD solution gives almost equal charges for both adsorption (2.88 μC cm^{-2}) and desorption (–2.70 μC cm^{-2}) processes. The integrated charge is comparable with the one obtained from corresponding capacitance peak (3.14 μC cm^{-2}), measured using impedance

spectroscopy method [9], indicating, that the *i*,*E* peaks are caused only by the change of capacitance and not by the direct faradaic electron transfer reaction.

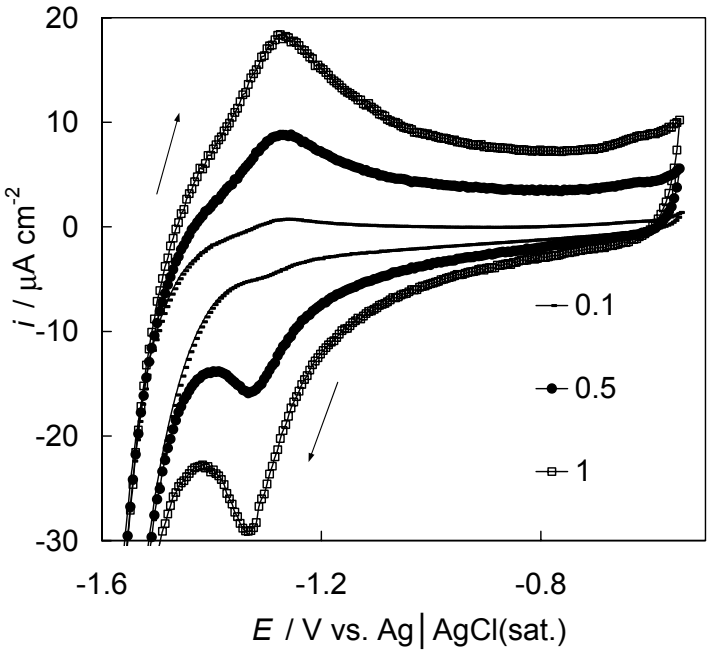

Figure 3. Cyclic voltammograms for Bi(111) interface in 0.5 M Na_2SO_4 base electrolyte solution with addition of 0.04 M 1,6-hexanediol at various potential scan rates (given in graph / V s^{-1}) .

The difference between adsorption and desorption peak potentials, noted as E_{ads} and E_{des}, varies from 28 to 72 mV for different organic compounds studied, and the adsorption-desorption peak found in the series capacitance versus potential curves (C_s,E) is situated in the middle of these peak potentials. The value of $E_{ads} - E_{des}$ is smaller if corresponding adsorption-desorption peaks in C_s,E-curves are sharper. The difference between CV adsorption and desorption peak potentials have been noticed also in other works, but the physical reasons of the peak formation were not discussed and the kinetic data was not analyzed [42–44].

The adsorption peaks shift to more positive potentials and the desorption peaks move to more negative potentials with increasing potential scan rate. E_{des},v curves for desorption peaks are nicely linear, but E_{ads},v adsorption curves, measured with Bi macroelectrodes, have small slopes and need higher scan rates for more precise data.

Microelectrode enables to measure CV-s at higher potential scan rates than a conventional mm-sized electrode. For Bi electrode with 4 mm diameter, the iR drop in 0.08 M pyridine + 0.1 M $LiClO_4$ aqueous solution at scan rate of 10 V s^{-1} is 2.4 mV at peak potential, but for 50 μm diameter Bi microelectrode,

this value is only 0.3 mV and adsorption processes at potential scan rates up to 100 V s^{-1} can be investigated without significant errors (iR < 3.5 mV).

The higher is the concentration of the organic substance, the smaller are the corresponding derivatives $\frac{\partial(E_{ads})}{\partial v}$ and $\left|\frac{\partial(E_{des})}{\partial v}\right|$ (data in Table 1). The slope value discussed was obtained from potential scan rate varying from 1 to 12 V s^{-1}, except for pyridine adsorption at microelectrode being from 1 to 100 V s^{-1}. The slope has a time dimension and therefore it may considered as a characteristic adsorption or desorption time. In case of pyridine (PY) and n-heptanol adsorption, the slope values indicate that the adsorption and desorption processes have similar rate constants for both Bi(111) and Bi(001) interfaces [10].

Table 1. Some parameters characterizing cyclic voltammetry capacitive adsorption and desorption peaks in different systems.

System	$\frac{E_{ads}+E_{des}}{2}$ / V	$E_{ads}-E_{des}$ / mV	$\frac{\partial(E_{ads})}{\partial v}$ / s	$\left\|\frac{\partial(E_{des})}{\partial v}\right\|$ / s
Bi(111)|0.1 M $LiClO_4$ + 0.08 M pyridine	–1.55	28	0.00038	0.00029
Bi(001)|0.1 M $LiClO_4$ + 0.08 M pyridine	–1.44	25	0.00036	0.00033
Bi(111)|0.1 M $LiClO_4$ + 5 mM n-heptanol	–1.27	44	0.0003	0.0032
Bi(001)|0.1 M $LiClO_4$ + 5 mM n-heptanol	–1.13	40	0.0006	0.0021
Bi(001)|0.1 M $LiClO_4$ + 2.5 mM n-heptanol	–1.06	46	0.0012	0.0027
Bi(001)|0.1 M $LiClO_4$ + 1.3 mM n-heptanol	–1.00	57	0.002	0.0053
Bi(111)|0.5 M Na_2SO_4 + 0.040 M HD	–1.30	72	0	0.0011
Bi(111)|0.5 M Na_2SO_4 + 0.32 M HD	–1.43	72	0	0.0010

According to data in Table 1, adsorption of measured compounds tends to be faster than the desorption process. Adsorption time constant for n-heptanol depends nearly linearly on its concentration in solution, and is smaller for higher organic compound solutions. Desorption is quick for small rigid molecules (pyridine), but is slow for n-heptanol molecule that has stronger interactions between other n-heptanol molecules.

4.2. Impedance spectroscopy

Impedance spectroscopy is an informative technique for investigating different electrochemical systems and processes. Cyclic voltammetry usually drives electrodes to a condition far from equilibrium. In contrast, impedance methods are based on perturbation of the electrochemical cell with an alternating signal of small magnitude (~5 mV), allowing measurements at equilibrium or steady state [45,46]. In this work, impedance spectroscopy has been used for the determination of electrochemical reaction mechanisms or quality of the electrodes.

Sinusoidal perturbation is applied to the electrode

$$E(\mathrm{t}) = E_{\mathrm{A}} \sin \omega t \tag{4.2.1}$$

where E(t) is the potential at time t, E_{A} is the potential amplitude, $\omega = 2\pi f$ is the radial frequency, and f is frequency in Hz units. The current response will be a sinusoid at the same frequency but shifted in phase

$$i(\mathrm{t}) = i_{\mathrm{A}} \sin(\omega t + \Phi) \tag{4.2.2}$$

where i(t) is the current at time t, i_{A} is the current amplitude and Φ is phase shift by which the potential lags the current [45,46]. The impedance is defined analogously to the Ohm's law as the ratio of voltage and current

$$Z = \frac{E(t)}{i(t)} \tag{4.2.3}$$

Impedance has magnitude ($Z_{\mathrm{A}} = E_{\mathrm{A}}/I_{\mathrm{A}}$) and phase angle and is thus a vector quantity

$$Z = Z_{\mathrm{A}}(\cos \Phi + \mathrm{j}\sin \Phi) = Z' + \mathrm{j}Z'' \tag{4.2.4}$$

where $\mathrm{j} = \sqrt{-1}$, Z' is real part of impedance, and Z'' the imaginary part of the impedance [45,46].

If sinusoidal voltage is applied across a pure capacitor, the impedance can be calculated according to the relationship

$$Z = \frac{1}{\mathrm{j}\omega C} = -\frac{\mathrm{j}}{\omega C} \tag{4.2.5}$$

where C is the capacitance and the phase angle $\Phi = -90^0$, that is, the impedance depends on the frequency and is entirely imaginary [45,46].

There are two accurate ways to obtain an indication of quality of a modelling function, the square of the standard deviation between the original data and the calculated spectrum (each data points weight is normalized by its magnitude) (χ^2) and the weighted sum of the squares (Δ^2) giving a main general indication about the preciseness of a fit and observing the parameter values and their relative error estimates (in %) [47]. In this work, experimental impedance data were mainly analyzed using the equivalent circuits illustrated in Fig. 4.

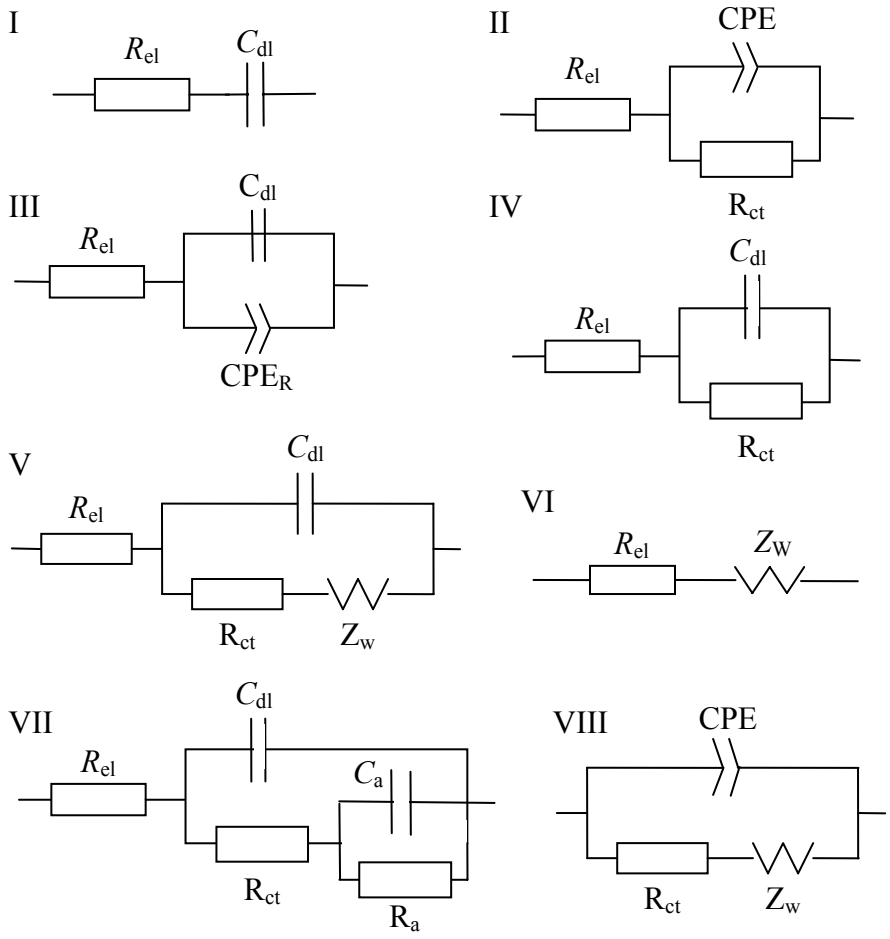

Figure 4. Equivalent circuits used for fitting the complex impedance plane plots. R_{el} is electrolyte resistance, C_{dl} is double layer capacitance, CPE is constant phase element, CPE_R is also constant phase element but with exponent values close to 0, R_{ct} is charge transfer resistance, Z_W is short circuit Warburg impedance, C_a is adsorption faradaic capacitance, and R_a is adsorption resistance.

4.2.1. Impedance of an ideally polarizable electrode

The concept of an "ideally polarizable" electrode was described in the work by Grahame [48] as the one where changes of potential due to flow of charge to or from the electrode cause only changes of charge density on the metal and conjugately of ion density on the solution side of the electrode interface, leading to charging of the resulting double layer. In this case, the equivalent electrical circuit (EC) consists only of the solution resistance, R_s, in series with the double-layer capacitance, C_{dl} (model I in Fig. 4) [49–51].

The Hg electrode in aqueous solutions of NaF or Na_2SO_4 comes close to the above requirements for an ideally polarizable interface. Hg is almost ideally polarizable over the potential range from +0.03 V to –1.1 V [52].

Gold is another metal that exhibits almost ideal polarizability over a certain range of potentials: current density values less than |1| μF cm^{-2} at sweep rate of 10 mV s^{-1} (from –0.25 to 0.75 V vs. SCE) and the value of α = 0.997 (the meaning of α is discussed in next chapter) has been obtained for Au(111) electrode in 0.1 M $HClO_4$ solution [53].

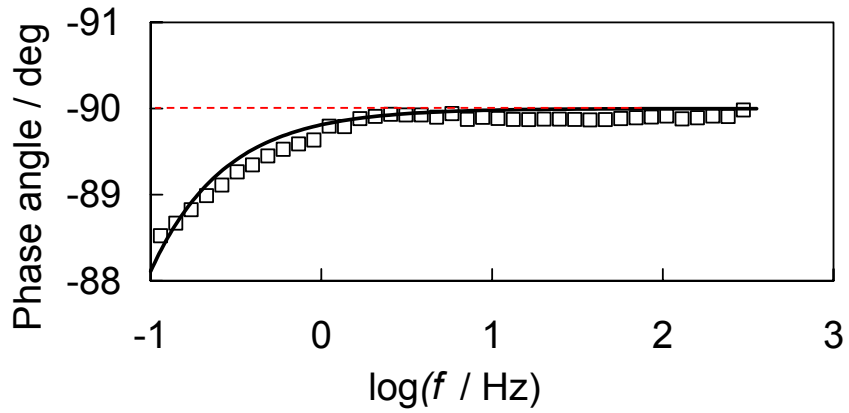

Figure 5. Phase angle vs. logarithm of frequency (where solution resistance is subtracted) for Bi(001) in 0.1 M $LiClO_4$ aqueous solution at –0.6 V. Solid and broken lines have been obtained by fitting of measured spectra with equivalent circuits II and I, respectively.

Cyclic voltammetry measurements in 0.1 M $LiClO_4$ aqueous solution indicate very low current density values (i < –100 nA cm^{-2}) from –1.2 to –0.40 V for Bi(001) and from –1.15 to –0.4 V for Bi(111) electrode [2]. The impedance for electropolished Bi(001) at –0.6 V (Fig. 5) can be fitted using EC I in Fig. 4 (R_{el} = 20 Ω cm^2, C_{dl} = 22.0 μF cm^{-2}, χ^2 = 0.008 and Δ^2 = 0.61) and therefore, the conditions of ideal polarizability are nearly satisfied.

Ideally polarizable electrode has an importance in electrochemical studies because other reactions can be studied at this electrode in its ideally polarizable potential region.

4.2.2. Capacitance dispersion of ac frequency

Frequency dispersion of capacitance is often observed in the case of solid electrodes, which have been attributed to the atomic scale roughness, crystallographic heterogeneity, and chemical inhomogeneities on the surface [54–62]. Porous systems usually show larger frequency dispersion than smooth ones [55,56]. Surprisingly, it was found that porous pure metal or nanoporous carbon electrodes may have only minor frequency dispersion effect in the absence of specific adsorption [56–59]. The frequency dispersion occurs for Au and Pt electrodes in halide solutions within the potential region, where adsorption and superficial species rearrangement takes place [63–65].

The frequency dispersion of capacitance can be represented with a constant phase element CPE with impedance

$$Z_{CPE} = \frac{1}{A(\mathrm{j}\omega)^{\alpha}} \qquad (4.2.2.1)$$

where A is a CPE coefficient and α is a CPE fractional exponent. In Nyquist plot, CPE is a straight line with angle $\Phi = -(\alpha * 90^0)$. If $\alpha = 1$, then A is equal to the electrical double layer capacitance, if $\alpha = 0.5$, then $Z_{CPE} = Z_W$ (Warburg-like diffusion impedance) and if $\alpha = 0$, then Z_{CPE} is equal to the resistance R [46,51]. The value of α can be obtained from fitting results as well as from the slope of plot of -log(-Z'') vs. log$f$.

Equivalent circuit II in Fig. 4 that is often used to represent the impedance behaviour of solid electrodes was used for fitting the calculated impedance spectra with experimental spectra [51]. Data from Table 2 indicate that the frequency dispersion is negligible for Bi single crystal electrodes as well as for porous Bi but exists for smaller and thin-film Bi electrodes. The value of α equal or higher than 0.996 is the best result ever measured for bismuth single crystal electrodes [66]. It has to be noted that the Bi(001) and Bi(111) data correspond to the best experiments but α values as low as 0.92 corres-

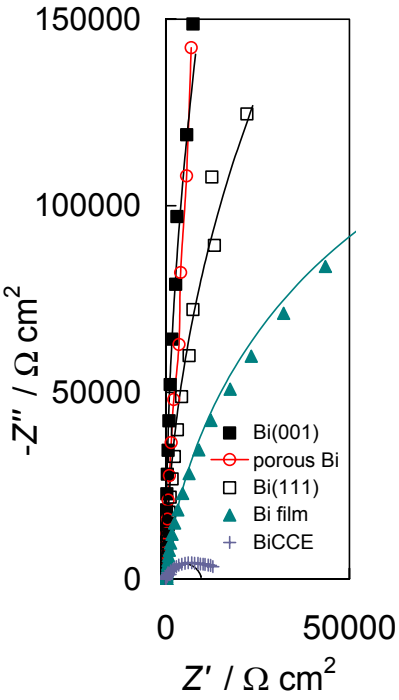

Figure 6. –Z'',Z' plot for different Bi electrodes in 0.1 M $LiClO_4$ aqueous solution at -0.6 V (lower ac frequency is 0.05 Hz). Solid lines have been obtained by fitting of calculated impedance spectra with measured ones using EC II.

pond to the electropolished electrode with an isolation leakage. The lower value of α is always accompanied with smaller value of R_{ct} (data in Table 2). Therefore, the Bi electrode capacitance dispersion of frequency depends on the surface purity (i.e. on the faradaic or specific adsorption processes) but not on the surface roughness.

Table 2. Fitting results for Bi interfaces at $E = -0.6$ V in 0.1 M $LiClO_4$ aqueous solution according to scheme II in Fig. 4.

Bi electrode	χ^2	Δ^2	R_{el} / Ω cm^2	A_R / μF s^{1-a} cm^2	α	R_{ct} / Ω cm^2
(001)	0.003	0.22	20	21.7	1.00	$1.9 \cdot 10^6$
(111)	0.002	0.16	19	22.7	0.996	$6.3 \cdot 10^5$
Porous (R = 220)	0.0025	0.11	67	21.9	0.999	$9.9 \cdot 10^5$
100 nm thick film	0.0015	0.10	183	10.9	0.954	$2.2 \cdot 10^5$
50 μm BiCCE	0.015	1.1	0.89	24.2	0.924	$7.8 \cdot 10^4$

Where R is roughness factor.

The fractional exponent value as high as 0.999 for bismuth sponge is surprising as for porous electrodes, usually much larger frequency dependence of capacitance have been measured [55]. Porous Au with roughness factor 770 has been characterized with the value of CPE exponent $\alpha \sim 0.977$ [57], but the differences between electrochemical properties of different gold single crystal interfaces (zero charge potential difference is up to 450 mV [54]) are larger than that of Bi single crystal electrodes. Also, low melting point of Bi excludes the high atomic level roughness.

The CPE behaviour is in conflict with the condition of ideal polarizability [67–68]. This is because they cannot be assigned a unique charge, a thermodynamic variable inherent to the ideal polarisability, represented mathematically by the Lippmann equation [50].

Small frequency dependence has also been measured at –1 V for Bi(001)| 0.5 mM $HClO_4$ aqueous solution: the semicircles can be modelled with $\alpha > 0.99$ [11].

4.2.3. Charge transfer resistance dispersion of ac frequency

For HER reaction, the C_{dl} is quite independent of ac frequency if the electrode surface consists of pure Bi. Even for porous Bi, α value is above 0.99 at –1.6 V in 0.1 M $LiClO_4$ aqueous solution. There is a semicircle in the $-Z'',Z'$-plot at –1.6 V indicating to the reaction with a single charge transfer limiting step. However, fitting with a simple parallel combination capacitor and resistor (EC IV in Fig. 4) does not describe the impedance spectra sufficiently. It is charac-

teristic that the phase angle at low frequencies has constant value of 3–4 degrees instead of 0, predicted by EC IV. Data in Table 3 indicate that by replacing R_{ct} with CPE_R, having α value close to zero, good fittings of data can be obtained (1–2 orders of magnitude lower χ^2 values were obtained with CPE_R instead of resistor). Therefore, the charge transfer resistance of Bi electrodes is dependent on ac frequency in solutions containing high concentrations of supporting electrolyte.

Table 3. Fitting results for Bi interfaces according to scheme III in Fig. 4.

System	χ^2	Δ^2	R_{el} / Ω cm^2	C_{dl} / μF cm^{-2}	A_R / F s$^{1-\alpha}$ cm^2	α
Bi(001) at –0.95 V| 1 mM $HClO_4$	0.00014	0.011	387	14.6	1.63E–04	0.006
Bi(001) at –1.0 V|1 mM $HClO_4$ + 0.1 M $LiClO_4$	0.00099	0.068	17.9	14.2	2.47E–04	0.039
Bi(001) at –1.6 V| 0.1 M $LiClO_4$	0.00048	0.039	19.4	16.4	1.68E–03	0.030
Bi(111) at –1.6 V| 0.1 M $LiClO_4$	0.00048	0.035	17.8	16.8	5.08E–03	0.033
Porous Bi at –1.6 V| 0.1 M $LiClO_4$	0.00031	0.017	76.0	13.1	1.86E–05	0.052

4.2.4. Faradaic reaction and diffusion limitation conditions

The peak in C_s,E-plots corresponds to the conditions where there is diffusion limitation at one side of the peak potential and slow charge transfer or adsorption are rate determining steps at the other side. This condition is satisfied in case of low frequency peaks due to faradaic reaction [11] as well as in case of adsorption-desorption peaks (caused by adsorption of organic compound or specific adsorption of ions) due to the change in electrical double layer capacitance [12,69].

The impedance response due to slow mass-transfer step can be described with mass-transfer impedance Z_W also called Warburg impedance. Mass-transfer coefficient can be expressed as [41,46,51]

$$\sigma = \frac{RT}{n^2F^2S\sqrt{2}}\left(\frac{1}{c_{ox}^0\sqrt{D_{ox}}} + \frac{1}{c_{red}^0\sqrt{D_{red}}}\right), \qquad (4.2.4.1)$$

where S is electrode area. Warburg impedance is obtained as

$$Z_W = \frac{\delta}{\sqrt{w}} - j\frac{\delta}{\sqrt{w}}\ , \qquad (4.2.4.2)$$

where first member describes the diffusion process real part and the second imaginary part of complex diffusion resistance [41,46]. Corresponding faradaic impedance for mixed kinetics is expressed as a serial combination of charge-transfer resistance and Warburg impedance. The resulting equivalent circuit is also known as Randles circuit, shown as EC V in Fig. 4 [41,46].

For more complex cases, the generalized finite-length Warburg element for a short circuit terminus model expresses as

$$Z_W = \frac{R_D \tanh\left[(j\omega T)^{\alpha_W}\right]}{(j\omega T)^{\alpha_W}}\ , \qquad (4.2.4.3)$$

where R_D is the limiting diffusion resistance, $T = L^2/D$ is diffusion time constant, L is the effective diffusion layer thickness, D is the effective diffusion coefficient of a particle and α_w is fractional exponent for Warburg-like diffusion impedance [41,46,51].

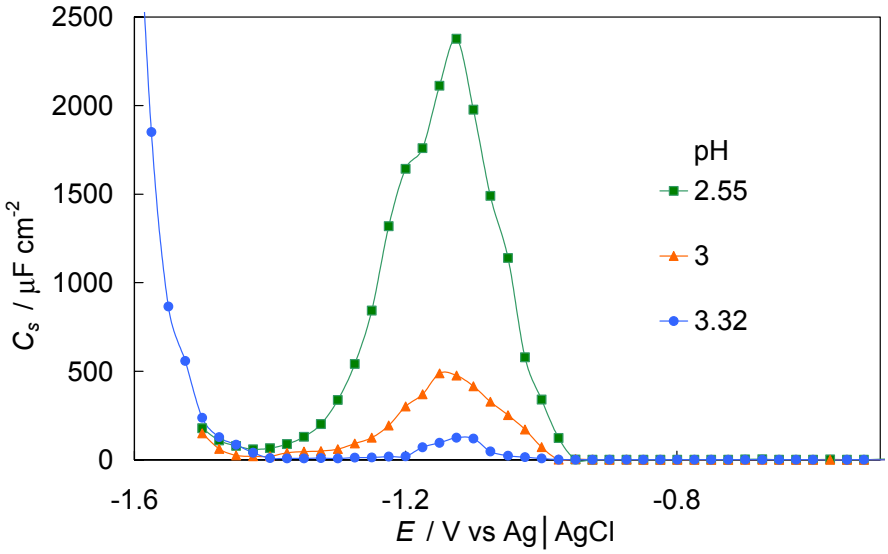

Figure 7. C_s,E dependence (1 Hz) for Bi(001) electrode in 0.1 M $LiClO_4$ + $HClO_4$ solution at different pH values (given in graph).

For HER reaction, there is a peak at about –1.15 V in C_s,E-plot at low ac frequencies (Fig. 7). It was found that at peak potential, there is equilibrium between mass-transfer and charge transfer steps and the impedance behaviour

can be fitted with Randles circuit (semicircle with 45^0 line at lower frequencies in $-Z''$,Z'-plot; EC V in Fig. 4) [46]. At more negative potentials, the reaction is limited by mass-transfer step (45 degree angle line; EC VI), at slightly less negative potentials the reaction is limited by charge transfer step (semicircle; EC IV), and near zero charge potential there is ideally polarizable region (IPR) (nearly 90 degree angle). The corresponding $-Z''$,Z'-plots are shown in Fig. 8 and fitting results in Table 4.

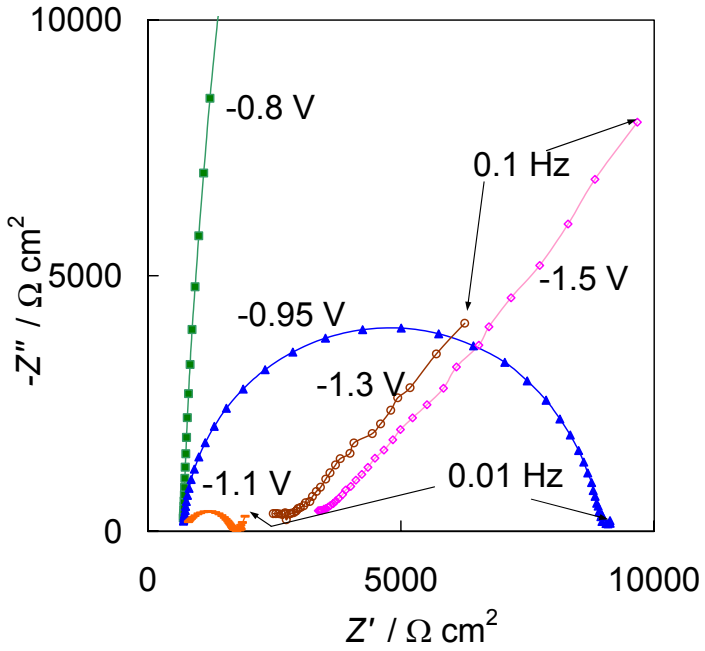

Figure 8. $-Z''$,Z' dependence for Bi(001)|0.5 mM $HClO_4$ aqueous solution (pH = 3.31) at different electrode potentials (given in figure).

Table 4. Fitting results for Bi(001)|0.5 mM $HClO_4$ (pH = 3.31) interface according to ECs in Fig. 4.

E / V Ag | AgCl	χ^2	Δ^2	R_{el} / Ω cm^2	C_{dl} / μF cm^{-2}	R_{ct} / Ω cm^2	R_D / Ω cm^2	T / s	α_W	EC
–0.55	0.03	2	730 (6%)	7.2 (1.2%)	447811 (5%)				IV
–0.95	0.0002	0.013	727 (0.5%)	16.9 (0.3%)	8056 (0.3%)				IV
–1.1	0.005	0.4	802 (1%)	14.4 (3%)	865 (1%)	376 (85%)	27 (190%)	0.5	V
–1.3	0.001	0.06	2476 (0.7%)			16446 (56%)	19 (113%)	0.5	VI

Dependence of logR_{ct} on *pH* is a linear with unity slope, indicating to a first-order reaction. Thus, at C_s,*E* peak potential $R_{ct} = [H^+]$ for Bi(001)|0.1 M $LiClO_4$ + $HClO_4$ and $R_{ct} = [H^+] - 0.4$ for Bi(001)|$HClO_4$. These values also apply for Bi(011–) and Cd(0001) electodes [11].

According to equation 4.2.4.2, σ can be calculated from slope of *Z*' vs. $w^{-1/2}$, and the slope is shown in Fig. 9. For further calculation of diffusion coefficients according to equation 4.2.4.1, only concentration of H^+ was taken into account, as c^0_{red} is small. Diffusion coefficient *D* for H^+ ion is $9.3*10^{-5}$ cm^2 s^{-1} and that for perchloric acid is $2–6*10^{-5}$ cm^2 s^{-1}, increasing with acid concentration [70]. Diffusion coefficient values, calculated for $HClO_4$ reduction on Bi electrode, are close to the actual value of D_{H+}, although systematically smaller. The addition of $LiClO_4$ solution reduces the D_{H+} values even more, caused by the electrical double layer influence. The activity of protonated water near the cathode surface reduces more than two orders of magnitude with the addition of Li^+ ions.

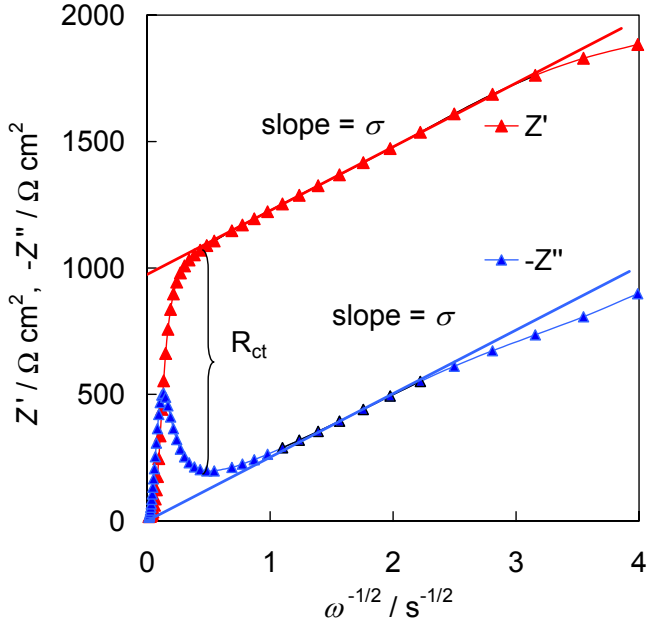

Figure 9. Calculation of R_{ct} and σ from impedance data for Bi(001)|0.1 M $LiClO_4$ + 1 mM $HClO_4$ system at –1.15 V.

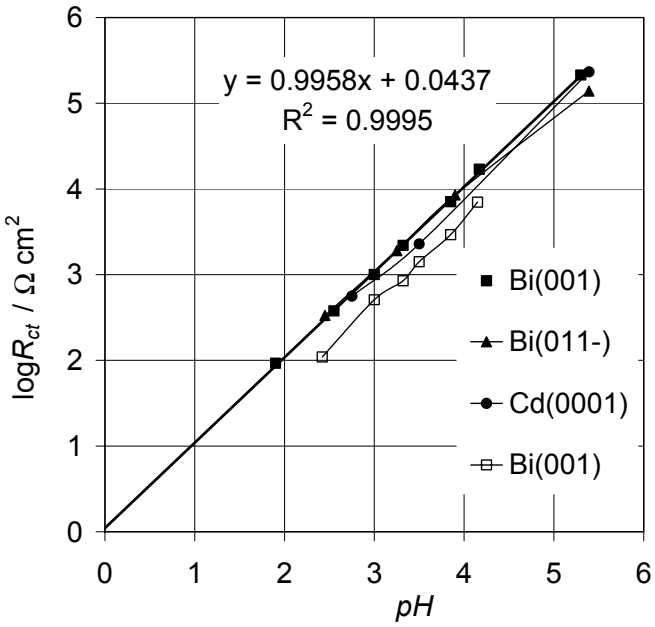

Figure 10. Charge transfer resistance (R_{ct}) vs. solution pH at *C,E* peak potential (*E* = –1.1...–1.15 / V Ag | AgCl) in 0.1 M $LiClO_4$ + $HClO_4$ (filled marks) or $HClO_4$ aqueous solution (empty rectangles).

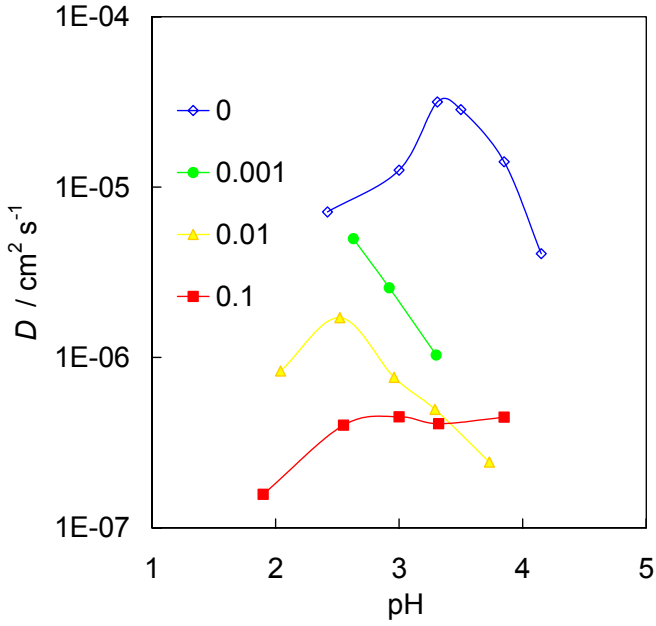

Figure 11. Diffusion coefficient (*D*) vs. solution pH for Bi(001) electrode at –1.15 V in $HClO_4$ aqueous solution (pH values are given in graph) with different $LiClO_4$ additions (given in figure / M).

From logR_{ct},E-plots, α_t and i_0 can be determined with higher precision than that from CV data [12]. According to formula 4.1.3, α_t = 0.55 ± 0.01 and R_0 = 9 (± 3)*10^{10} Ω cm^2 giving i_0 = 3 (± 1)*10^{-13} A cm^{-2}. Analysis of traditional Taffel plot gave i_0 = 2*10^{-12} A cm^{-2} and α_t = 0.54, although in Ref. [71] several order of magnitude higher values have been obtained. Electron transfer rate constant k_s, calculated according to equation 4.1.4, is 1.6 * 10^{-15} cm s^{-1}.

4.2.5. Faradaic reaction involving one adsorbed species

Inductivity element in equivalent circuit causes impedance as

$$Z = j\omega L \tag{4.2.5.1}$$

and in this case phase angle $\Phi = 90^0$ [46].

Inductive loops are often associated to the phase change of a solid, i.e. to corrosion or dissolving interfaces [72,73] or electrodeposition of metals [74]. Monte-Carlo simulations of metal dissolution show that surface adsorbate relaxation can effectively initiate inductive loops in an electrochemical impedance spectrum [75,76]. Equivalent circuit VII in Fig. 4 corresponds to the impedance behaviour of a faradaic reaction involving one adsorbed species [51]. Impedance curves in Fig. 7 can be fitted with EC VII, if R_a and C_a have both negative values, or with EC containing an inductance element [51]. In both cases, the forward and reversible rate constants for the electrochemical desorption step (second reaction) have to be larger than that for the adsorption step (first reaction) [51].

Impedance spectra for Bi electrode at E < –2 V has an inductive loop at the lower frequency region of spectrum. All the impedance spectra in Fig. 12 have inductive loops, and the spectrum measured at –2.2 V even has a nearly round shape.

The parameters for the Bi|0.002 M $LiClO_4$ aqueous solution interface at E = –2.1 V, calculated using EC VII, have the following values: R_{el} = 11 Ω cm^2, C_{dl} = 36.0 μF cm^{-2}, R_{ct} = 31 Ω cm^2, C_a = –0.014 μF cm^{-2} and R_a = –13 Ω cm^2, χ^2 = 0.007, and Δ^2 = 0.37. It has to be noted that replacing C_a with CPE would increase the fitting quality noticeably (χ^2 and Δ^2 decrease 4 times), but C_{dl} was found to be independent of ac frequency. The inductive loop in impedance spectrum can be explained as relaxation of short-lived bismuth hydrides on the electrode surface (reactions are discussed more thoroughly in section 6.1) [2,77–81].

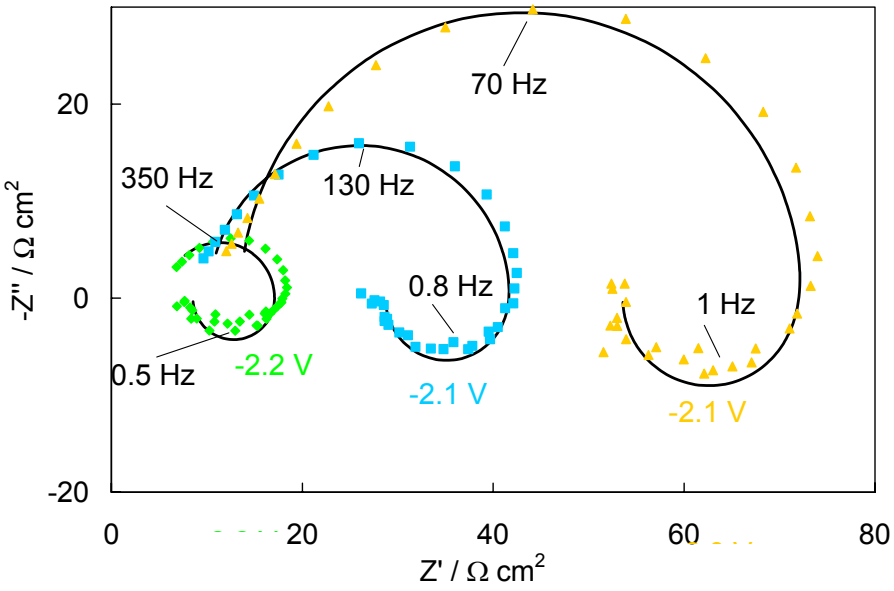

Figure 12. $-Z'',Z'$ plot for BiCCE in 0.002 M $LiClO_4$ aqueous solution at different extremely negative potentials, given in figure. Solid lines have been obtained by fitting of measured spectra with equivalent circuit VIII.

4.2.6. Impedance of a blocking adsorbed layer

The Bi(001) electrode surface, modified with 1-octadecanethiol (ODT), shows quite different impedance response compared to Bi(001)|0.1 M $LiClO_4$ interface (Fig. 13). The thiol modified interface behaves as having very low electrolyte resistance although the charge transfer resistance is much smaller than that for pure Bi surface.

To explain this behaviour, the thiolate coated electrode surface may be considered as an electrically isolated surface that has micrometer-sized and even smaller defects (pin-holes) nearly homogeneously distributed over the whole surface. Therefore, Bi|bismuth thiolate system seems to be like a microelectrode array characterised by spherical diffusion properties but charge transfer through these surface defects on the thiolate coated Bi surface is possible. Detailed analysis of the $-Z'',Z'$ plots show that the short circuit Warburg impedance describes correctly the impedance response of moving charged particle through the holes in $Bi(ODT)_3$ layer [82–83]. Thus, an EC VIII can be used for fitting of Bi(001)|$Bi(ODT)_3$|0.1 M $LiClO_4$ impedance data [47].

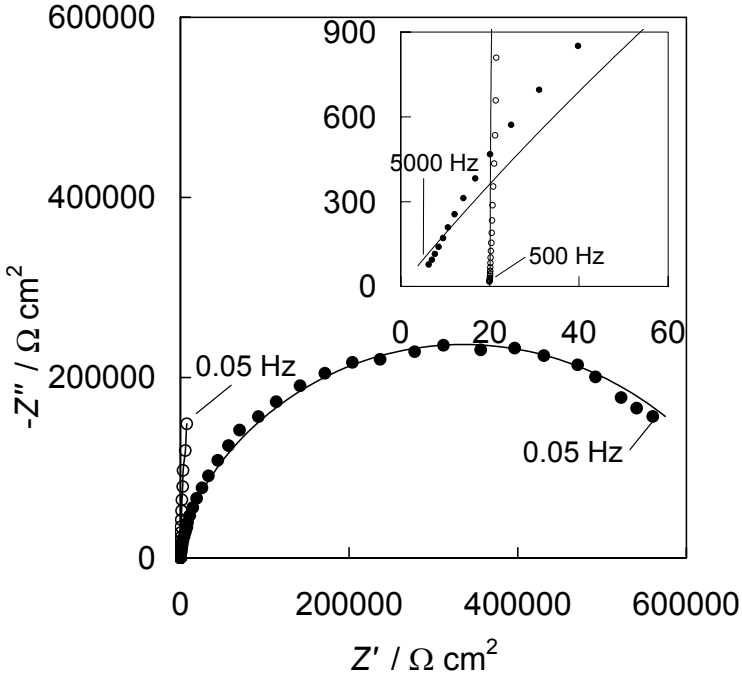

Figure 13. –Z'',Z' dependence for clean Bi(001) electrode (open marks) and ODT modified Bi(001) electrode (filled marks) in 0.1 M $LiClO_4$ aqueous solution at E = –0.6 V. Higher frequency part is given as inset. The solid lines correspond to the fittings with equivalent circuits I for Bi(001) and VIII for Bi(001)|thiol.

4.3. Infrared spectra of thin films and in situ measurements of electrochemical processes

Applying infrared spectroscopy, chemical composition and orientation of molecules can be analyzed. Over the last two decades, in situ infrared spectroelectrochemistry has become an increasingly powerful analytical tool in electrochemistry: the detection of organic monolayers is now commonplace [84–88], and there is other exciting work about of the double layer characterization [89–93]. Firstly, all common solvents, and especially water, absorb infrared light strongly; secondly, the amount of absorbing species of interest at or near an electrode is extremely small, rendering sensitivity a significant problem at a time when conventional infrared sources were weak, and detectors insensitive.

4.3.1. Grazing angle ATR spectra of thiol modified Au and Bi surfaces

FTIR allows for a detailed characterization of chain-conformational properties, packing arrangement, and chemical composition. There are plenty of published grazing angle infrared reflection spectra in the literature about self-assembled monolayers on gold [34–38]. Thus, we also obtained similar spectra for thiol modified bismuth [8]. However, only C-H stretching modes can be seen with aforementioned method, giving limited amount of information. Therefore, we measured more sensitive grazing angle ATR spectra and can now also discuss the spectra at lower wavenumber region. Due to the lack of such information in the literature, we also measured thiol self-assembled monolayers on gold (150 nm thick Au(111) on mica). The infrared setup consisted of 2 mirrors and a 25 mm diameter Ge hemisphere where the thiol modified sample was pressed against, p-polarized infrared beam intersected the hemisphere at 60 degrees angle of incidence.

Figs. 14 and 15 show absorbance spectra of octadecanethiol (ODT), thiol modified Bi and Au, and $Bi(ODT)_3$ fibers (synthesis method discussed later). Thiol modified surfaces have been prepared by holding Bi or Au electrodes in 1 mM thiol solution in ethanol for 24 hours. The absorbance for thiol modified bismuth surface is about 5 times larger than for ODT monolayer on Au(111), indicating that a thicker layer has been formed on Bi. However, the intensity of ATR spectra depends how good contact have been obtained with the ATR crystal, being more difficult to achieve for 4 mm Bi cylinder. Also, enhancement effects are stronger for thinner layers.

Fig. 14 shows absorbance spectra of the C-H stretching modes of the polymethylene $[–(CH_2)_n–]$ sequence and end-methyl $[–CH_3]$ [94,95]. A summary of these assignments is given in Table 5.

The weak peak observed at 2872–2877 cm^{-1} and a shoulder at 2935 cm^{-1} are assigned to the CH_3 group's symmetric CH stretching modes (Fig. 14). This doublet of the symmetric stretch of the CH_3 group is understood to arise from the intramolecular Fermi resonance interaction with the overtone of the CH_3 group asymmetric deformation [94]. These peaks are the strongest in Au + ODT spectra, indicating to a more vertical position of methyl groups in the thiol monolayer. Weak peaks for thiol modified Bi indicate the absence of vertically oriented organic compound layer.

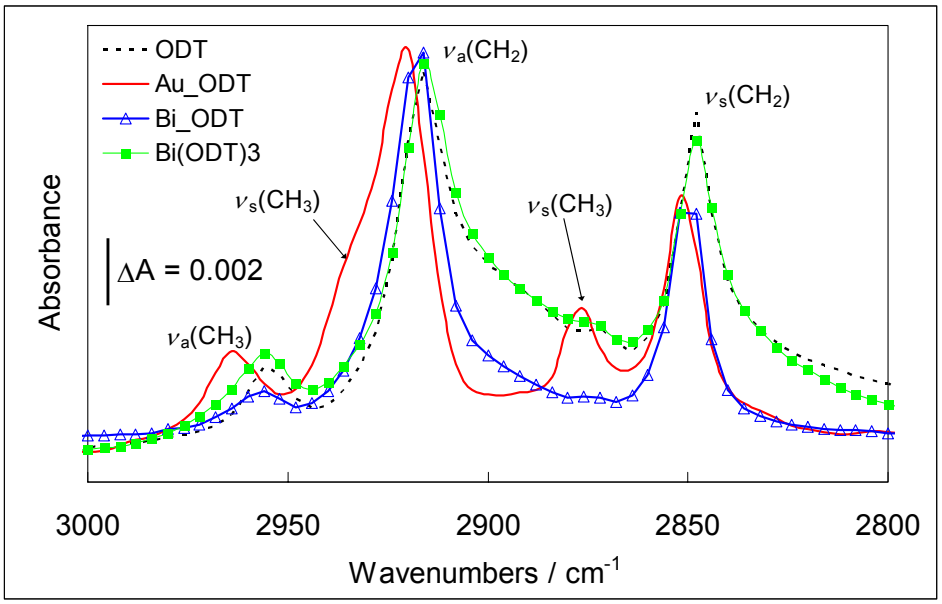

Figure 14. Infrared spectra of ODT, thiol modified surfaces, and $Bi(ODT)_3$ in the high-frequency region showing C-H stretching modes (25 mm diameter Ge hemisphere; 60 degrees angle of incidence: p-polarization). Absorbance for Au is original, and scaled for other measurements.

The two strongest bands in Figure 14 with peak maxima at 2847–2851 and 2915–2920 cm^{-1} are assigned to CH_2 C-H symmetric and antisymmetric stretching modes, respectively. The exact location of these peaks is known to be a strong indicator of chain conformation. For crystalline *n*-alkanes, these modes occur in the ranges of 2846–2849 and 2916–2918 cm^{-1}, respectively [94]. These ranges are known to shift with increase in gauche population in the polymethylene ensemble and assume the ranges of 2854–2856 and 2924–2928 cm^{-1} for high-temperature disordered or liquid phases of *n*-alkanes [94]. The observed positions in a narrow range of 2849–2850 and 2915–2917 cm^{-1} for ODT, Bi + ODT, and $Bi(ODT)_3$ indicate the well ordered crystalline structure. Au|ODT system has CH_2 absorption peaks at ~2 cm^{-1} higher wavenumbers and CH_3 bands at 4–9 cm^{-1} higher wavenumbers. Therefore, ODT monolayer on Au(111) has less crystalline structure, especially CH_3 groups have more loose packing, but Bi electrode is coated with thiolate crystals rather than oriented layers.

The absence of ν(SH) peak at 2559 cm^{-1} for thiol modified Au and Bi indicates that the adsorbed compound is not in thiol form. Absorption bands for metal-sulfur vibrations are fortunately at too low wavenumbers to be detectable with an MCT detector.

Absorbance spectra in the 1550–650 cm^{-1} region is shown in Fig. 15.

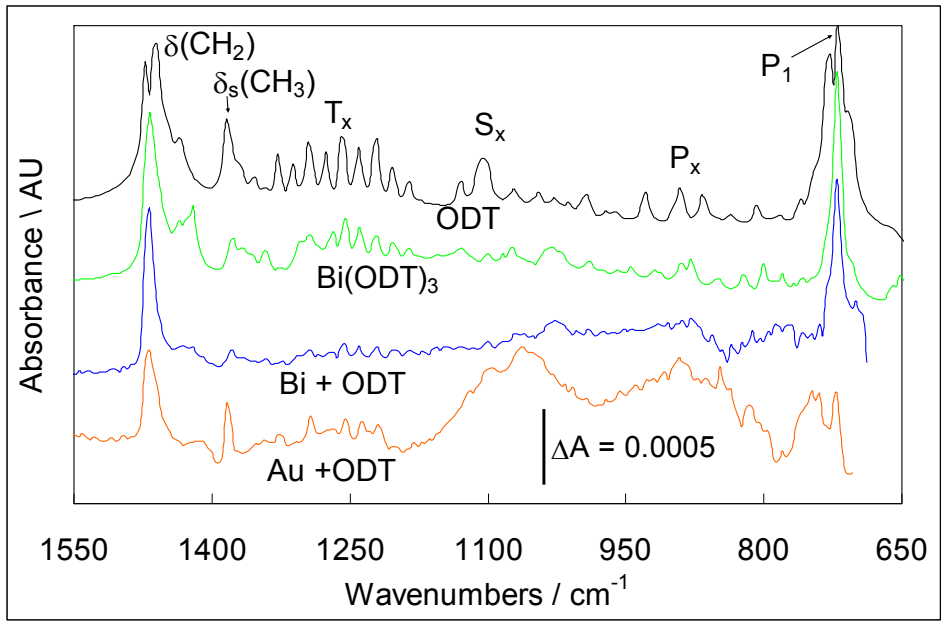

Figure 15. Infrared spectra in the low-frequency region.

Two strong peaks in this region are CH_2 deformation (scissoring) peak at 1470 cm^{-1} and the head-band of series of rocking modes of the chain methylenes (P_1) at 720 cm^{-1} [94]. Exact characteristics of these peaks provide a sensitive measure of the packing arrangement of the alkyl chains. In orthorhombic arrangements of the polymethylene chains, the scissoring peak and rocking peaks are split into two components by interchain interactions between the contiguous CH_2 groups of the two chains that constitute the crystal sub-cell [94]. This splitting, referred to as factor-group splitting, is specific to orthorhombic sub-cells [94]. It is not observed in the alternative single-chain subcells of monoclinic or triclinic packing, where only one peak is observed. The observed singlet for all Au and Bi thiols at 1470 cm^{-1} in this regard implies that the unit cell is composed of only one chain. Taken alone, the observation above excludes the orthorhombic arrangement, but does not distinguish between the monoclinic or triclinic types of packing that may occur in polymethylene chains.

Second derivative spectra reveal a weak peak at 1460–1455 cm^{-1} for all systems measured. The peak at 1455 cm^{-1} is assigned to out-of-plane CH_3 asymmetric deformation or bending mode while the contribution at 1460 cm^{-1} is assigned to in-plane CH_3 asymmetric deformation [94].

The peak appearing at 1383–1378 cm^{-1} is assigned to the CH_3 symmetric deformation, sometimes called umbrella mode [94]. Intensive peaks were measured for ODT and Au + ODT systems, but weak peaks for Bi + ODT and $Bi(ODT)_2$ systems.

The band at 1416 cm^{-1} is associated with scissoring of a methylene group adjacent to the metal-sulphur bonds [94]. There is medium intensity band at 1420 cm^{-1} in $Bi(ODT)_3$ spectra and weaker band for the Bi + ODT system. Au + ODT system has weak and wide peak at 1410 cm^{-1} and ODT does not have this peak. This is the only peak that can be used for distinguishing bismuth thiolate layer because Bi-S vibration bands occur at too low wavenumbers.

Next the appearance of the series of uniformly spaced peaks of moderate intensities with alternating weak shoulders between 1175 and 1300 cm^{-1} is assigned to the more intense wagging (W_x) and weaker twisting (T_x) modes. The occurrence of the wag-twist progression series, establishes unambiguously that the trans polymethylene sequence constitutes the dominant population of chain conformers in the crystals. In contrast, if the chains were disordered, as in high-temperature or liquid-phase *n*-alkanes, these features would diminish in intensity, broaden, and appear as long-wavelength bumps in the spectra [94]. Additionally, the number, the intensity, and the inter-band separation all depend on the average number of trans conformers in the chains according the following equation: [94]

$$\Delta\nu = 326 / (m + 1) \qquad (4.3.1.1)$$

The calculated number of trans methylene units in molecule is 17.1, 17.4, 17.6, 16.9 for ODT, Au + ODT, Bi + ODT, and $Bi(ODT)_3$, respectively. These numbers show remarkably well, that nearly the entire length of the chain substituent is in all-trans conformation for all samples.

Another relevant feature of interest in this region of the spectra of polymethylene assemblies, in general, is the presence of peaks exclusive to localized vibrations of nonplanar or gauche conformations. For example, the peak at 1341 cm^{-1} for thiol modified bismuth surface and $Bi(ODT)_3$ compound indicates an end-gauche effect [94].

Table 5. Interpretation of some infrared peaks for ODT, thiol modified surfaces, and $Bi(ODT)_3$ [94,95].

Symbol	Vibration	ODT	Au + ODT	Bi + ODT	$Bi(ODT)_3$
$\nu_a(CH_3)$	asym str (op)	2956 (w)	2964 (m)	2956 (w)	2955 (m)
$\nu_s(CH_3)$	sym str (FR1)	–	2936 (w)	–	2935 (vw)
$\nu_a(CH_2)$	asym str	2917 (s)	2920 (s)	2918 (s)	2916 (s)
$\nu_s(CH_3)$	sym str (FR2)	2873 (w)	2877 (m)	2873 (w)	2873 (w)
$\nu_s(CH_2)$	sym str (ip)	2849 (s)	2851 (s)	2850 (s)	2849 (s)
$\nu(SH)$	str	2559 (w)	–	–	–
$\delta(CH_2)$	def, scissor	1473 (s) 1462 (s)	1470 (s)	1469 (s)	1467 (s)
$\delta_a(CH_3)$	asym def	1454 (m)	1457 (w)	1457 (m)	1455 (m)
$\delta(S–CH_2)$	def, scissor	–	–	1422 (w)	1420 (m)
$\delta_s(CH_3)$	sym def, umbrella	1383 (s)	1384 (s)	1379 (w)	1378 (m)
end-gauche	CH_2 wag	–	1344 (w)	1341 (w)	1341 (m)
W_x	CH_2 wag	1328 (m)	1327 (m)	1325 (m)	1325 (m)
W_x	CH_2 wag	1312 (w)	1310 (w)	1308 (w)	–
W_x	CH_2 wag	1294 (m)	1293 (m)	1292 (m)	1292 (m)
W_x	CH_2 wag	1276 (w)	1271 (w)	1271 (m)	1272 (m)
W_x	CH_2 wag	1258 (m)	1255 (m)	1257 (m)	1255 (m)
W_x	CH_2 wag	1242 (w)	1237 (m)	1240 (m)	1236 (m)
W_x	CH_2 wag	1222 (m)	1218 (m)	1220 (m)	1218 (m)
W_x	CH_2 wag	1204 (w)	1200 (w)	1203 (m)	1200 (w)
W_x	CH_2 wag	1186 (w)	1180 (w)	1185 (m)	1184 (w)
S_x	C-C-C skeletal	–	*	1171 (w)	1172 (m)
P_1	CH_2 rock	719 (s) 730 (s)	721 (s)	719 (s)	719 (s)

asym – asymmetric; sym – symmetric; str – stretch; def – deformation; op – out of plane; ip – in plane; FR – Fermi resonance; vw – very weak; w – weak; m – medium; s – strong; vs – very strong.
*The region from 800 to 1150 cm^{-1} for Au is noisy due to the mica absorption peaks.

Based on systematical analysis of measured infrared spectra, it can be concluded that the compound, formed on Bi metal, is $Bi(ODT)_3$ although have somewhat lower crystallinity.

4.3.2. SNIFTIRS – in situ reflectance spectra of electrode surfaces in solutions

The external reflectance approach is the most exploited in situ infrared approach, and simply involves trapping a thin layer of electrolyte, ca. 1–25 μm, between the polished, reflective working electrode and an infrared transparent window such as ZnSe [96]. Fortunately, thin electrolyte layer neglects the study of fast redox processes. The solvent absorption is strong and needs to be annulled if the weak absorptions of near-electrode species are of interest. In 1983, Pons [97] reported data acquisition protocol, which he termed SNIFTIRS (subtractively normalized interfacial Fourier transform infrared spectroscopy), which involved stepping the potential of the reflective working electrode repeatedly between two potential values. The number of scans, collected at each step is kept low to minimize the effects of instrumental drift, whilst the required signal-noise ratio is achieved through the high number of steps. Consequently, SNIFTIRS is also restricted to electrochemical systems that are essentially reversible over the timescale of the potential modulation, but has proved extremely sensitive, and is generally reported as being surface specific, only detecting potential-induced changes in adsorbed species.

Polarized light incident upon a reflective metal electrode surface can be thought of as comprising two perpendicular components: a component polarized such that its electric vector vibrates perpendicular to the plane of incidence, and a component vibrating parallel to the plane of incidence. In essence, the work showed that the vibrations of an adsorbed molecule that are parallel to the electrode surface may become activated as a result of the electric field, and this was termed the *electrochemical Stark effect* [98–100]. As would be expected, this effect depends very strongly on the nature of the adsorbed molecule.

Our constructed experimental setup, shown in Fig. 16, is similar to the one described by Faguy and Marinković [101]. Briefly, the IR beam was directed through a ZnSe wire grid polarizer and a gold coated flat mirror to a 25.4 mm diameter ZnSe hemisphere at 34 degrees angle of incidence. Electropolished Bi electrode in solution was gently pressed against the flat side of the ZnSe hemisphere with the help of the digital micrometer. The Teflon flow-through cell was completed with also Pt wire as counter electrode and Ag|AgCl reference electrode in saturated KCl aqueous solution. As the externally reflected (and also internally reflected to some extent) IR beam was noticeably dispersed due to the inhomogeneity and surface roughness of the ZnSe hemisphere and of the Bi(001) electrode, a concave mirror was both directing and focusing the beam further to the detector chamber.

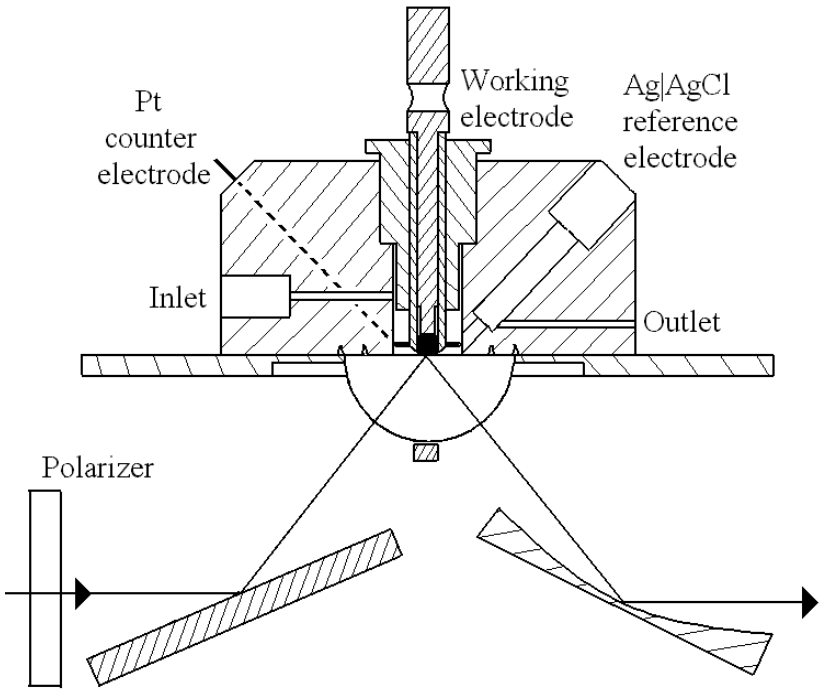

Figure 16. Constructed spectro-electrochemical cell (section view) for SNIFTRS measurements and IR beam path.

4.3.3. SEIRAS – internal reflectance through thin layer metal films

An interesting alternative method of minimizing the solution path length is to employ internal reflectance or attenuated total reflectance (ATR) at the internal surface of an infrared transparent crystal or internal reflection element (IRE) such as Ge, Si, diamond, or ZnSe. For more general applications, the IRE is coated with a thin metal film, typically ca. 20 nm [102]. At angles of incidence greater than the critical angle, total internal reflection occurs at the point of incidence on the inner surface of the IRE [96]. At the point of incidence, the incident and reflected infrared rays superimpose to form an evanescent wave that decays exponentially out from the crystal surface, through the metal layer and out into the electrolyte (Fig. 1a) [96].

The nonelectrochemical SEIRAS (surface enhanced infrared adsorption spectroscopy) effect was first reported by Hartstein and coworkers in 1980 [103]. As with the SERS (surface enhanced Raman spectroscopy) effect, SEIRAS is limited, so far, to the coinage metals [96]. SEIRAS spectra show marked enhancement of the infrared absorptions of adsorbed species, up to

40× that expected on a smooth, bulk metal electrode. A thin metal overlayer excites surface plasmon polaritons in the metal film, the strong electromagnetic fields associated with this excitation provide a sensitive probe of the metal film–electrolyte interface, with tenfold enhancement in sensitivity being claimed over the more conventional SNIFTIRS method [96].

Both the electrolyte and the metal layer will damp the evanescent wave by absorbing energy from it. Hence, it is crucial to ensure that the metal working electrode layer, whilst being thick enough to ensure metallic conduction, is not too thick that the evanescent wave is sufficiently damped it cannot sample the electrode–electrolyte interface [96]. On the other hand, thin Bi films have low conductivity. Therefore, 75–100 nm thick electroless (deposition method discussed later) or thermally deposited Bi film was used. Experiments with thicker (up to 250 nm) and thinner Bi films confirm that 90 nm is optimal thickness. Because prepared Bi films are rough, there are thinner areas where infrared beam goes through.

Our constructed system in Fig. 17 uses deposited Bi film on 10 mm diameter silicon hemisphere as a working electrode. The small glass cell also includes Pt spiral as a counter electrode, Luggin capillary for a reference electrode, and gas bubbling line for removing dissolved oxygen. The incident angle of IR beam can be changed by changing the angle of cell's base plate.

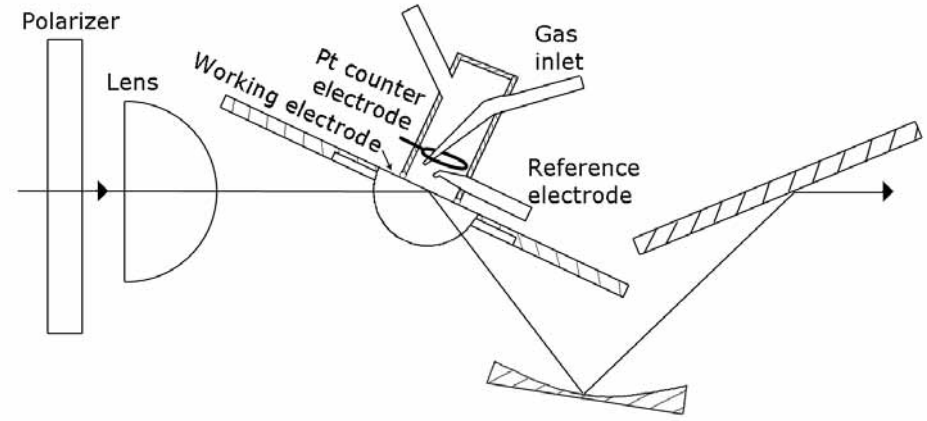

Figure 17. Constructed variable angle (55–75 deg) SEIRAS spectro-electrochemical cell with corresponding IR beam path. Working electrode is 85 nm thick Bi film deposited onto the flat side of 10 mm diameter Ge or Si hemisphere.

4.3.4. Potential-induced change in water orientation on Bi electrode

A survey of the literature reveals a number of detailed in situ infrared studies discussing the metal–electrolyte interface structure, using Pt or platinum alloys [104–106], Au[107], Ag[108], Cu[109] or Hg [110] as electrodes. However, it should be noted that the present work [6] is the first infrared reflectance study of the bismuth–electrolyte interface.

The infrared spectra of adsorbed water was studied with bulk Bi(001) and thin Bi film electrodes in $LiClO_4$ and $HClO_4$ aqueous solutions using SNIFTIRS and SEIRAS methods, respectively. The total number of scans coadded into each single beam spectrum was 1028, generated from 10 cycles of 128 scans, each collected at selected fixed electrode potential during 1 minute at a resolution of 4 cm^{-1}. The electrode was equilibrated during 30 seconds after each potential step before infrared measurements. The resulting spectra were calculated by dividing the sample with the reference spectrum and presented in absorbance units. Thus the positive-going bands represent a gain of a particular species at the sample potential relative to that at the background potential.

Surprisingly, SNIFTIR and SEIRA spectra, shown in Fig. 18, are quite different. Firstly, SEIRA spectra is 20-fold stronger. Secondly, SNIFTIR spectra indicate the decrease in amount of perchlorate anion (1105 cm^{-1}) with water solvation cell (3600 cm^{-1} and 1636 cm^{-1}) at negative potentials. Instead, SEIRA spectra indicate the change in water orientation: O-H dipole is preferably in perpendicular orientation at negative and positive surface charge densities (hydrogen down at cathodic and oxygen down at anodic potentials), whereas no peaks were detected at around zero charge potential –0.6 V where water molecules are more perpendicularly adsorbed. It has to be noted that the SEIRAS peaks measured at –1 V in 0.1 M $LiClO_4$ and 0.1 M $HClO_4$ coincide, although there is heavy hydrogen evolution in acid solution. Also, according to electrochemical measurements, perchlorate anion should adsorb on bismuth unspecifically, i.e. only with water solvation shell. Therefore, the SEIRAS method gives true spectra from Helmholz layer whereas SNIFTIR spectra describe the average diffuse layer only. The latter applies for Bi electrode with our setup, but there are other works that also prefer SEIRAS over SNIFTIR method due to truer adsorbed layer spectra [93].

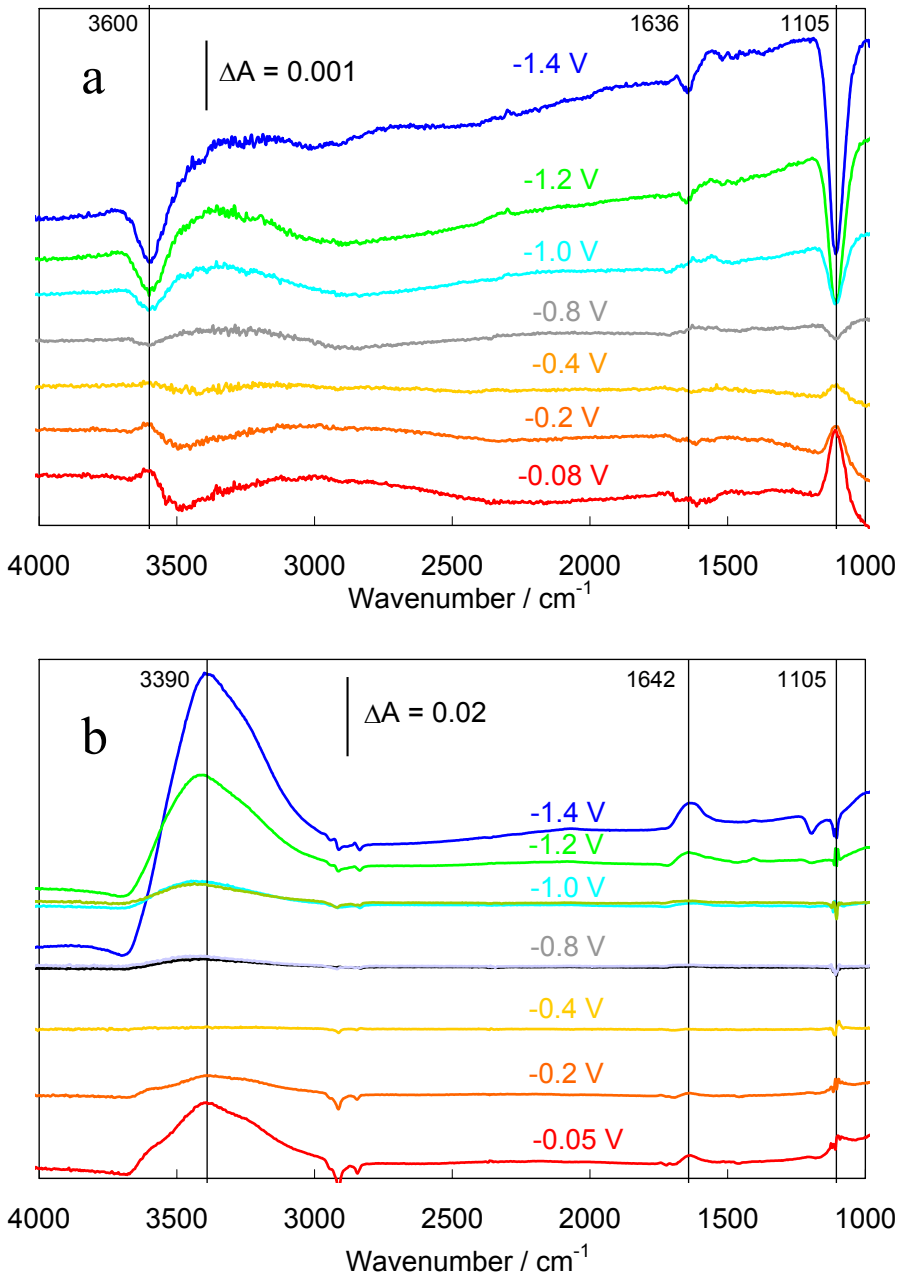

Figure 18. SNIFTIR (a) and SEIRA (b) spectra of Bi|0.1 M perchlorate aqueous solution interface at different electrode potentials. In (a) the spectra were measured with Bi(001) electrode in 0.1 M $LiClO_4$ solution with small $HClO_4$ addition (pH = 3.5). In (b) the spectra with 85 nm Bi film on silicon were measured from –1.4 to –0.8 V in 0.1 M $LiClO_4$ and from –1.0 to –0.05 V in 0.1 M $HClO_4$ solution. Background spectrum was collected at –0.6 V for all cases.

5. EXPERIMENTAL

5.1. Apparatus and reagents

The electrochemical measurements were carried out using Autolab PGSTAT 30 with a FRA 2 system. The ac voltage amplitude was 5 mV. The impedance spectra were recorded at 10 points per decade. ZView 2.3 software was used for fitting of the impedance data. Impedance at higher frequencies, affected by the geometric capacitance of cell and inductance of wires, was removed from fitting and graphs.

FTIR spectroscopy measurements were made using Perkin-Elmer Spectrum GX system with nitrogen-cooled mid-range MCT detector. The resolution was 4 cm^{-1} and the spectra were collected during 2 minutes (256 scans). The measured bands were assigned to certain vibrations with the help of density functional theory calculations with ADF2006 package using double-zeta functions and PBE and BLYP exchange-correlation potentials at the generalised gradient approximation (GGA) as well as by B3LYP method from Gaussian 03 software.

Meiji MX 8530 reflective light optical microscope was used for visualization of the thiol modified bismuth surface. Atomic force microscopy (AFM) data were obtained by Agilent Technologies™ Series 5500 measurement system using silicon nitride tips. Differential scanning calorimetry studies with Perkin-Elmer Diamond DSC machine gave information about bismuth thiolate decomposition at elevated temperatures. The structural data were obtained at room temperature by a refinement of the X-ray diffraction patterns (Difractometer DRON-1).

Stereomicroscope TZ45K and 3 Mpix camera with ScopePhoto software were used for the contact angle measurements. Contact angle θ was measured by fitting a mathematical expression to the shape of the water drop and then calculating the slope of the tangent to the drop at the liquid-solid vapour interface line

$$\theta = 2\tan^{-1}(2h/d) \qquad (5.1.1)$$

where h is the drop height and d is drop diameter [111].

Solutions for electrochemical measurements have been made from $LiClO_4$ (Sigma Aldrich 99.99%) and were saturated with electrolytic hydrogen (Barken BALSTON hydrogen generator, purity >99.9999%) during 30 minutes prior measurements. Other chemicals used were the highest purity commercially available or purified by distillation as well as by other methods.

150 nm Au(111) films on mica samples were treated with butane flame before measurements. Large atomically flat areas were confirmed with AFM images.

5.2. Electrochemical polishing of Bi and Cd

Bismuth single crystal bars were cleaved through (111) and (001) interfaces at the temperature of liquid nitrogen. Then, these pieces were processed to 4.00 mm cylinders and glued into 4.05 mm (inner diameter) borosilicate glass tube (Duran glass from Schott) using two component transparent epoxy glue. The final surface preparation of a Bi(hkl) electrode was obtained by electrochemical polishing in KI + HCl solution under positive potential at ~200 mA for 6 seconds at rotation speed 180 rpm [112–114].

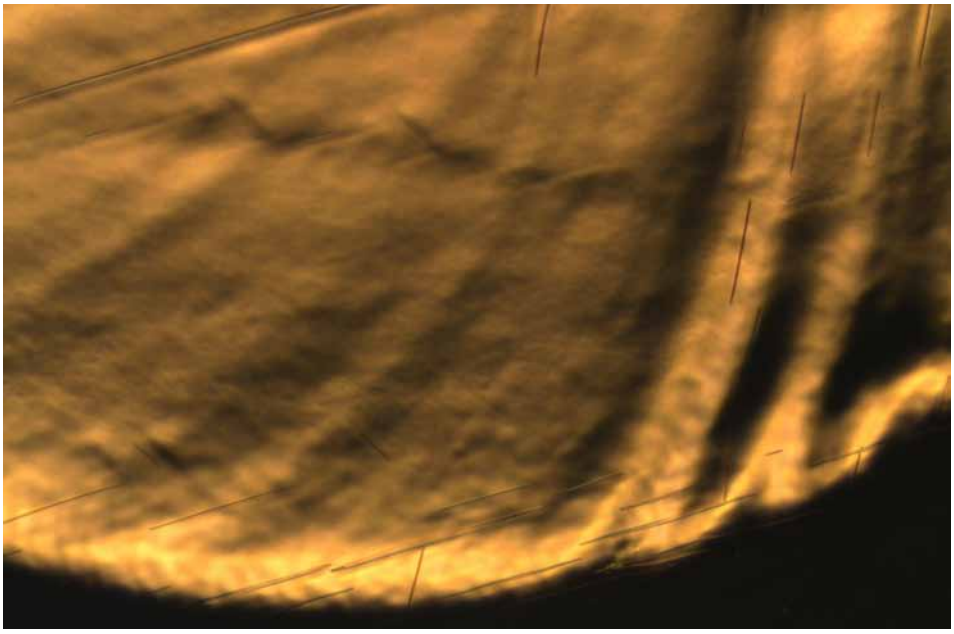

Figure 19. 1.6×1.2 mm optical microscopy (OM) image of electrochemically polished Bi(001) electrode surface. The visible waves indicate that too high polishing current was used for this electrode.

Large atomically smooth areas have been found on a cleaved and electro-polished Bi(111) surface by STM method [115]. AFM image from electro-polished Bi(001) electrode surface, taken in an air environment, indicates some roughness, probably due to the oxide layer formed.

5.3. Electrochemical measurements with macroelectrodes

The electrochemical measurements were carried out in a typical three-electrode cell using Ag|AgCl reference electrode in saturated KCl solution (all potentials mentioned in the following chapters are measured against this reference electrode) through Luggin capillary and a Pt counter electrode.

5.4. Preparation of bismuth microelectrodes

The motivation for preparation of microelectrodes was to reduce the amount of wasted Bi connected to the cleaving of 3.5 mm diameter Bi(111) macroelectrode surface (knocking with sharp knife along Bi(111) plane leads to a separation of 1–2 mm thick disk). Also, smaller electrode sizes may be used for larger scan rates in CV and higher ac frequencies can be measured with impedance spectroscopy [39]. The transport rate and, consequently, the current per unit area become very large because of the change from linear to spherical diffusion [39].

Bismuth (Mateck >99.9999%) was chosen as an electrode material and soda-lime glass as an isolator material. The Bi microelectrodes can be easily prepared by filling glass capillaries with liquid bismuth under 2 bar H_2 pressure above Bi melting point 271.3°C and then cooling down to room temperature using the cooling front toward the electrode direction at a speed of 2 mm s^{-1}. The thermal expansion coefficient for soda-lime glass (9 μm m^{-1} K^{-1}) is lower than for Bi single crystal (11.6 μm m^{-1} K^{-1} for Bi(001) and 17.3 μm m^{-1} K^{-1} for Bi(111) plane directions, correspondingly [116]) that is fortunately somewhat compensated with the fact that bismuth expands ~2.7% on solidification [117]. The nonworking electrode tip was etched in 35% HF + 10% $CuSO_4$ aqueous solution from its original size ~200 μm to ~150 μm so it could fit into the stainless steel tubing. The copper layer formed on bismuth surface helped to solder the electrode to a 100 μm isolated copper wire using low melting alloy (58% Bi and 42% Sn, T_f = 138°C) for electrical contact. Then, the copper wire and the electrode backside were inserted and glued with epoxy into 50 mm long stainless steel tube holder. The scratches around glass tube have been made by sandpaper and so BiCCE breaks easily by applying a small external force.

The scanning electron microscopy data in Fig. 20a show that the top of a nicely cleaved Bi electrode is flat. An AFM image in Fig. 20b indicates wide atomically flat areas of the Bi(111) interface having rhombohedral crystal structure [118,119]. The characteristic monoatomic lattice steps of Bi single crystal can be found between terraces.

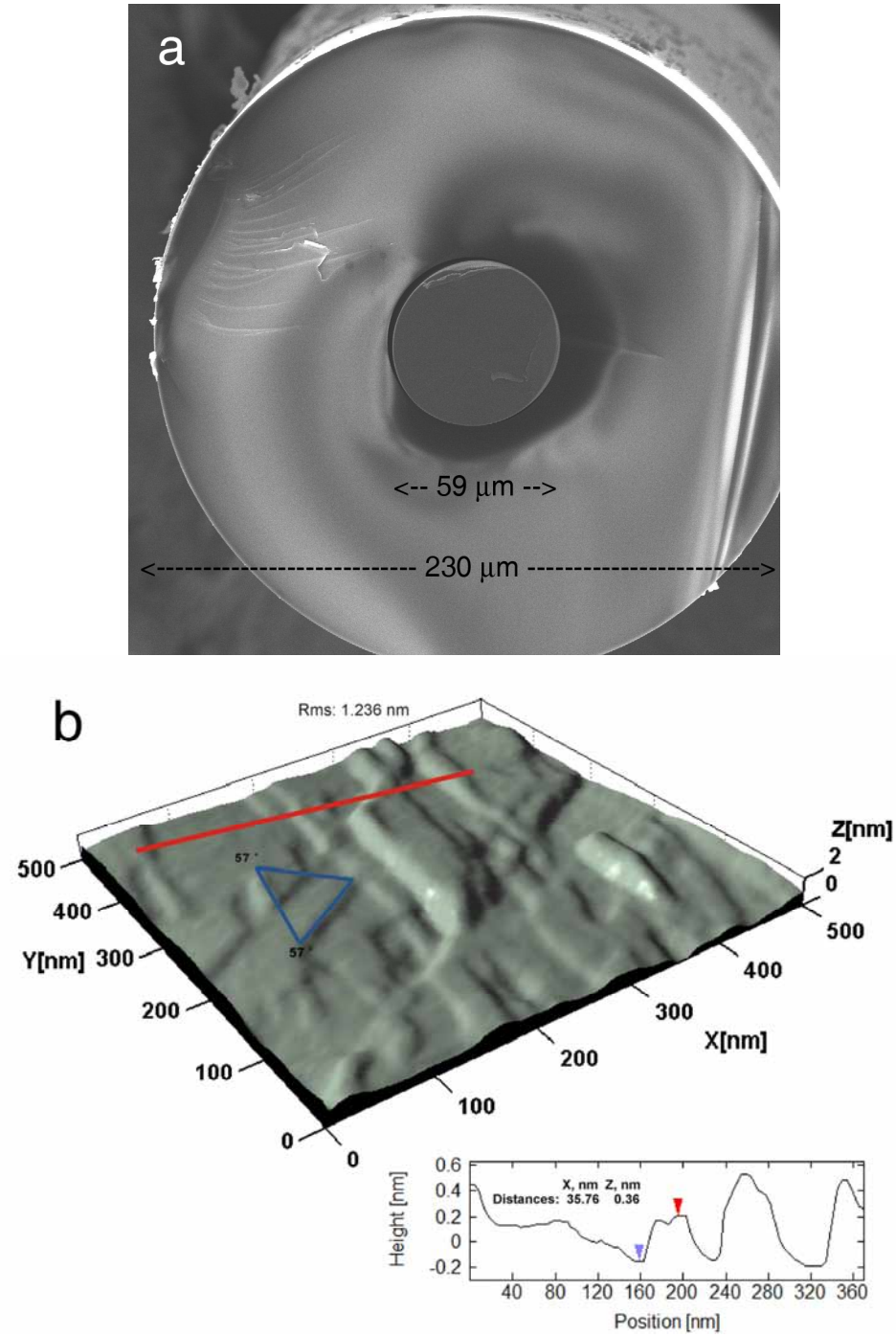

Figure 20. SEM (a) and AFM (b) images of cleaved bismuth microelectrode. The blue triangle in the AFM picture indicates the Bi(111) plane of rhombohedral crystal structure and height profile is given as the red line.

5.5. Development of renewable surface microelectrode system

It is quite inconvenient and time-consuming to take an electrode out of solution before each cleaving step while bismuth surface oxidizes in an air environment. Therefore, cleaving procedure should be carried out in an electrolyte solution under computer control.

5.5.1. I version

The cleaving of bismuth capillary electrode was carried out in a glass cell shown in Fig. 21. The measurement cell consists a small hole for Bi electrode, solution inlet, platinum wire electrode, solution outlet, and an Ag|AgCl reference electrode was connected with the cell through a Luggin capillary. By rotating a screw mechanism, the electrode moves toward. By pushing the electrode towards glass wall at ~45 deg angle, small pieces break from top of the electrode. In order to get a symmetrical cleavage, a ring scratch was made into glass capillary using a small blade covered with diamond crystals.

In principle system I can be used, but sometimes electrode was broken from wrong place and jammed into the channel. Also, in order to carry out flow injection analysis, a flow cell design was needed.

Figure 21. Photograph (12×7 mm) of the version I cell.

12

5.5.2. II version

The glass cell, shown in Fig. 22, was made from a single glass capillary. The cell volume was 50 times smaller than in version I and there was included a possibility to inject sample to the constant solution flow. Solution was deoxygenated with hydrogen and delivered into cell by syringe pump Alladin 2000. Electrode moving was automated by continuous rotating servo and Basic Stamp microprocessor. The measurement system was attached into optical microscope in order to visualize the electrode surface.

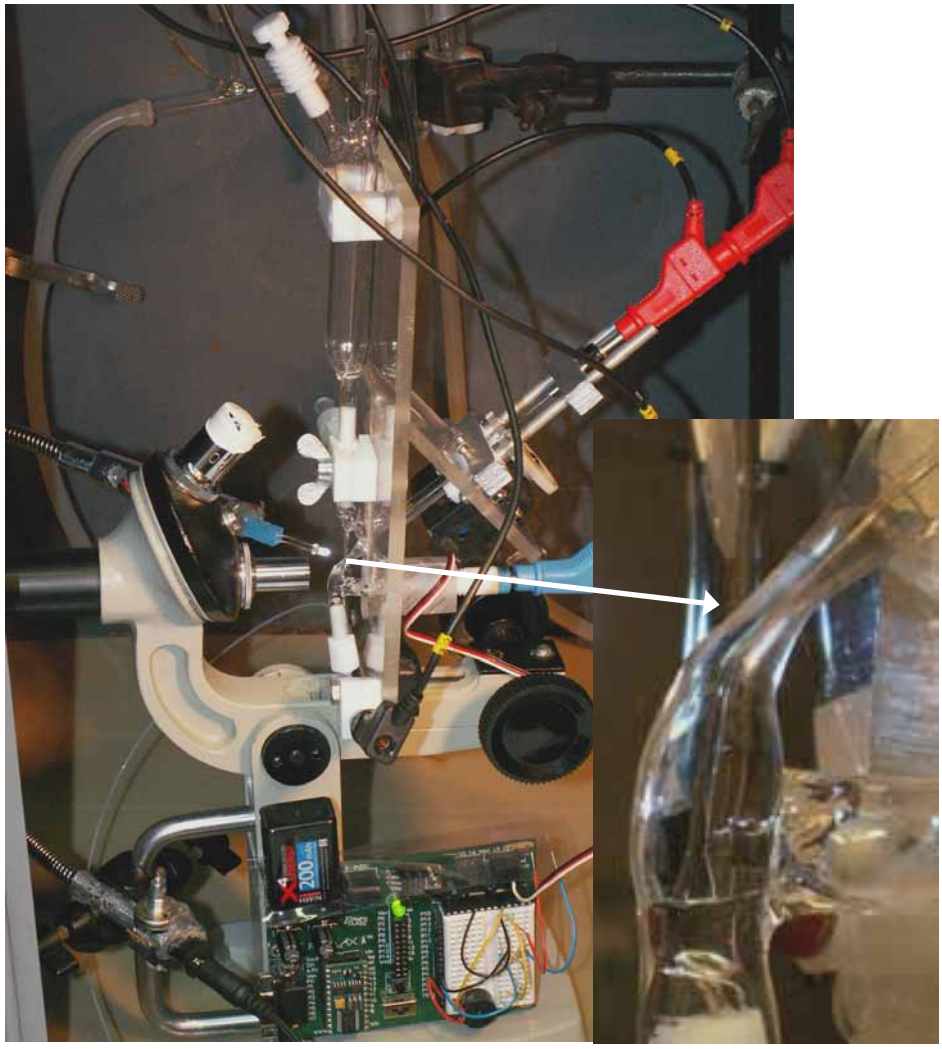

Figure 22. Photograph (30×40 cm) of the II version measurement system. Inset: magnification of the cleaving area.

Lots of measurements were carried out with system II, including flow injection experiments. However, the electrode jamming problem was even worse than with I version. After about 5 successful cleavings the electrode jammed and had to be removed from a cell. Also, in order to get higher mass-transfer rates for collection step in heavy-metal analysis, the solution flow should have opposite direction. Due to the complicated shape of glass cell, the optical microscope images were of low quality. Because of the cell geometry, only as high as 2 mm long cylinders were broken from top of the Bi electrode. Electrode bending before cleaving caused the resulting electrode isolation leakage. System II was quite large too.

5.5.3. III version

The glass cell was made from two microscopy glass slides like it has been described in Refs. [120] and [121] except, the channels in our system were made with diamond cutting disc. The bismuth cleaved capillary electrode (BiCCE) is moving in a channel inside glass chip with the help of a home-made linear positioner (Fig. 23).

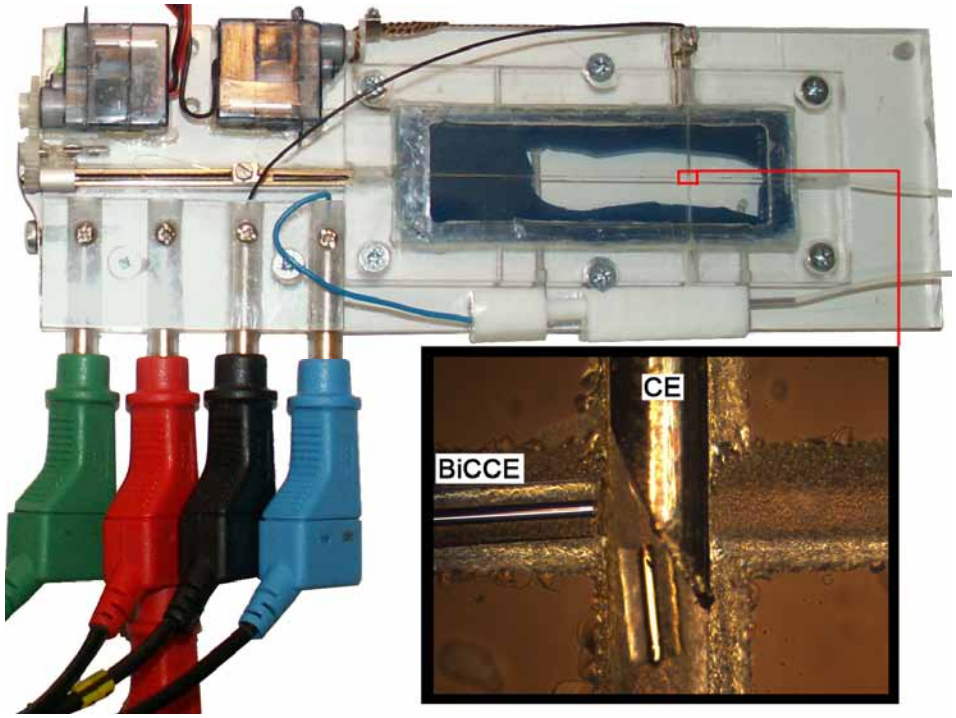

Figure 23. Photograph (18×9 cm) of the BiCCE measurement system. Inset: BiCCE cleaving procedure (1.6×1.2 mm) under optical microscope.

An actuator is also moving a needle so that every time a 320 μm long cylinder breaks and a new Bi surface is formed as it is seen under optical microscope (inset of Fig. 23). The broken piece is going downstream with solution flow (delivered by syringe pump Aladdin 2000) and the needle that is also a counter electrode moves back. This process can be repeated ~150 times until the end of the electrode. Electrode renewal is automated with the help of 8-core Propeller processor and can be initiated from PC computer or infrared remote control.

No electrode jamming occurred in version III cell. High mass-transfer rates can be achieved by placing a glass capillary nozzle close to the electrode surface. Additionally, temperature control is possible and high quality microscope images can be taken using transmission or reflectance methods. System III is small and suitable for mass production. However, we have to note that not every cleaving yields a good quality single crystal electrode surface, because sometimes the sides of the electrode may be exposed to solution. Thus, the quality of the electrode isolation still needs some further development.

5.6. In situ preparation of rough Bi surfaces

For preparation of porous bismuth electrode, BiCCE was held at a potential of +1 V for 1 s followed by immediate potential switch to –2 V for 0.5 s. Then, the potential was fixed at –1.2 V and the syringe pump was regulated to a higher flow rate of 5 mL per hour for 10 s in order to remove the unreacted Bi^{3+} ions from the solution. A small part of Bi electrode dissolved at +1 V and formed an oversaturated solution of BiO^{+} cations near the electrode surface. By applying potential step to –2 V, reduction of these ions occurred, and the formation of black sponge was visible under optical microscope having much larger volume than the volume of Bi dissolved during the oxidation step. SEM data in Fig. 24 show that different morphologies coexist inside porous Bi, like ~800 nm large pyramidic Bi crystals as well as dendrites created of ~60 nm diameter Bi nanowires [2].

During a few minutes after preparation, the volume of freshly formed bismuth sponge collapses twofold (detected by visual inspection through microscope) and the surface area reduces about 50% based on the values of capacitance measured. It was observed that the surface area of porous Bi decreases further during some hours, although to a smaller extent.

The shape of C_s,E-curve for porous Bi is similar to that of smooth Bi electrodes; however, porous Bi has larger hydrogen overpotential.

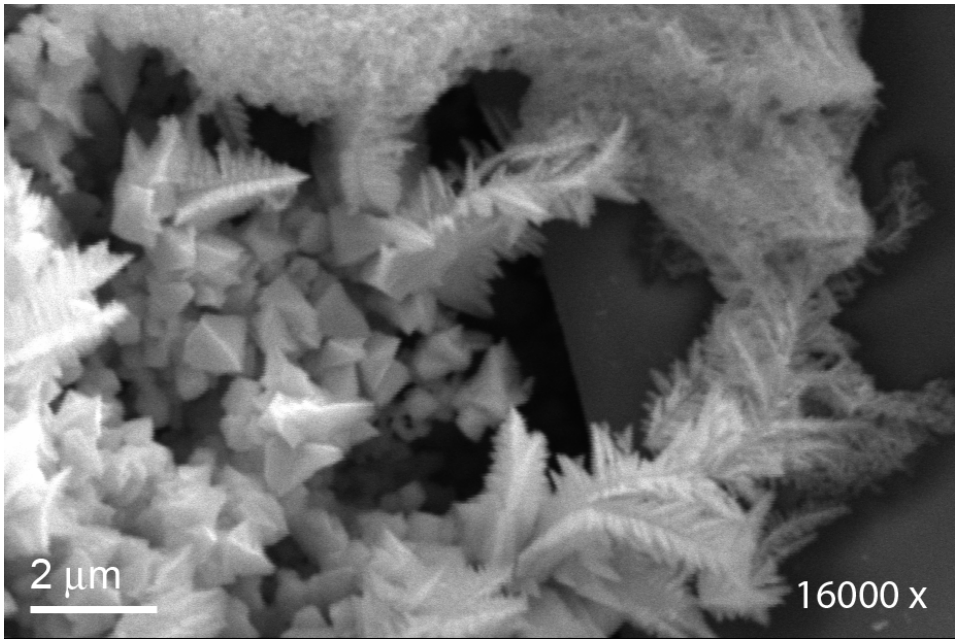

Figure 24. SEM image for BiCCE after dissolution and electrodeposition steps.

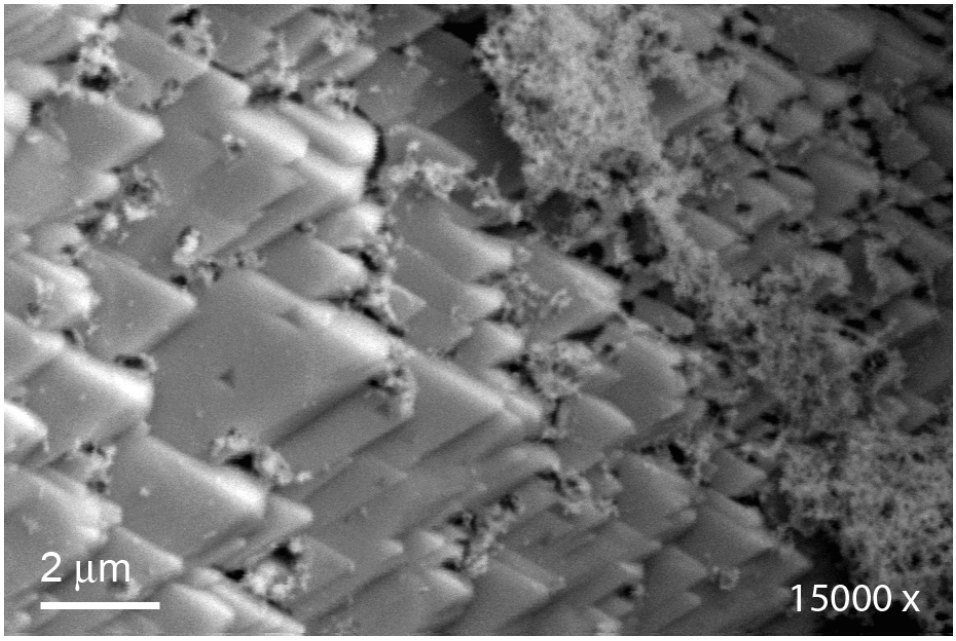

Figure 25. SEM image for BiCCE after 5 min holding at –2.2 V in 0.1 M $LiClO_4$ aqueous solution.

In a second experiment, BiCCE was held for five minutes at E = –2.2 V in 0.1 M $LiClO_4$ solution, and SEM images of the resulting surfaces, given in Fig. 25, indicate the presence of porous Bi layers on smooth Bi surface [2]. The structured area under dispersed Bi in Fig. 25 is not characteristic of a cleaved bismuth surface [1,115] but rather to a chemically or electrochemically etched surface of Bi.

5.7. Electroless deposition of Bi thin films or nanoparticles

Our motivation to deposit pure Bi thin films was the intention to prepare working electrode material for SEIRAS measurements. Therefore, a Bi film preparation method was developed [4]:

0.4 mg of Bi_2O_3 was heated with 2 drops of 30% HF in a PTFE beaker in a hot plate until the yellow oxide turned to a white bismuth(III)fluoride. Next, 2 mL of water was added and the PTFE beaker was heated at 90°C during 2 minutes in order to dissolve Bi salt (about 0.4 mM Bi^{3+} in 1.2 M HF, solid BiF_3 was in excess) and also to remove most of the dissolved gases. Thereafter, 0.5 mL of formed solution with chosen temperature was quickly dropped onto a polished Si(111) wafer. First, SiO_2 layer on silicon surface dissolved in HF during 5–10 seconds. A yellow Bi film formed according to the reactions:

$$SiF_6^{2-} + 4e^- = Si + 6F^- \qquad -E^0 = 1.24 \text{ V [122]} \qquad (5.7.1)$$

$$Bi^{3+} + 3e^- = Bi \qquad E^0 = 0.308 \text{ V [122]} \qquad (5.7.2)$$

$$3Si + 18F^- + 4Bi^{3+} = 3SiF_6^{2-} + 4Bi \qquad E^0 = 1.548 \text{ V} \qquad (5.7.3)$$

The reaction may proceed from 30 seconds to 10 minutes to provide a uniform coating. At higher temperatures, it is necessary to add more of prepared solution for few times due to the evaporation of solution and consumption of Bi^{3+} ions. Finally, the substrate was washed with MilliQ+ water and desiccated in an argon gas flow.

The thickness of bismuth film can be controlled by the synthesis temperature. Average thickness was calculated by weight difference of Bi coated and uncoated Si wafer (bismuth films were dissolved in 50% HNO_3 in a few seconds). For example, deposition during 10 minutes at 65°C gave 215 nm, 25 minutes at 25°C 100 nm, and 10 minutes at 25°C 74 nm thick Bi film, respectively. Deposition during 2 min at 25°C gave only separated Bi nanoparticles at Si(111) surface (calculated average thickness ~30 nm).

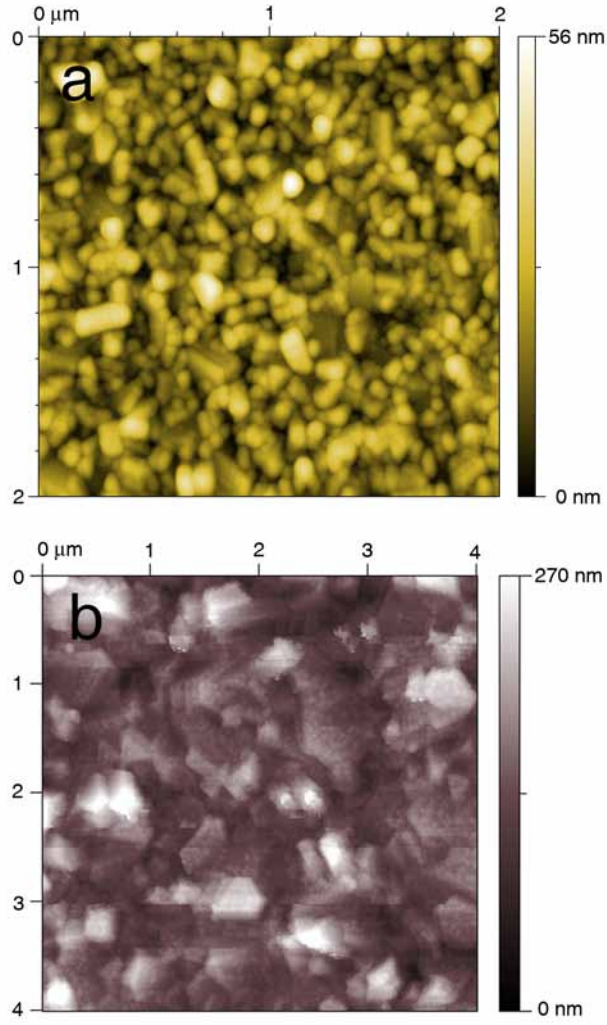

Figure 26. AFM images of bismuth deposits on Si(111): a) 30 nm average thickness (deposition time 2 min at 25°C), b) 215 nm thick Bi film (10 min at 65°C). RMS values 8.1 nm and 51.6 nm have been calculated, correspondingly.

AFM images for bismuth films, measured at different stages of deposition, help to understand how the film forms. At the beginning of the reaction, hemispherical Bi nanoparticles grow on a silicon surface (Fig. 26a). Thereafter, the larger Bi grains start to form due to the growing and joining together of smaller particles, meanwhile the silicon dissolution still takes place. Finally, up to 700 nm wide bismuth crystals are joined to a continuous film (Fig. 26b) and the reaction ceases as silicon is not exposed to the solution any more.

XRD pattern search-match analysis [4] showed that the film formed on Si(111) substrate is well crystallized rhombohedral Bi [122,123]. The Bi

structure is preferentially oriented in (111) plane, but some other crystallographic orientations were also detected in the diffraction pattern. The ordering of Bi crystals is much lower during the first stages of the film growth.

XPS spectra indicate the existence of about 2 nm thick bismuth(III)oxide on the freshly prepared Bi film surface [4]. Raman spectra peaks correspond to monoclinic α-Bi_2O_3 oxide layer [124,125]. Argon ion bombardment experiment showed that there was a pure bismuth film on silicon side, no silicon dioxide or bismuth silicide was detected.

Four-point resistivity measurements gave the following surface resistivities: 0.32 mΩ cm for 215 nm and 0.60 mΩ cm for 74 nm thick Bi films, respectively [4].

Prepared Bi thin films have yellowish colour and emit visible photoluminescence [4].

6. RESULTS AND DISCUSSION

6.1. Electrochemical properties of bismuth electrodes in aqueous solutions

Bismuth oxidizes in an air environment, but the ~2 nm thick Bi_2O_3 layer formed [4] reduces at cathodic potentials (E < –0.4 V vs. Ag|AgCl). Bismuth has large IPR: from –1.2 to –0.4 V in 0.1 M $LiClO_4$ aqueous solution [2]. According to E,pH graph for Bi, the dissolution of Bi into BiO^+ starts at E > 0.2 V and higher valence compounds may form at even higher potentials depending on the value of solution pH [126]. At E < –1.2 V, hydrogen evolution begins

$$H_2O + e^- \leftrightarrow H_{ads} + OH^- \text{ (slow)} \quad (6.1.1)$$

$$H_{ads} + H_2O + e^- \rightarrow OH^- + H_2 \text{ (fast)} \quad (6.1.2)$$

At even more negative potentials (E < –2 V), there is also a side reaction, gaseous bismuth hydride formation, which leads to the controlled dissolution of Bi surface [2]:

$$Bi + 3H_{ads} \leftrightarrow BiH_3\uparrow \text{ (side reaction)} \quad (6.1.3)$$

BiH_3 decomposes quickly and forms bismuth nanoparticles that deposit back onto the bismuth electrode surface.

$$2BiH_3 \rightarrow 2Bi\downarrow + 3H_2$$

In 0.1 M $HClO_4$ solution, Bi electrode has IPR from –0.75 to 0 V. HER at Bi electrode is believed to be limited by the rate of step (6.1.4) followed by the fast electrochemical hydrogen desorption step (6.1.5) [71]:

$$H_3O^+ + e^- \leftrightarrow H_{ads} + H_2O \text{ (slow)} \quad (6.1.4)$$

$$H_{ads} + H_3O^+ + e^- \rightarrow H_2O + H_2 \text{ (fast)} \quad (6.1.5)$$

The formation of electric double layer with addition of unspecifically adsorbing salt ($LiClO_4$ or Na_2SO_4) decreases the activity of hydrogenated protons near surface and therefore the rate of hydrogen evolution decreases [11]. Hydrogen evolution is totally irreversible for both proton and direct water reduction mechanisms.

14

Bi single crystal can be easily cleaved along (111) or (001) planes, but the smooth surface for Bi single crystal electrodes can be also achieved by electropolishing in HCl + KI solution. Bi(001), Bi(111) as well as porous Bi have similar capacitance value, which is very sensitive to the addition of organic compounds in solution [1,9,13–15]. The capacitance of single crystal as well as porous Bi electrodes in $LiClO_4$ solution in IPR does not depend on ac frequency [2]. Chemical impurities on the surface or isolation leakage cause CPE exponent α variation from 0.92 to 0.99. It was found that porous bismuth has more than hundred mV higher hydrogen evolution overpotential than smooth Bi electrodes [2].

Two of bismuth single crystal planes, Bi(111) and Bi(001), have the most distinct properties of all bismuth single crystal planes. Bi(111) has 96 mV more negative zero charge potential than that for Bi(001) [54], but these effects appear only at the conditions of strong adsorption. For example, desorption of pyridine from Bi(111) surface takes place at about 100 mV more negative potential than from Bi(001) [1,14,15].

6.2. Bismuth electrode interaction with alcohols

There are plenty of studies analyzing organic compounds adsorption on Bi electrode [13–15,69,127–130], because Bi behaves electrochemically similarly to poisonous Hg and is therefore a good system for studying adsorption processes. This work was a part of the project devoted to the study of the influence of the organic molecule structure on the adsorption behaviour at the Bi|solution interface [13–15,69,127–130].

Under electrochemical control, it is possible to study the adsorption of organic compounds directly onto the metal surface. Without electrochemical control in an air environment, bismuth is covered with thin layer of Bi_2O_3. However, simple surface modification without electrochemical control is also important because it can be used in practical applications.

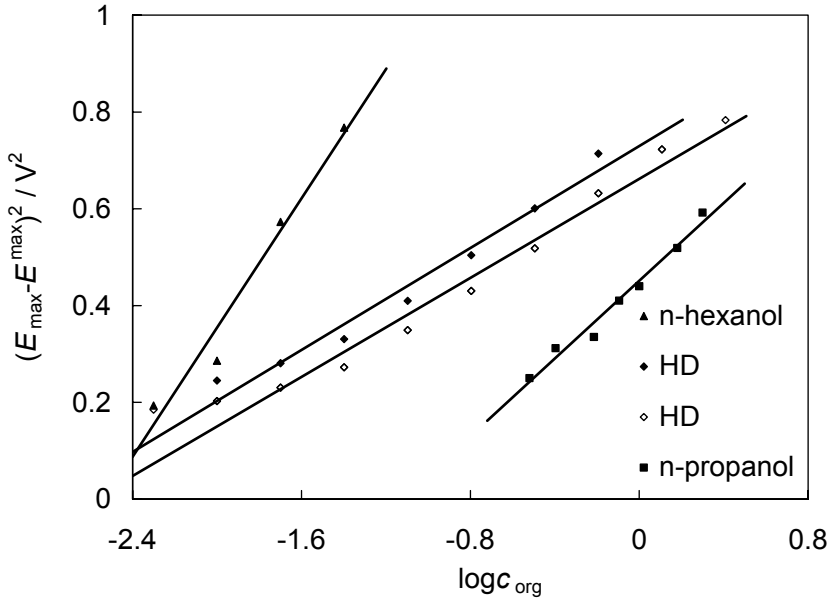

Figure 27. Dependence of the difference between the potential of adsorption-desorption maximum E^{peak} and the zero charge potential $E_{\sigma=0}$ on log$c$ at Bi(111) (filled marks) and at Bi(001) (open marks) for various organic compounds, noted in figure.

Primary alcohols adsorb on bismuth surface with the hydrocarbon chain oriented towards the electrode and polar hydroxyl group pointing out to the solution [129,130]. Because 1,6-hexanediole (HD) has two terminal hydroxyl groups, it should adsorb differently. The adsorption parameters for HD were obtained using similar calculation methods than for *n*-hexanol [130] and *n*-propanol [129]. The values of molecular surface area indicate that HD adsorbs flatly on Bi single crystal electrode surfaces (it was previously found that HD adsorbs flatly on Hg [131]). Adsorbed HD molecules do not participate in direct charge transfer processes. Data from Fig. 27 indicates that at low concentrations n-hexanol is also adsorbed flatly.

Analysis of infrared and electrochemical data demonstrates that at negative surface charge densities there are no chemisorbed particles on the bismuth|ethanol solution interface [7]. Differently from platinum|electrolyte interface, no ethanol oxidation products were detected [7]. Absorption peaks in the measured infrared spectra were mainly caused by the variation of solvated perchlorate anion adsorption due to the change of surface charge density with the variation of bismuth electrode potential [7].

6.3. Formation of the bismuth thiolate compound layer on bismuth surface

In electrochemical literature, there is one study reporting the formation of self-assembled hexadecanethiol and other thiol monolayers on bismuth surface [132]. In this article, there is no data about the thickness of the thiol layer formed at bismuth electrode and this layer was characterised only by its diffusion blocking properties of electroreduction reaction of daunomycin and picric acid at bismuth electrode surface [132].

Surface modification with thiols has been made by keeping the Bi single crystal electrode in 1mM thiol solution in 96% ethanol for 24 h, which is a typical procedure for preparing self-assembled monolayers on gold [34–38]. Then, the electrode was thoroughly washed with 10 mL of ethanol and dried. The modification of hydrophilic Bi with hydrophobic thiols can be easily proved by contact angle measurements in Fig. 28.

Optical microscopy data for the ODT modified Bi(001) surface, given in Fig. 29, shows that a few μm thick nonuniform layer of bismuth thiolate compound has formed during holding bismuth in ODT solution [8]. Image in Fig. 30 was taken after 2 cyclic voltammetry cycles between –1.6 and –0.45 V. It is apparent that part of the thiolate long crystals was reduced to thiol and can be seen as visible droplets on the surface.

The exact amount of deposited compound can be calculated from cyclic voltammetry data. The thiol-modified electrode was immersed into solution at –0.7 V and left to stabilize of current density during 30 minutes. The first excursion to the cathodic potentials creates a very large reduction peak with an area –1350 μC cm^{-2} (Fig. 31). For 1-octadecanethiol monolayers on gold, –83 μC cm^{-2} reductive desorption peak was observed [34]. According to the data in Fig. 31, the reduction process is totally irreversible because there is no peak in the second voltammogram.

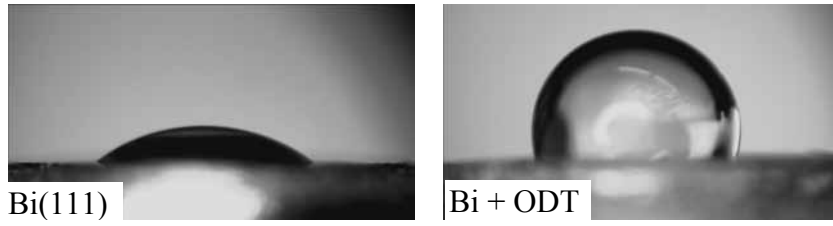

Figure 28. Contact angle measurement data for electropolished Bi(111) before and after modification with ODT.

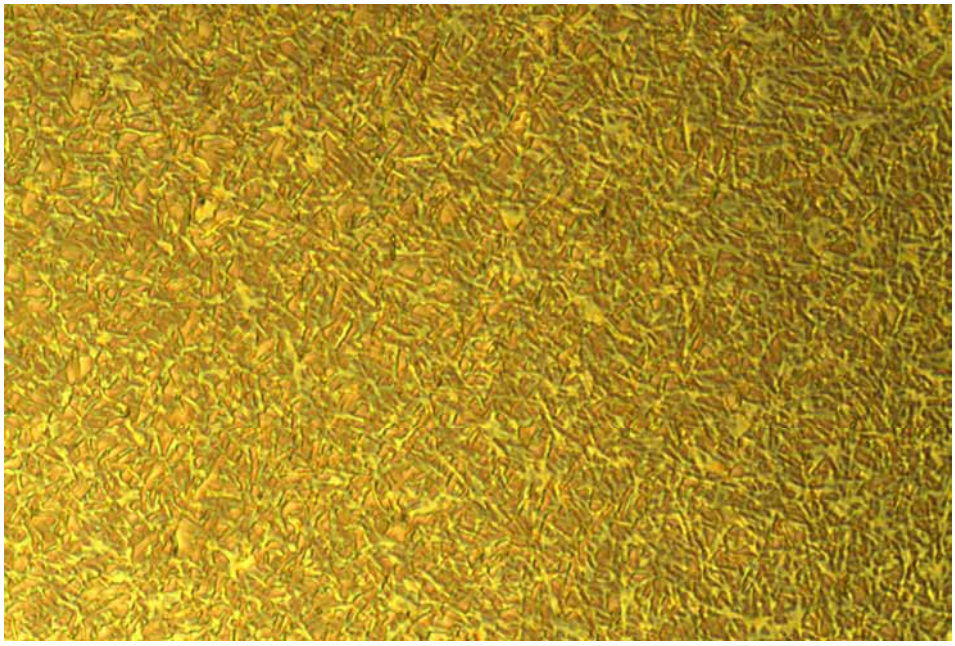

Figure 29. 120×75 μm optical microscopy (OM) image of Bi(001) electrode after modification with ODT solution.

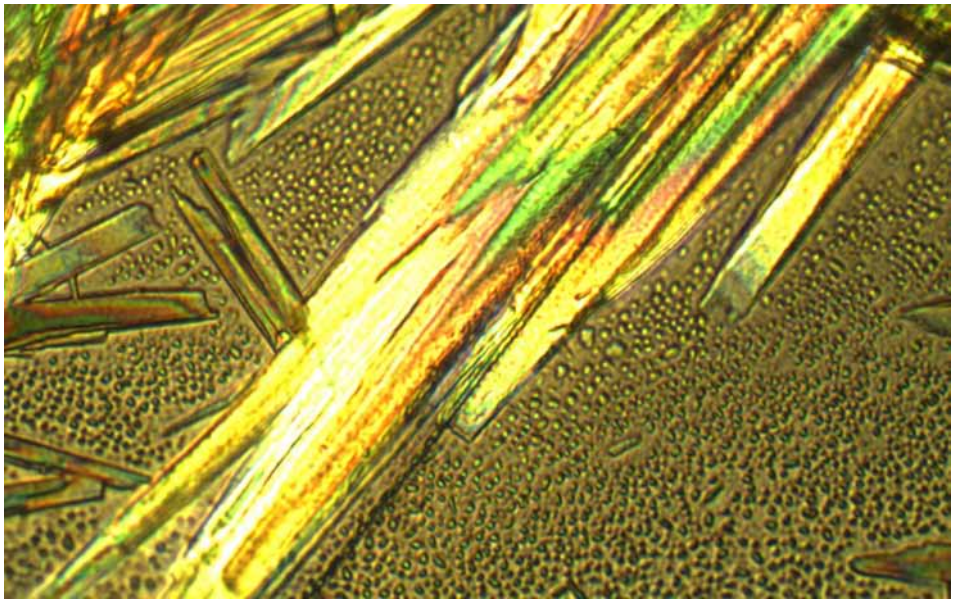

Figure 30. 120×75 μm OM image of decanethiol modified Bi electrode (1mM thiol, 24h) after electroreduction step. The long crystals correspond to tris(1-decylthio)bismuthine and the liquid drops to decanethiol, formed during electroreduction.

15

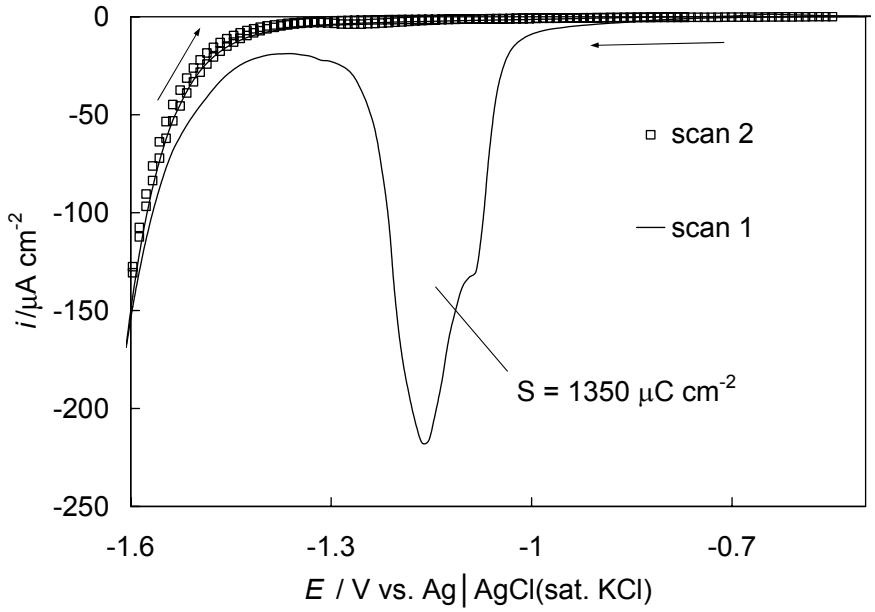

Figure 31. Cyclic voltammograms at potential scan rate of 20 mV s^{-1} for Bi(001) interface modified with ODT solution, measured in 0.1 M $LiClO_4$ aqueous solution.

During the first potential cycle, all $Bi(ODT)_3$, deposited on the electrode surface, reduced to bismuth and corresponding thiol [8]. However, the electrochemically inactive (in the region –1.6 V < E < –0.4 V) thiol stays on the Bi(001) surface as capacitance at –0.7 V for thiol modified electrode is only 0.1 μF cm^{-2} and after excursion to –1.6 V and back the capacitance value has not changed at all. Compared to a value of differential capacitance 19 μF cm^{-2} corresponding to a Bi(001)|0.1 M $LiClO_4$ interface at E = –0.7 V and to the limiting capacitance value from 2 to 5 μF cm^{-2} for Bi(001)|concentrated organic alcohol aqueous solution interface [13–15,9], it is clear that there is a thick layer of organic compound, characterised with the very low dielectric constant, adsorbed on Bi(001) surface.

It should be noted that if the yellow crystals of $Bi(DT)_3$ at Bi(001), seen partially in Fig. 30, are dissolved by rinsing very thoroughly with ethanol ($Bi(DT)_3$ crystals are slightly soluble), the electrode gives a very small area reduction peak (with charge density only ~ –10 μC cm^{-2}) during first cycle of cyclic voltammetry scan. No sharp reduction peak is observed that would be expected for a well ordered monolayer of electroactive compound.

To study the kinetics of thiol layer formation process at Bi, the electrode was immersed into 1 mM ODT solution in deoxygenated ethanol and was bubbled with hydrogen during thiolate deposition process also. The dependence of cyclic voltammetry peak area q (i.e. destructive reduction charge density) on deposition time is logarithmic with equation q = 93 ln(t) + 28 [8]. Thus, even after

holding the Bi(001) electrode only during a few seconds in thiol solution, there is more than a monolayer of electroactive compound on the Bi(001) surface.

6.3.1. Dependence on thiol structure

The formation of thick thiol layers on Bi electrode raised some new questions: maybe there are some other thiols that form stable monolayers on bismuth? Thus, further studies were carried out with different 1 mM thiol ethanol solutions where Bi electrode was dipped. Nevertheless, all thiols and carboxylic acids tested form thick Bi thiolate (or carboxylate) layer that was proved by OM pictures and infrared spectroscopy measurements. Comparison of organized thiol monolayers on gold (Table 6) shows that the contact angle values for dithiols (B13DT, ODIT) and MHDA are different for Bi and Au electrodes, indicating to a different orientation of these thiols on Au and Bi.

Table 6. Contact angle measurements using the shape of water drop, calculated according to equation 5.1.1.

Compound | modification time	Au(111)	Bi(111)
–	67	17 (23^{MP})
1-octadecanethiol (ODT) | 24h	101	106
1-octadecanoic acid (STEAR) | 24h	75	88
16-mercaptohexadecanoic acid (MHDA) | 24h	23	56
1,3-benzenedithiol B13DT | 24h	77	27
3,3,4,4,5,5,6,6,7,7,8,8,9,9,10,10,10-heptadecafluoro-1-decanethiol (FDT) | 24h	104	99
1,8-octanedithiol (ODIT) | 24h	63	22

MP – mechanically polished

Bismuth interacts with 1-decanethiol even faster than with 1-octadecanethiol and eventually collects most of the thiol from the solution to form the yellow by colour tris(1-decylthio)bismuthine fiber-like crystals on the electrode surface. Formed bismuth thiolates are yellow, exept compound with B13DT, which is red (image in Fig. 32).

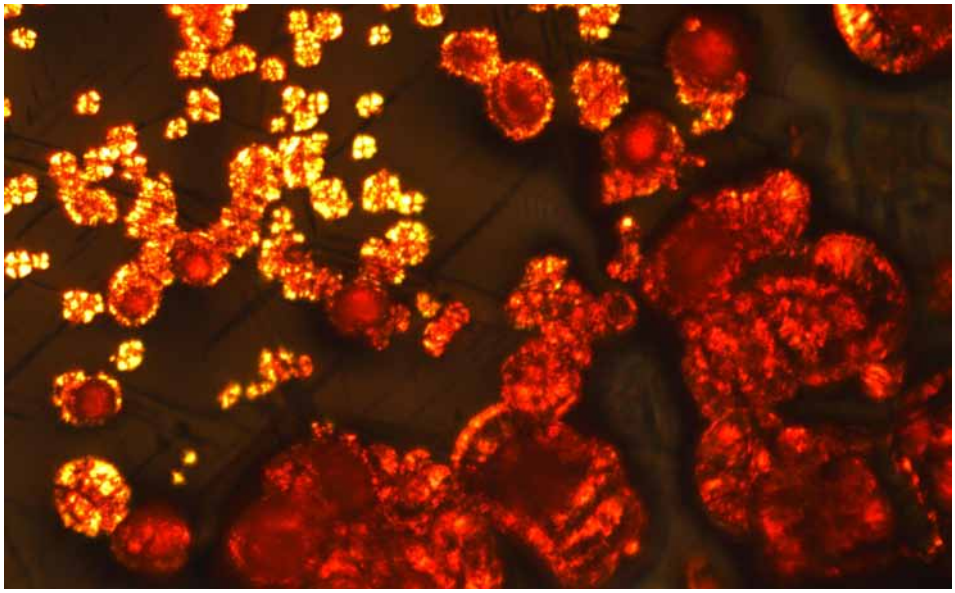

Figure 32. 780×500 μm optical microscopy images of Bi(111), modified with 1mM B13DT ethanol solution for 100 hours.

6.3.2. Synthesis and properties of bismuth thiolates

The existence of bismuth thiolates $Bi(SR)_3$ (where R is phenyl, butyl or some other hydrocarbon chain) is known for a long time however few of them have been synthesised yet [133,134]. We prepared bismuth thiolates by two different methods:

1) 1.24 g ODT was dissolved in 160 mL ethanol in a round flask. 0.455 g $BiCl_3$ was dissolved in 10 mL ethanol by adding 2 drops of concentrated HCl. The thiol solution was stirred with argon bubbling. The $BiCl_3$ solution was added with the help of syringe pump during 10 hour period. The formed orange solid, shown in Fig. 33, was filtered, washed with ethanol and dried. Yield was 85% and the melting point of this compound was 81°C. Gravimetric analysis [8] showed that the formed compound contained 22.1 ± 1% Bi and has empirical formula $Bi(ODT)_{2.6}$. Bismuth(III) compounds are stable, but Bi(II) or Bi(I) are not, thus, the insertion of Cl^- ions into the product is possible. Therefore, we developed another method for the synthesis of bismuth thiolates.

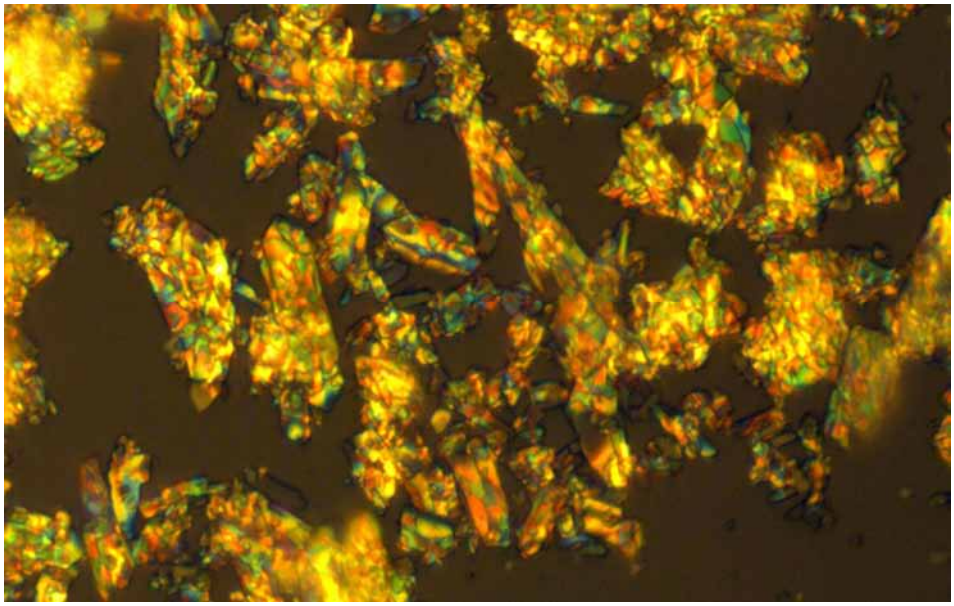

Figure 33. OM image (157×100 μm) of $Bi(ODT)_{2.6}$ crystals, prepared from $BiCl_3$ and ODT in ethanol.

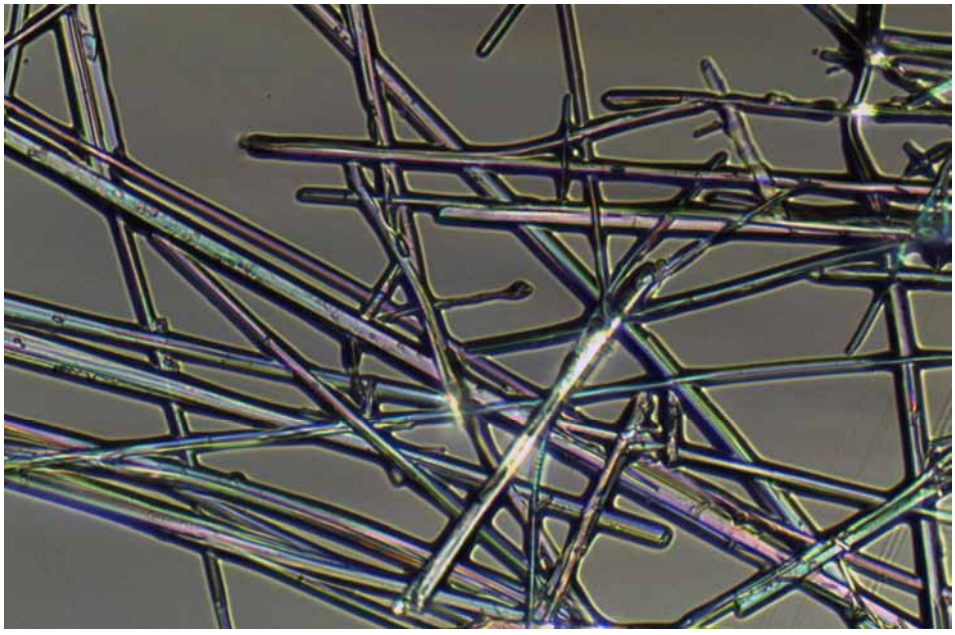

Figure 34. OM image (157×100 μm) of $Bi(ODT)_3$, prepared from Bi_2O_3 and thiol in hexanol (darkfield contrast).

16

2) 0.5 g Bi_2O_3 and 0.807 g of ODT were heated at 65°C in 70 mL hexane during 24 h in a closed vessel. Thereafter, the hot yellow solution was decanted to another bulb to remove the excess of Bi_2O_3. Upon cooling down a system with a rate of 5°C per hour a bright yellow precipitate formed, practically insoluble in acetone and ethanol. According to the results of elemental analysis it contains 19.5 ± 1% Bi (the calculated value of Bi in $Bi(ODT)_3$ is 19.6%) and thus the new compound synthesised is tris(1-octadecylthio)bismuthine (yield 75%, melting point 82°C). The $Bi(ODT)_3$ II looks like a yellow cotton wool, and contains of up to cm long fibres (Fig. 34). These fibres are round with diameters from 1 to 5 micrometers, while the maximum length of these fibres depends on the size of the reaction bulb.

According to quantum chemical modelling data for a $Bi(ODT)_3$ molecule, the angle between S-Bi-S bonds is 94 degrees. However, hydrocarbon chains have many possible configurations. It is quite unrealistic that the configuration of hydrocarbon chains, given in Fig. 35, can exist in crystalline phase. However, in soluble form the solvation may stabilize this shape.

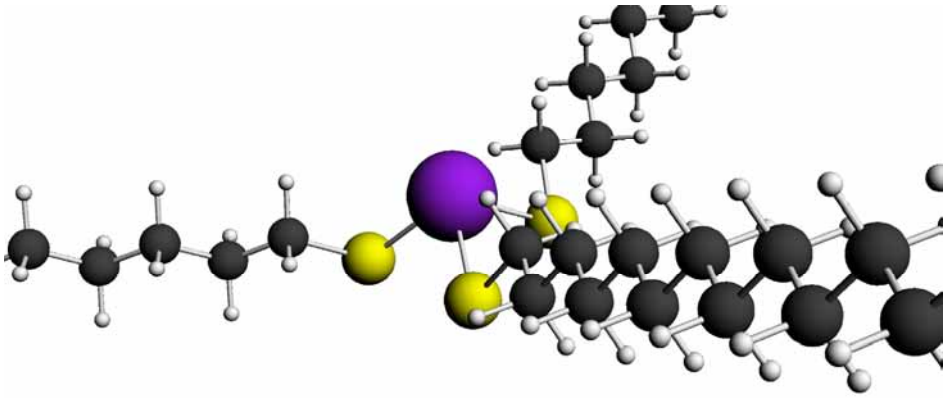

Figure 35. Optimized geometry for a single $Bi(ODT)_3$ molecule calculated with PBE functional from ADF software package (Bi – purple, S – yellow, C – black, H – white).

Indeed, bismuth thiolate is soluble in hexane, while other metal-thiolates (AuODT [95], AgODT [94]) are insoluble in all kinds of solvents.

Infrared spectra for $Bi(ODT)_3$ and $Bi(ODT)_{2.6}$ crystal forms were taken using a small silicon ATR element. The derivative spectra reveal that $\delta(CH_2)$ and P_1 peaks for $Bi(ODT)_{2.6}$ are split unlike single peaks for $Bi(ODT)_3$. Thus, the $Bi(ODT)_{2.6}$ has orthorhombic sub-cell, but $Bi(ODT)_3$ has monoclinic or triclinic packing. There are medium intensity peaks at 1416 cm^{-1} and 1428 cm^{-1} for $Bi(ODT)_{2.6}$ but at 1420 cm^{-1} and 1432 cm^{-1} for $Bi(ODT)_3$. Peak at 1071 cm^{-1} exists only for $Bi(ODT)_{2.6}$, but there is a wide peak at 1028 cm^{-1} for $Bi(ODT)_3$. Also, there are differences in frequencies and intensities of other S_x and P_x series peaks.

XRD measurements indicate that both $Bi(ODT)_3$ I and II are well crystalline solids. However, I and II have completely different peak positions in XRD spectra Fig. 36) and, thus, different crystallographic structure. Also, inset of Fig. 36 indicates the three overlapping peaks for $Bi(ODT)_3$ I. Thus, $Bi(ODT)_3$ I contains three different crystal fractions with lattice constants 5.13(1) nm (dominant form), 5.06 nm (twice smaller amount), and 4.99 nm (again twice smaller amount). The difference between lattice constants is 0.07 nm. The $Bi(ODT)_3$ II has only one crystalline phase with lattice constant c = 4.41(2) nm (this parameter was obtained with more precise SAXS method). According to the quantum chemical calculations, the size of $Bi(ODT)_3$ molecule in Fig. 35 is 4.5 nm and a single ODT-Bi fragment is 2.6 nm long. Therefore, $Bi(ODT)_3$ molecules in II crystals can indeed have orientation similar to Fig. 35 while in synthesis product I the hydrocarbon chains have more linear configuration.

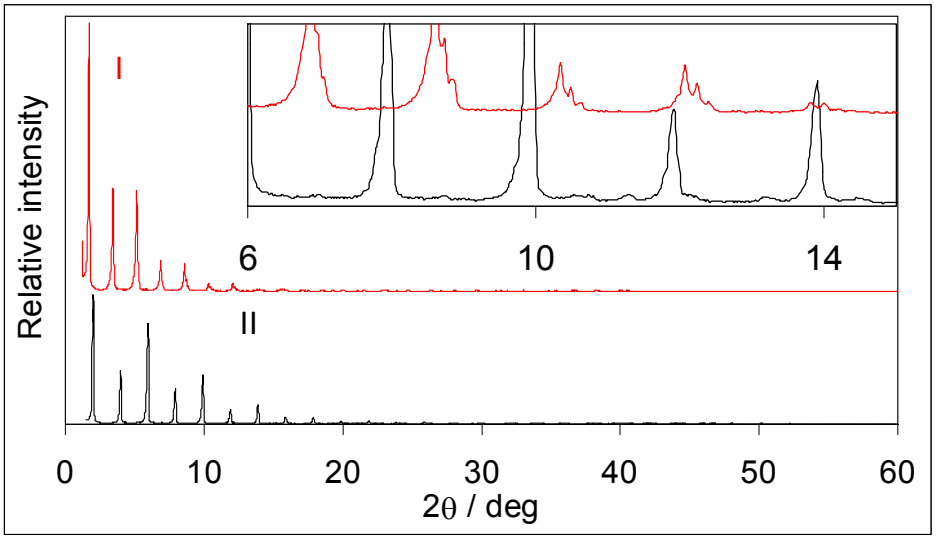

Figure 36. XRD patterns of $Bi(ODT)_3$, prepared from $BiCl_3$ and ODT in ethanol (I) and from Bi_2O_3 and ODT in hexanol (II). Inset: magnification from low-angle region.

Thermal properties of $Bi(ODT)_3$ were investigated by using differential scanning calorimetry (DSC). Fig. 36 shows the two first cycles of $Bi(ODT)_3$ heating curves. In the first heating scan, a sharp endothermic peak is found at 83°C (peak onset temperature). In the second heating scan there is a peak at 62°C. The cooling curves have peaks at 49 and 51 ^{0}C, respectively. Therefore, the peak observed from the first heating scan originated from an irreversible endothermic transition while for the second and following scans a reversible peak was observed. Thus, it can be concluded that $Bi(ODT)_3$ decomposed irreversibly to bismuth and di-n-octadecylsulfide while melted at 83°C. The

latter has melting point 60°C [95]. Large differences between melting and solidifying temperatures are common for large organic compounds.

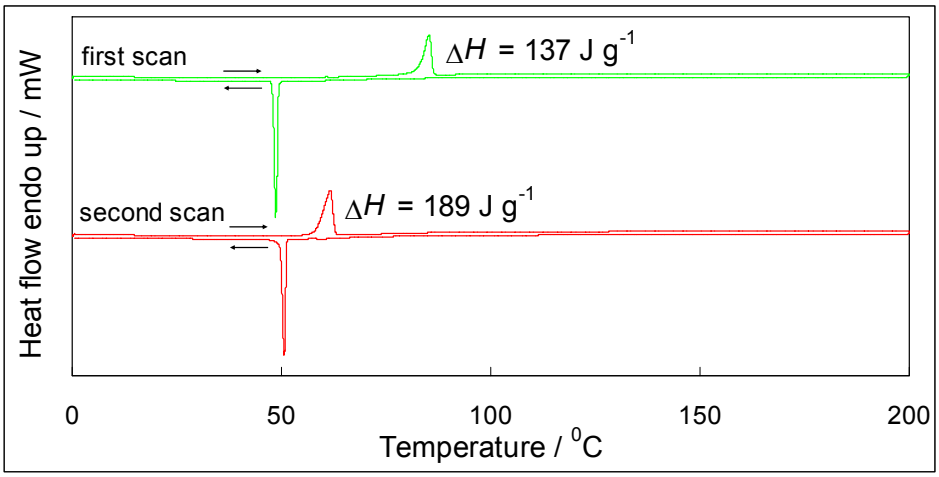

Figure 37. DSC curves of $Bi(ODT)_3$ on heating and cooling scans at 10 deg min^{-1}.

6.3.3. Bismuth thiol interaction mechanism

In metal electrochemical series, bismuth is situated at the left side of hydrogen (E^0 = 0.308 V [122]). Therefore, Bi should not react with acids. Still, the reaction takes place in the presence of oxygen or if acid is itself oxidizer, like nitric acid. The surprising result that, instead of monolayer, a thick thiolate layer formation on Bi in thiol solution contradicts the results from Adamkovski et al. [132], based only on electrochemical data. The bismuth thiolate compounds formed on Bi(001) and Bi(111) electrode surfaces have the melting points quite close to the compounds synthesised in the solution phase. The conclusion is that thiol does not react with bismuth directly, but reacts with bismuth oxide formed on bismuth surface in thiol solution in ethanol at OCP.

Electrochemical and infrared studies of bismuth electrode in thiol ethanol solution indicate that the S-down oriented monolayer cannot be prepared onto bismuth even under electrochemical control because there is too low gap between the thiol reduction and bismuth oxidation potentials (and oxide reacts with thiol) [5].

6.4. Experiments with BiCCE

The potential of BiCCE was fixed at –1.2 V, and some cylinders from a top of the BiCCE were broken until a good flat surface was achieved [1]. The shapes of C_s,E- as well as i,E-curves for 50 μm BiCCE are similar, but the original values of capacitance are three orders of magnitude smaller than that for 4 mm Bi(001) or Bi(111) electrodes [1]. The capacitance values were used for calculation of surface area, and surface roughnesses from 1.1 to 1.8 were achieved due to the non-ideal cleavage: there were some (001) steps on the mainly (111) surface [1] and some bending of capillary electrode during cleavage process probably caused the separation of Bi electrode from the glass capillary walls causing isolation leakage. In this work, BiCCE was used in a variety of electrochemical experiments that were not possible with conventional size Bi macroelectrodes.

6.4.1. Determination of bismuth electrode surface orientation using characteristic pyridine adsorption-desorption peaks

The small area of a single Bi microelectrode makes these measurements impossible with usual XRD equipment. Also, electrochemical determination includes steps on the surface and electrode sides, exposed to solution. Lust et al. [14,15] have found that pyridine forms sharp adsorption-desorption peaks in C,E-curves for the Bi(hkl) electrodes. The peak corresponding to the Bi(111) interface is situated at 100 mV more negative potential than the peak for Bi(001) plane [14–15]. For BiCCE, two well separated peaks have been detected (Fig. 39), the highest peak corresponds to the Bi(111) plane and the minor peak to the surface area with adsorption properties similar to the Bi(001) plane. Higher peak for (111) plane has been obtained for BiCCE in Fig. 38a, whereas BiCCE in Fig. 38b gives higher (001) peak. Thus, the BiCCE electrode surface consists mainly of Bi(111) terraces and less than 15% of Bi(001) plane areas also, corresponding to the steps on the surface or the sides of the electrode.

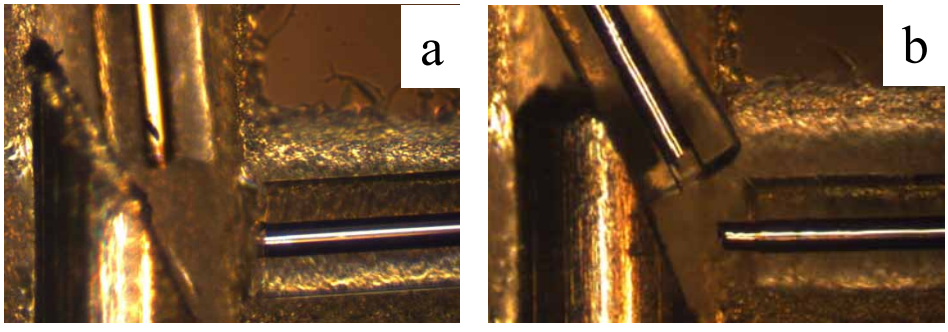

Figure 38. OM images (1.2 x 0.75 mm) of two BiCCEs during cleaving process.

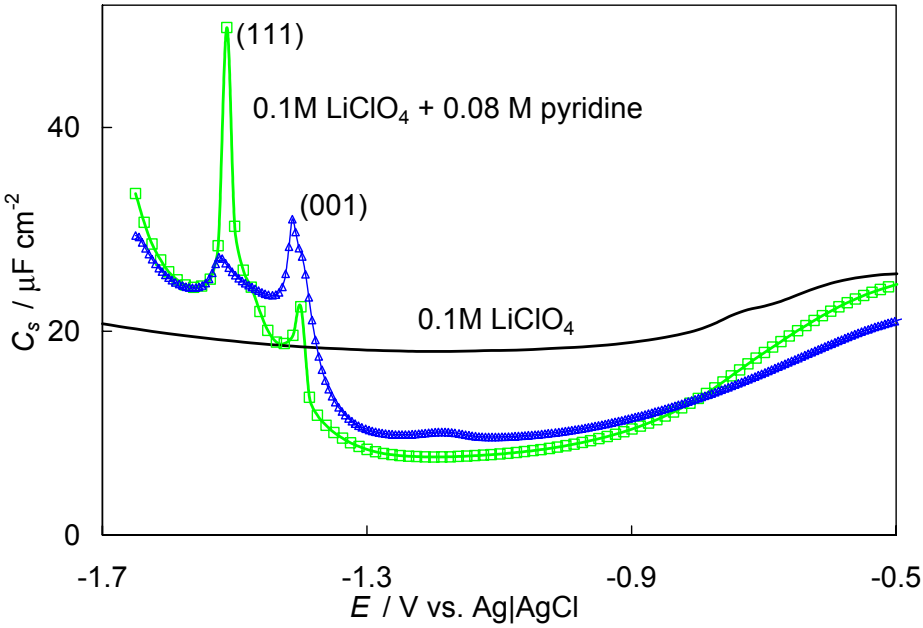

Figure 39. Differential capacitance (at ac frequency f = 210 Hz) dependence on potential in 0.1 M $LiClO_4$ aqueous solution with addition of 0.08 M pyridine for two differently cleaved polycrystal bismuth microelectrodes, shown in Fig. 38.

6.4.2. Electrochemical analysis of heavy metal ions

The ability of BiCCE to detect trace levels of toxic trace metal cations is illustrated in Fig. 40. There is a nearly linear dependence of peak current versus Cd^{2+} and Pb^{2+} concentrations in solution (inset in Fig. 40). The detection limit achieved for a nearly standing solution using 50 μm BiCCE in this experiment was estimated to be ca 0.2 μg L^{-1} for both Cd^{2+} and Pb^{2+} ions [1]. The measurements were carried out on the same cleaved surface in the presence of dissolved oxygen however before each measurement the electrode was electrochemically polished at –0.15 V for 1 second in solution flow.

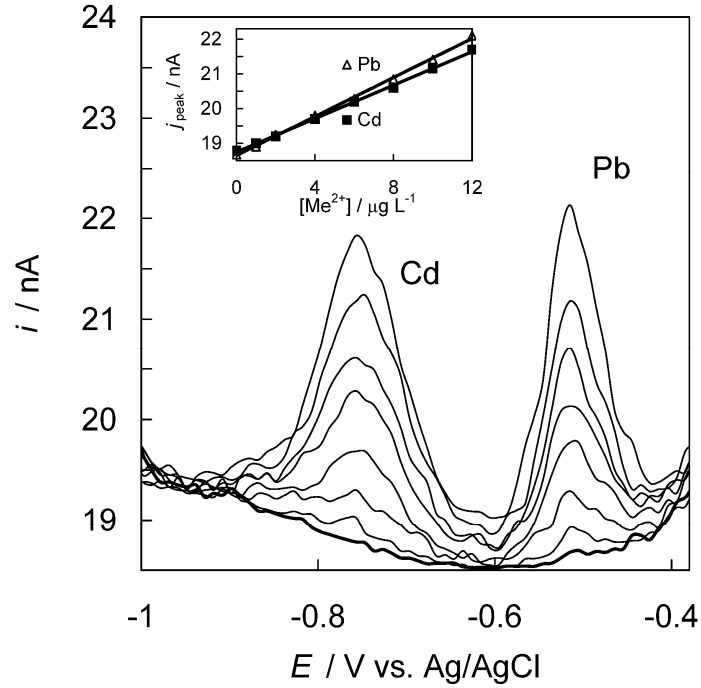

Figure 40. Anodic stripping square-wave voltammograms for increasing concentration levels of Pb^{2+} and Cd^{2+} (from 1 to 12 μg L^{-1}) in solution along with background response. Conditions: 0.1 M acetate buffer (pH = 4.5); preconcentration potential –1.2 V and time 4 min, frequency 200 Hz, potential step 10 mV and amplitude 25 mV. Inset: corresponding calibration plot j_{peak} vs. Pb^{2+} and Cd^{2+} concentrations.

Taking into account that the curves in Fig. 40 have been measured with nearly standing solution, enhancement of detection limit using jet flow method is possible.

6.4.3. Flow injection analysis

Taking into account the good stability of differential capacitance for solid bismuth electrode [1,14–17], the concentration of ions or neutral organic compounds can be determined at maximum adsorption potential. To demonstrate this, 1μL of 0.1 M potassium iodide was injected into the electrolyte flow. The positive-going peak was observed at E = –0.4 V (Fig. 41) because specific adsorption of the iodide ions causes the increase in capacitance [15,135,136]. The injection of organic compound n-hexanol, that neither oxidizes nor reduces on the bismuth surface at –0.7 V, gives the negative-going peak, because n-hexanol has smaller dielectric constant value compared to water, and decreasing the differential capacitance in the region of maximal adsorption. Of course,

larger organic molecules may adsorb irreversibly at maximum adsorption potential and for those compounds stripping analysis is possible.

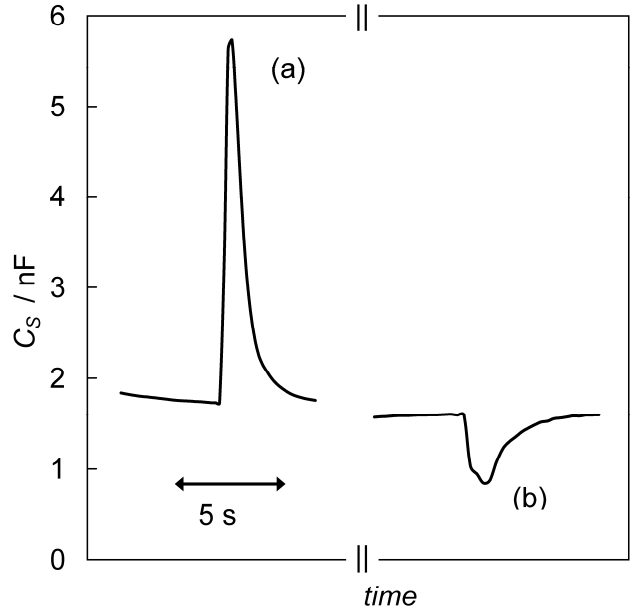

Figure 41. Differential capacitance vs. time plots for injection of 1μL of 0.1 M KI + 0.1 M $LiClO_4$ at E = –0.4 V vs. Ag|AgCl (a) and 1μL of 0.01 M n-hexanol + 0.1 M $LiClO_4$ at E = –0.7 V (b) to a 0.1 M $LiClO_4$ aqueous solution (flow moving at a speed of 1 mL h^{-1}).

6.4.4. Electrochemical studies at the moment of double layer formation

The worked out method of fast cleaving of BiCCE opens new possibilities for studying double layer properties at the moment of its formation. The potential of zero charge (pzc) gives information about the double layer structure of an electrode as well as charge and orientation properties of different adsorbed particles [54,137,138]. Several methods have been worked out to determine pzc, including measuring of the diffuse layer minimum in C,E-curve in dilute electrolyte solutions [54]. There is one more new method for obtaining pzc for dropping mercury electrode using several drop data to find the potential at which the growing of the mercury surface will not induce a change of the charge in time [138] or electrode scrap method [139–144].

The method, proposed here, offers a fast and a very simple way to determine pzc of the Bi(111) plane using BiCCE. The idea is to monitor the current vs. time at fixed electrode potential at the moment of the electrode cleavage. The electrode cleavage in 0.1 M $LiClO_4$ solution (Fig. 42) shows negative-going

peaks at –0.8 and –0.7 V, but at –0.6 V there is a positive-going peak. Integrating one such current peak area gives the charge needed to form the double layer at applied potential. Now, surface charges corresponding to other electrode potentials can be easily obtained from chronocoulonometry measurements and by the linear extrapolation we get pzc = –0.65 V. Based on previous data [54], in 1 mM $LiClO_4$ solution the minimum in *C*,*E*-curve for Bi(111) plane is situated at –0.655 V, indicating that our method developed gives correct pzc values for BiCCE.

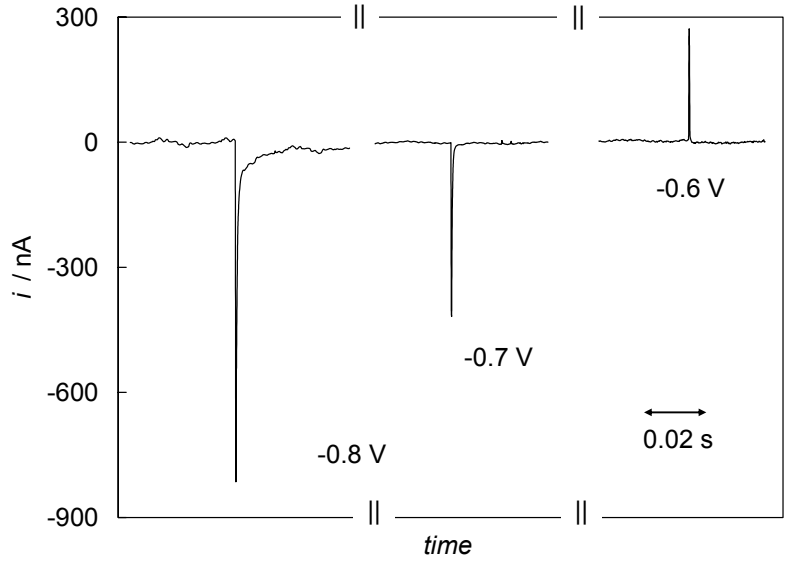

Figure 42. Charging current (*i*) vs. time curves for BiCCE in 0.1 M $LiClO_4$ solution at cleaving potentials –0.8, –0.7 V and –0.6 V vs. Ag|AgCl, measured during three separate experiments. Timescale is given in figure.

7. SUMMARY

This work gave new information about electrochemical properties of bismuth as well as some new preparation methods for Bi electrodes and new compounds. The studies were mainly carried out using cyclic voltammetry, impedance spectroscopy, infrared spectroscopy, and surface imaging techniques (optical microscopy, scanning electron microscopy, atomic force microscopy).

A new method for preparation of nearly single crystalline bismuth micro-electrode with the renewable surface and the corresponding measurement system has been worked out, being a promising replacement for the toxic dropping mercury electrode. The bismuth cleaved capillary electrode (BiCCE) surface is renewed in situ in solution by breaking 320 μm long cylinders on a top of a bismuth filled glass capillary. BiCCE was shown to be suitable for the analysis of trace metal cations or organic compounds and enables to study the double layer formation properties at the moment of the electrode cleavage.

It was shown that thin bismuth films or Bi nanoparticles can be deposited onto silicon wafer using bismuth(III)oxide and hydrofluoric acid as reagents. The formed films have yellowish tinge and are quite rough, consisting of up to 700 nm diameter Bi crystals preferentially (but not exclusively) oriented in (111) plane of rhombohedral symmetry, and are coated with approximately 2 nm thick α–Bi_2O_3 layer, after contact with air atmosphere.

Two different strategies were used for in situ deposition of porous bismuth onto Bi microelectrode in aqueous 0.1 M $LiClO_4$ solution. Porous surface was prepared by anodic dissolution of bismuth electrode followed by fast electroreduction of formed Bi^{3+} ions at cathodic potentials. The nanostructured porous bismuth electrode, with surface roughness factor up to 220, consists of Bi nanowires and has higher hydrogen evolution overvoltage than observed for smooth Bi electrodes. It was established that gaseous bismuth hydride formation and decomposition into Bi nanoparticles takes place at high negative electrode potentials ($E < -2$ V vs. Ag|AgCl).

It was found that the impedance of pure Bi electrode have negligible frequency dependence of capacitance but noticeable frequency dependence of charge transfer resistance. In situ infrared spectroscopy measurements conclude that the Bi surface in aqueous and ethanol solutions does not have any chemisorbed species and the change in electrode potential causes the reorientation of solvent molecules as well as the change in ion concentration near the Bi electrode surface.

Analysis of results demonstrates that after holding of Bi electrodes during some hours in solution of thiol in ethanol, bismuth is covered with a thick porous layer of bismuth thiolate compound but not a self-assembled thiol monolayer like observed on Au electrodes. For the verification of formed thiolate layers the new compounds tris(1-octadecylthio)bismuthine and tris(1-decylthio)bismuthine were also synthesised from bismuth(III)oxide and thiol in

hexane solution and a similarity of properties with the bismuth thiolate compounds, formed at the bismuth electrode surface, has been demonstrated.

Some new applications of Bi electrodes can be suggested:

- Electroanalysis of heavy metals or organic compounds with bismuth cleaved capillary microelectrode system.
- Electroless deposition of thin bismuth films on silicon and preparation of porous bismuth for electronics industry.
- Bismuth surface modification with thiols for lithography, corrosion protection or in electroanalysis for analyte collection step. New method for synthesis of bismuth thiolates from metal oxide.

8. REFERENCES

[1] T. Romann, S. Kallip, V. Sammelselg, E. Lust, Bismuth microelectrode system with in situ renewable surface for electroanalysis and adsorption studies, Electrochem. Comm. 10 (2008) 1008.

[2] T. Romann, E. Lust, Electrochemical properties of porous bismuth electrodes, Electrochimica Acta, doi:10.1016/j.electacta.2010.05.012.

[3] T. Romann, H. Mändar, K. Tõnurist, E. Lust, Modification of heavy metal surfaces with thiols, FMTDK converence, Tartu, Estonia, February 25–26, 2010.

[4] T. Romann, E. Anderson, S. Kallip, H. Mändar, L. Matisen, E. Lust, Electroless deposition of bismuth on Si(111) wafer from hydrogen fluoride solutions, Thin Solid Films 518 (2010) 3690.

[5] T. Romann, E. Lust, Formation of the Bismuth Thiolate Compound Layer on Bismuth Surface, In: 5th Baltic Converence on Electrochemistry: Functional Materials in Electrochemistry – from Fundamental problems to Molecular Electronics and Modern Power Sources; Tartu, Estonia, 30 April – 3 May 2008, P–30.

[6] T. Romann, M. Väärtnõu, A. Jänes, E. Lust, In situ infrared spectroscopic characterization of a bismuth-ethanol interface, Electrochim. Acta 53 (2008) 8166.

[7] T. Romann, M. Väärtnõu, E. Lust, In Situ Infrared Spectroscopic Studies of Water and Ethanol on Bismuth Single Crystal Surfaces, In: Cd of Abstracts: The 59th Annual Meeting of the International Society of Electrochemistry, Sevilla, Spain, September 6–13, 2008, Abs. s02-P-059**.**

[8] T. Romann, V. Grozovski, E. Lust, Formation of the bismuth thiolate compound layer on bismuth surface, Electrochem. Comm. 9 (2007) 2507.

[9] T. Romann, K. Lust, E. Lust, Adsorption of 1,6-hexanediol on Bi single crystal electrodes, Electrochim. Acta 52 (2007) 2612.

[10] T. Romann, Cyclic Voltammetry Studies of Organic Compound Adsorption on Bismuth Electrodes, Master's thesis, Institute of Physical Chemistry, University of Tartu, 2006.

[11] T. Romann, Vesiniku katoodse eraldumise protsessi kineetika vismuti monokristalli tahkudel (Hydrogen evolution reaction kinetics on bismuth single crystal electrodes), Bachelor's thesis, Institute of Physical Chemistry, University of Tartu, 2005.

[12] A. Economou, Trends in Anal. Chem. 24 (2005) 334.

[13] E.J. Lust, U. V. Palm, Soviet Electrochem. Engl. Tr. 21 (1985) 1304.

[14] E. Lust, A. Jänes, P. Miidla, K. Lust, J. Electroanal. Chem. 425 (1997) 25.

[15] E. Lust, A. Jänes, K. Lust, V. Sammelselg, P. Miidla, Electrochim. Acta 42 (1997) 2861.

[16] S. Kallip, E. Lust, Electrochem. Comm. 7 (2005) 863.

[17] S. Kallip, H. Kasuk, V. Grozovski, P. Möller, E. Lust, Electrochim. Acta 53 (2008) 4035.

[18] J. Wang, J.M. Lu, S.B. Hoćevar, P.A.M. Farias, B. Ogorevc, Anal. Chem. 72 (2000) 3218.

[19] E. A. Hutton, S.B. Hoćevar, L. Mauko, B. Ogorevc, Anal. Chim. Acta. 580 (2006) 244.

[20] L. Lin, S. Thongngamdee, J. Wang, Y. Lin, O.A. Sadik, S.-Y. Ly, Anal. Chim. Acta 535 (2005) 9.
[21] E. A. Hutton, B. Ogorevc, S.B. Hoćevar, F. Weldon, M.R. Smyth, J. Wang, Electrochem. Comm. 3 (2001) 707.
[22] M. Bučková, P. Gründler, G.-U. Flechsig, Electroanalysis 17 (2004) 440.
[23] Ph. Hofmann, Progr. Surf. Sci. 81 (2006) 191.
[24] E.I. Rogacheva, S.G. Lyubchenko, M.S. Dresselhaus, Thin Solid Films 516 (2008) 3411.
[25] K.S. Wu, M.Y. Chern, Thin Solid Films 516 (2008) 3808.
[26] K.S. Wu, M.Y. Chern, J. Appl. Phys. 104 (2008) 033704/1.
[27] X. Duan, J. Yang, W. Zhu, X. Fan, C. Xiao, Mater. Lett. 61 (2007) 4341.
[28] F.Y. Yang, K. Liu, K. Hong, D.H. Reich, P.C. Searson, C.L. Chien, Science 248 (1999) 1335.
[29] K.J. Wan, T. Guo, W.K. Ford, J.C. Hermanson, Phys. Rev. B 44 (1991) 3471.
[30] T. Nagao, J.T. Sadowski, M. Saito, S. Yaginuma, Y. Fujikawa, T. Kogure, T. Ohno, Y. Hasegawa, S. Hasegawa, T. Sakurai, Phys. Rev. Lett. 93 (2004) 105501–1.
[31] S. Yaginuma, T. Nagao, J.T. Sadowski, M. Saito, K. Nagaoka, Y. Fujikawa, T. Sakurai, T. Nakayama, Surf. Sci. 601 (2007) 3593.
[32] L. Kumari, J.-H. Lin, Y.-R. Ma, J. Phys. D: Appl. Phys. 41 (2008) 025405/1.
[33] D. Fan, F.Q. Zhu, I.X. Shao, P.C. Searson, R.C. Cammarata, Mat. Res. Soc. Symp. Proc. 781E (2003) Z4.2.1.
[34] M.J. Esplandiu, M.L. Carot, F.P. Cometto, V.A. Macagno, E.M. Patrito, Surf. Sci. 600 (2006) 155.
[35] U. Akiba, M. Fujihira, in: A.J. Bard, M. Stratmann (Eds.), Encyclopedia of Electrochemistry, vol. 10, Wiley, Darmstadt, 2007, Ch. 1.2.1.
[36] R.H. Terrill, T.A. Tanzer, P.W. Bohn, Langmuir 14 (1998) 845.
[37] M.A. Hines, J.A. Todd, P. Guyot-Sionnest, Langmuir 11 (1995) 493.
[38] M.M. Walczak, C. Chung, S.M. Stole, C.A. Widrig, M.D. Porter, J. Am. Chem. Soc. 113 (1991) 2370.
[39] B. Speiseri, in: A. J. Bard, M. Stratmann (Eds.), Encyclopedia of Electrochemistry, vol 3, Wiley, New York, 2003, 81–104.
[40] A. M. Bond, Broadening Electrochemical Horizons, Oxford University Press, Great Britain, 2002.
[41] A. J. Bard, L. R. Faulkner, Electrochemical Methods: Fundamentals and Applications, 1st ed., John Wiley & Sons, New York, 1980.
[42] H. Strieger, D. Krznaic, D.M. Kolb, J. Electroanal. Chem. 532 (2002) 227–235.
[43] S. Hason, S.-P. Simonaho, R. Silvennoinen, V. Vetterl, Electrochim. Acta 48 (2003) 651–668.
[44] S. Hason, V. Vetterl, J. Electroanal. Chem. 536 (2002) 19.
[45] A. J. Bard, L. R. Faulkner, Electrochemical Methods: Fundamentals and Applications, 1st ed., John Wiley & Sons, New York, 1980.
[46] S. Krause, in: A. J. Bard, M. Stratmann (Eds.), Encyclopedia of Electrochemistry, vol. 3, Wiley, New York, 2003, 196–229.
[47] ZVIEW for Windows (version 2.3), Scribner Inc.
[48] D.C. Grahame, Chem. Rev., 41, 441 (1947).
[49] R. Parsons, Chapter 4 in Modern Aspects of Electrochemistry, J. O'M Bocris and B. E. Conway, eds., vol. 1, Chapter 4, Butterworths, London (1954).
[50] J.-P. Badlali, J. Goodisman, J. Phys. Chem. 79 (1975) 223.

19

[51] A. Lasia in: B.E. Conway (Ed.), Modern Aspects of Electrochemistry, no. 32 (2002) p.143.
[52] J. O. Agak, R. Stoodley, U. Retter, D. Bizzotto, J. Electroanal. Chem. 562 (2004) 135.
[53] Z. Kerner, T. Pajkossy, Electrochim. Acta 47 (2002) 2055.
[54] E. Lust in: A.J. Bard, M. Stratmann (Eds.), Encyclopedia of Electrochemistry, vol. 1, Wiley, Weinheim, 2002, Ch. 2.
[55] A. Lasia in: B.E. Conway (Ed.), Modern Aspects of Electrochemistry, no. 32 (2002) p.143.
[56] N.A. Hampson, C. Lazarides, A.C. Tyrrell, R. Leek, J.P.G. Farr, Surf. Technol. 15 (1982) 167.
[57] R. Jurczakowski, C. Hitz, A. Lasia, J. Electroanal. Chem. 572 (2004) 355.
[58] A. Jänes, E. Lust, J. Electroanal. Chem. 588 (2006) 285.
[59] S.A. Cotgreave, N.A. Hampson, P.C. Morgan, M. Welsh, R. Leek, Surf. Technol. 13 (1981) 107.
[60] T. Pajkossy, Solid State Ionics 176 (2005) 1997.
[61] Z. Kerner, T. Pajkossy, J. Electroanal. Chem. 448 (1998) 139.
[62] Z. Kerner, T. Pajkossy, Electrochim. Acta 46 (2000) 207.
[63] T. Pajkossy, J. Electroanal. Chem. 364 (1994) 111.
[64] R.S. Neves, E. De Robertis, A.J. Motheo, Electrochim. Acta 51 (2006) 1215.
[65] T. Pajkossy, T. Wandlowski, D.M. Kolb, J. Electroanal. Chem. 414 (1996) 209.
[66] G. Nurk, A. Jänes, K. Lust, E. Lust, J. Electroanal. Chem. 515 (2001) 17–32.
[67] P. Zoltowski, J. Electroanal. Chem. 457 (1998) 149.
[68] A. Sadkowski, J. Electroanal .Chem. 481 (2000) 222.
[69] B.B. Damaskin, O.A. Petrii, V.V. Batrakov, Adsorption of Organic Compounds on Electrodes, Plenum, New York (1971) p. 35.
[70] D. R. Lide, CRC Handbook of Chemistry and Physics. 84th edition, (2003–2004), 595–596.
[71] K. Lust, E. Perkson, E. Lust, Russian J. of Electrochem. 36 (1999) 1257.
[72] T. Zhang, C. Chen, Y. Shao, G. Meng, F. Wang, X. Li, C. Dong, Electrochim. Acta 53 (2008) 7921.
[73] F.-H. Cao, Z. Zhang, J.-X.Su, J.-Q. Zhang, Materials and Corrosion. 56 (2005) 318.
[74] C. Cachet, R. Wiart, I. Ivanov, Y. Stefanov, R. Rashkov, J. Appl. Electrochem. 24 (1994) 713.
[75] P. Córdoba-Torres, M. Keddam, R.P. Nogueira, Electrochim. Acta 54 (2008) 518.
[76] P. Córdoba-Torres, M. Keddam, R.P. Nogueira, Electrochim. Acta 54 (2009) 6779.
[77] X. Chen, S. Chen, W. Huang, J. Zheng, Z. Li, Electrochim. Acta 54 (2009) 7370.
[78] X. Wang, P.F. Souter, L. Andrews, J. Phys. Chem. A 107 (2003) 4244.
[79] W. Jerzembeck, H. Bürger, L. Constantin, L. Margulès, J. Demaison, J. Breidung, W. Thiel, Angew. Chem. Int. Ed. 41 (2002) 2550.
[80] S.Y. Chen, Z.F. Zhang, H.M. Yu, Anal. Bioanal. Chem. 374 (2002) 126.
[81] A. D'Ulivo, Z. Mester, R.E. Sturgeon, Spectrochim. Acta Part B 60 (2005) 423.
[82] R.J. Forster, in: A.J. Bard, M. Stratmann (Ed.), Encyclopedia of Electrochemistry, vol. 3, Wiley, New York, 2003, Ch. 2.5.
[83] L. Murtomäki, K. Kontturi, J. Electroanal. Chem. 449 (1998) 225.

[84] N. Li, V. Zamlynny, J. Lipkowski, F. Henglein, B. Pettinger, J. Electroanal. Chem. 524–525 (2002) 43.
[85] B. Pettinger, J. Lipkowski, M. Hoon-Khosla, J. Electroanal. Chem. 500 (2001) 471.
[86] Y. Ikezawa, T. Sawatari, T.K.H. Goto, K. Toriba, Electrochim. Acta 43 (1998) 3297.
[87] Y. Ikezawa, T. Sawatari, H. Terashima, Electrochim. Acta 46 (2001) 1333.
[88] M. Hoon-Khosla, W.R. Fawcett, A. Chen, J. Lipkowski, B. Pettinger, Electrochim. Acta 45 (1999) 611.
[89] M. Ito, Surf. Sci. Reports, 63 (2008) 329.
[90] Th. Wandlowski, K. Ataka, S. Pronkin, D. Diesing, Electrochim. Acta 49 (2004) 1233.
[91] M. Osawa, M. Tsushima, H. Mogami, G. Samjeské, A. Yamakata, J. Phys. Chem. C 112 (2008) 4248.
[92] M. Futamata, L. Luo, C. Nishihara, Surf. Sci. 590 (2005) 196.
[93] M. Osawa, M. Tsushima, H. Mogami, G. Samjeské, Structure of water at the Pt/acid interface: An infrared study, In: Cd of Abstracts: The 59th Annual Meeting of the International Society of Electrochemistry, Sevilla, Spain, September 6–13, 2008**.**
[94] A. N. Parikh, S. D. Gillmor, J. D. Beers, K. M. Beardmore, R. W. Cutts, B. I. Swanson, J. Phys. Chem. B 1999, 103, 2850.
[95] S.-Ho. Cha, K.-H. Kim, J.-U. Kim, W.-K. Lee, J.-C. Lee, J. Phys. Chem. C 112 (2008) 13682.
[96] P.A. Christensen, in: A. J. Bard, M. Stratmann (Eds.), Encyclopedia of Electrochemistry, vol. 3, Wiley, New York, 2003, 530–571.
[97] S. Pons, J. Electroanal. Chem. 150 (1983) 495.
[98] C. Korzeniewski, S. Pons, J. Vac. Sci. Technol. B 3 (1985) 1421.
[99] C.Korzeniewski, B. S. Pons, Langmuir 2 (1986) 468.
[100] C. Korzeniewski, R. B. Shirts, B. S. Pons, J. Phys. Chem. 89 (1985) 2297.
[101] P.W. Faguy, N.S. Marinković, Anal. Chem. 67 (1995) 2791.
[102] M. Osawa, K. Yoshii, K. Ataka, T. Yotsuyanagi, Langmuir 10 (1994) 640.
[103] A. Hartstein, J. R. Kirtly, J. C. Tsang, Phys. Rev. Lett. 45 (1980) 201.
[104] T. Iwasita, F.C. Nart, Prog. Surf. Sci. 55 (1997) 271.
[105] M.H. Shao, R.R. Adzic, Electrochim. Acta 50 (2005) 2415.
[106] V. Pacheco Santos, V. Del Colle, R.B. de Lima, G. Tremiliosi-Filho, Electrochim. Acta 52 (2007) 2376.
[107] M. Futamata, Surf. Sci. 427–428 (1999) 179.
[108] N.S. Marinković, J.S. Marincović, R.R. Adžic, J. Electroanal. Chem. 467 (1999) 291.
[109] Y. Ikezawa, T. Ariga, Electrochim. Acta 52 (2007) 2710.
[110] K. Arihara, F. Kitamura, T. Ohsaka, K. Tokuda, J. Electroanal. Chem. 518 (2002) 139.
[111] M.-W. Yang, S.-Y. Lin, Colloids Surf. 220 (2003) 199.
[112] E.J. Lust, U. V. Palm, Soviet Electrochem. Engl. Tr. 21 (1985) 1304.
[113] E. Lust, A. Jänes, P. Miidla, K. Lust, J. Electroanal. Chem. 425 (1997) 25.
[114] E. Lust, K. Lust, A. Jänes, Russ. J. Electrochem. 31 (1995) 876.
[115] S. Kallip, E. Lust, Electrochem. Comm. 7 (2005) 863.
[116] E. F. Cave, L. V. Holroyd, J. Appl. Phys. 31 (1960) 1357.
[117] J. Emsley, The Elements, 3rd ed., Clarendon press, Oxford, 1988, p. 36.

[118] S. Trasatti, E. Lust, Mod. Aspects Electrochem. 33 (1999).
[119] J. Emsley, The Elements, third ed., Clarendon Press, Oxford, 1988.
[120] R.M. Tiggelaar, F. Benito-López, D.C. Hermes, H. Rathgen, R.J.M. Egberink, F.G. Mugele, D.N. Reinhoudt, A. van den Berg, W. Verboom, H.J.G.E. Gardeniers, Chem. Eng. 131 (2007) 163.
[121] M.G. Roper, J.G. Shackman, G.M. Dahlgren, R.T. Kennedy, Anal. Chem. 75 (2003) 4711.
[122] D .R. Lide (Ed.), CRC Handbook of Chemistry and Physics, Internet Version 2005.
[123] Powder Diffraction File, Joint Committee on Powder Diffraction Standards, ASTM, Philadelphia, PA, 2009, Card 4401246.
[124] L. Kumari, J.-H. Lin, Y.-R. Ma, J. Phys. D: Appl. Phys. 41 (2008) 025405/1.
[125] L. Kumari, J.-H. Lin, Y.-R. Ma, J. Phys. Condens. Matter 19 (2007) 406204/1.
[126] Справочник химика III, Moskva, 1964, 769–771.
[127] E.J. Lust, U.V. Palm. Sov. Electrochem. Engl. Tr. **24** (1988),227.
[128] G. Nurk, A. Jänes, P. Miidla, K. Lust, E. Lust, J. Electroanal. Chem. 515 (2001) 33.
[129] E. Lust, A. Jänes, K. Lust, J. Electroanal. Chem. 436 (1997) 141.
[130] E. Lust, A. Jänes, K. Lust, P. Miidla, J. Electroanal. Chem. 442 (1998) 189.
[131] M. Goledzinovski, J. Dojlido, J. Lipkowski, J. Electroanal. Chem. 185 (1985) 131.
[132] M. Adamkovski, A.Zajac, P. Gründler, G.-U. Flechsig, Electrochem. Commun. 8 (2006) 932.
[133] Yu.V. Barabash, Yu.G. Skrypnik, I.A. Shevchuk, Z.G. Korotkova, Zhurnal Analiticheskoi Khimii 34 (1979) 1505.
[134] L.J. Farrugia, F.J. Lawlor, N.C. Norman, Polyhedron 14 (1995) 311.
[135] B. Damaskin, U. Palm, E. Petyärv, M. Salve, J. Electroanal. Chem. 47 (1973) 127.
[136] M. Väärtnõu, E. Lust, J. Electroanal. Chem. 614 (2008) 1.
[137] E. Lust, K. Lust, A. Janes, Elektrokhimiya 26 (1990) 1627.
[138] M. Žic, J. Electroanal. Chem. 584 (2005) 215.
[139] D.D. Bode, T.N. Anderson, H. Eyring, J. Phys. Chem. 71 (1967) 792.
[140] T.N. Anderson, J.L. Anderson, H. Eyring, J. Phys. Chem. 73 (1969) 3562.
[141] L.E. Rybalka, D.I. Leikis, A.G. Zelinskii, Elektrokhimiya 12 (1976) 1340.
[142] V.A. Safonov, S.A. Sokolov, V.M. Gelovich, Dokl. Akad. Nauk SSSR 299 (1988) 1438.
[143] V.A. Safonov, L.Yu. Komissarov, O.A. Petrii, Electrochim. Acta 42 (1997) 675.
[144] S. Trasatti, E. Lust, Mod. Aspects Electrochem. 33 (1999).

9. SUMMARY IN ESTONIAN

Vismuti õhukeste kihtide, poorsete ja mikroelektroodide valmistamine ning nende pinna modifitseerimise meetodid

Käesolevas töös konstrueeriti mitmesuguseid vismutil baseeruvaid nano- ja mikromõõtmetes elektroode ning mõõteseadmeid ja töötati välja vismuti pinna modifitseerimise meetodeid. Mõõtmiste käigus saadi ka uut informatsiooni vismuti elektrokeemiliste omaduste kohta. Kasutati peamiselt tsüklilise voltammeetria, elektrokeemilise impedantsi ja uudse in situ infrapuna spektroskoopia meetodeid ning pinna mikroskoopia tehnikaid.

Töötati välja uus meetod vismuti monokristalse mikroelektroodi (BiCCE) valmistamiseks ja konstrueeriti mõõtesüsteem. 50 μm diameetriga BiCCE pinda on võimalik mõõtmiste käigus lihtsasti uuendada, murdes Bi elektroodi otsast 320 μm pikkusi tükke. Näidati, et BiCCE abil saab teostada raskmetalli jääkide analüüsi ja läbi viia uudseid adsorptsiooni ning elektrilise kaksikkihi alaseid uuringuid pinna uuenemise hetkel.

Leiti, et õhukest vismutkihti või nanoosakesi on lihtsasti võimalik räni pinnale sadestada vismutfluoriidi sisaldavast vesilahusest. Tekkinud vismutkiht on kollase läikega, koosnedes kuni 700 nm suurustest (111) orientatsiooniga Bi kristallidest ning on õhus kaetud 2 nm paksuse α-Bi_2O_3 kihiga.

Poorse vismuti valmistamiseks kasutati kahte erinevat strateegiat. Bi pinda oksüdeeriti lahustumiseni ja seejärel redutseeriti kiiresti tagasi metalseks vismutiks. Tekkinud Bi nanovarrastest koosneva poorse struktuuri eripind on 220 ning sel on 140 mV suurem vesiniku eraldumise ülepinge kui siledal Bi elektroodil. Teiseks hoiti Bi elektroodi väga katoodsetel potentsiaalidel (E < – 2 V Ag|AgCl võrdluselektroodi suhtes) ja leiti, et elektroodilt eraldub gaasiline BiH_3, mis laguneb kiiresti Bi nanoosakesteks ja sadeneb tagasi elektroodi pinnale.

Leiti, et Bi elektroodi mahtuvus ei sõltu mõõtesagedusest, kuid laengu-ülekandeprotsessi takistus sõltub. In situ infrapunaspektroskoopia mõõtmiste tulemustest võib järeldada, et Bi|vesilahuse ja Bi|etanooli piirpinnal pole spetsiifiliselt adsorbeerunud ühendeid ja elektroodi potentsiaali muutus kutsub esile ainult pinnalähedaste solvendimolekulide orientatsiooni ning ioonide pinnalähedase konsentratsiooni muutuse.

Selgus, et erinevalt tioolide monokihtidest kullal, tekib vismuti pinnale paksem vismuttiolaadi kiht. Tekkinud kihi tuvastamiseks sünteesiti ka uued ühendid tris(1-oktadetsüültio)vismutiin ja tris(1-detsüültio)vismutiin heksaani lahuses Bi_2O_3 reaktsioonil vastava tiooliga ning tõestati, et just need ühendid tekkisid ka Bi elektroodi pinnal.

Mõningad selle töö rakendusi:

- Raskmetallide ja orgaaniliste ühendite elektroanalüüs BiCCE süsteemiga.
- Õhukeste vismutkihtide sadestamine ränile ja poorse vismuti valmistamine elektroonikatööstuse tarbeks.
- Vismuti pinna modifitseerimine tioolidega litograafiaks, korrosiooni kaitseks või ainete elektroanalüüsil analüüdi kogumise etapis. Uus sünteesimeetod vismut-tiolaatide saamiseks lähtudes metalli oksiidist.

10. ACKNOWLEDGEMENTS

First and foremost I would like to express my greatest gratitude to my supervisor Professor Enn Lust for his great guidance and support trough the electrochemistry studies.

I would like to thank Karmen Lust about help in technical correction of manuscipts and all my friends and colleagues for helpful discussions, inspirations and continuous support.

I also want to thank my grandmother for giving me chemistry books that started my deep interest in chemistry.

I would like to acknowledge the following persons:

- Dr. Gunnar Nurk for the help of setting up infrared spectroscopy experiments.
- Dr. Kristjan Laes, Dr. Heili Kasuk, Dr. Mart Väärtnõu and Dr. Jaak Nerut for introduction of electrochemical measurements with Autolab.
- Kersti Vaarmets, Liis Siinor, Dr. Thomas Thomberg, Dr. Jaanus Kruusmaa, Dr. Indrek Kivi, and Dr. Eneli Härk for finding necessary glassware, chemicals and other equipment when it was most needed.
- Dr. Silvar Kallip, Erik Anderson, Vitali Grozovski, and Margus Marandi for the help with the AFM measurements.
- Dr. Hugo Mändar for the XRD and SAXS measurements.
- Dr. Leonard Matisen for the XPS measurements.
- Dr. Ilmo Sildos, Mihkel Rähn, and Sven Lange for Raman and photo-luminescence measurements.
- Prof. Väino Sammelselg for taking SEM images from Bi micro-electrodes.
- Dr. Tõnu Järveots for assistance with Leo 1430 (SEM) machine.
- Kerli Tõnurist for the DSC measurements.

Financial support from Graduate School on Functional Materials and Technologies, University of Tartu and Tallinn University of Technology,
ESF project 1.2.0401.09-0079.

11. PUBLICATIONS

CURRICULUM VITAE

Tavo Romann

Born:	05.12.1982, Tartu, Estonia
Citizenship:	Estonian
Address:	Institute of Chemistry University of Tartu 14A Ravila St., Tartu 50411, Estonia
E-mail	tavo.romann@ut.ee

Education

2006 – ...	University of Tartu, *Ph.D.* student (physical and electrochemistry).
2005–2006	University of Tartu, *M.Sc.* in physical and electrochemistry, 2005
2001–2005	University of Tartu, *B. Sc.* in chemistry

Professional employment

2008 – ...	University of Tartu, Institute of Chemistry, contractual-researcher (0.5)
2007–2008	University of Tartu, Institute of Physical Chemistry, contractual-researcher (0.5)
2006–2007	University of Tartu, Institute of Physical Chemistry, chemist (0.5)

List of publications

1. T. Romann, E. Lust, Electrochemical properties of porous bismuth electrodes, Electrochimica Acta, doi:10.1016/j.electacta.2010.05.012.
2. A. Jänes, H. Kurig, T. Romann, E. Lust, Novel doubly charged cation based electrolytes for non-aqueous supercapacitors, Electrochem. Comm. 12 (2010) 535.
3. H. Kurig, T. Romann, A. Jänes, E. Lust, Electrochemical characteristics of titanium carbide derived carbon|1-ethyl-3-methylimidazolium tetrafluoroborate electrical double layer capacitors, ECS Trans. 25 (2010) 15.
4. T. Romann, E. Anderson, S. Kallip, H. Mändar, L. Matisen, E. Lust, Electroless deposition of bismuth on Si(111) wafer from hydrogen fluoride solutions, Thin Solid Films 518 (2010) 3690.
5. T. Romann, H. Mändar, K. Tõnurist, E. Lust, Modification of heavy metal surfaces with thiols, FMTDK converence, Tartu, Estonia, February 25–26, 2010.

6. T. Romann, E. Lust, Electrochemical properties of porous bismuth, In: Meeting Abstracts (CD): 216th ECS Meeting, Vienna, Austria, October 4–9, 2009, Abs. 3022.
7. T. Romann, M. Väärtnõu, A. Jänes, E. Lust, In situ infrared spectroscopic characterization of a bismuth-ethanol interface, Electrochim. Acta 53 (2008) 8166.
8. T. Romann, S. Kallip, V. Sammelselg, E. Lust, Bismuth microelectrode system with in situ renewable surface for electroanalysis and adsorption studies, Electrochem. Comm. 10 (2008) 1008.
9. T. Romann, M. Väärtnõu, E. Lust, In Situ Infrared Spectroscopic Studies of Water and Ethanol on Bismuth Single Crystal Surfaces, In: Cd of Abstracts: The 59th Annual Meeting of the International Society of Electrochemistry, Sevilla, Spain, September 6–13, 2008, Abs. s02-P-059**.**
10. T. Romann, E. Lust, Formation of the Bismuth Thiolate Compound Layer on Bismuth Surface, In: 5th Baltic Converence on Electrochemistry: Functional Materials in Electrochemistry – from Fundamental problems to Molecular Electronics and Modern Power Sources; Tartu, Estonia, 30 April – 3 May 2008, P-30.
11. Nerut, J.; Thomberg, T.; Härk, E.; Lust, K.; Jäger, R.; Kallip, S.; Kasuk, H.; Grozovski, V.; Romann, T.; Väärtnõu, M.; Lust, E. (2008). Adsorption kinetics and electroreduction of compex ions on the Bi(hkl) and Cd(0001) single crystal planes. In: 5th Baltic Conference on Electrochemistry: Functional Materials in Electrochemistry – from Fundamental problems to Molecular Electronics and Modern Power Sources; Tartu, Estonia; 30 April – 3 May, 2008, O-6.
12. T. Romann, E. Lust, Renewable Surface Microelectrode System for Research and Electroanalysis, In: Book of Abstracts: 6th Spring Meeting of the International Society of Electrochemistry, Foz do Iguacu, Brazil, 16–19 March, 2008, 74.
13. T. Romann, V. Grozovski, E. Lust, Formation of the bismuth thiolate compound layer on bismuth surface, Electrochem. Comm. 9 (2007) 2507.
14. T. Romann, M. Väärtnõu, E. Lust, In situ infrared spectroscopy characterization of bismuth-ethanol interface, In: Abstracts of Scientific Converence: 30th Estonian Chemistry Days; Tartu, Estonia; 16 November, 2007, 137.
15. Lust, E.; Grozovski, V.; Härk, E.; Jäger, R.; Kallip, S.; Kasuk, H.; Lust, K.; Nerut, J.; Romann, T.; Thomberg, T.; Väärtnõu, Kinetics of ionic and molecular adsorption and electroreduction mechanism of complex ions in relation to the surface structure of the Bi, Sb and Cd electrodes. 58th Annual Meeting of the International Society of Electrochemistry, Banff, Canada, September 9 to 14, 2007.
16. T. Romann, K. Lust, E. Lust, Adsorption of 1,6-hexanediol on Bi single crystal electrodes, Electrochim. Acta 52 (2007) 2612.

ELULOOKIRJELDUS

Tavo Romann

Sünniaeg ja koht:	05.12.1982, Tartu, Eesti Vabariik
Kodakondsus:	Eesti
Aadress:	Keemia Instituut Tartu Ülikool Ravila 14A, Tartu 50411, Eesti
E-post:	tavo.romann@ut.ee

Haridus

2006 – ...	Tartu Ülikool, *Ph.D*. (füüsikalise ja elektrokeemia erialal).
2005–2006	Tartu Ülikool, *M.Sc*. (füüsikalise ja elektrokeemia erialal).
2001–2005	Tartu Ülikool, *B. Sc*. (keemia erialal).

Teenistuskäik

2008 – ...	Tartu Ülikool, Keemia instituut, erakorraline teadur (0.5)
2007–2008	Tartu Ülikool, Füüsikalise keemia instituut, erakorraline teadur (0.5)
2006–2007	Tartu Ülikool, Füüsikalise keemia instituut, keemik (0.5)

Ilmunud teaduspublikatsioonid

1. T. Romann, E. Lust, Electrochemical properties of porous bismuth electrodes, Electrochimica Acta, doi:10.1016/j.electacta.2010.05.012.
2. A. Jänes, H. Kurig, T. Romann, E. Lust, Novel doubly charged cation based electrolytes for non-aqueous supercapacitors, Electrochem. Comm. 12 (2010) 535.
3. H. Kurig, T. Romann, A. Jänes, E. Lust, Electrochemical characteristics of titanium carbide derived carbon|1-ethyl-3-methylimidazolium tetrafluoroborate electrical double layer capacitors, ECS Trans. 25 (2010) 15.
4. T. Romann, E. Anderson, S. Kallip, H. Mändar, L. Matisen, E. Lust, Electroless deposition of bismuth on Si(111) wafer from hydrogen fluoride solutions, Thin Solid Films 518 (2010) 3690.
5. T. Romann, H. Mändar, K. Tõnurist, E. Lust, Modification of heavy metal surfaces with thiols, FMTDK converence, Tartu, Estonia, February 25–26, 2010.
6. T. Romann, E. Lust, Electrochemical properties of porous bismuth, In: Meeting Abstracts (CD): 216th ECS Meeting, Vienna, Austria, October 4–9, 2009, Abs. 3022.
7. T. Romann, M. Väärtnõu, A. Jänes, E. Lust, In situ infrared spectroscopic characterization of a bismuth-ethanol interface, Electrochim. Acta 53 (2008) 8166.

8. T. Romann, S. Kallip, V. Sammelselg, E. Lust, Bismuth microelectrode system with in situ renewable surface for electroanalysis and adsorption studies, Electrochem. Comm. 10 (2008) 1008.
9. T. Romann, M. Väärtnõu, E. Lust, In Situ Infrared Spectroscopic Studies of Water and Ethanol on Bismuth Single Crystal Surfaces, In: Cd of Abstracts: The 59th Annual Meeting of the International Society of Electrochemistry, Sevilla, Spain, September 6–13, 2008, Abs. s02-P-059**.**
10. T. Romann, E. Lust, Formation of the Bismuth Thiolate Compound Layer on Bismuth Surface, In: 5th Baltic Converence on Electrochemistry: Functional Materials in Electrochemistry – from Fundamental problems to Molecular Electronics and Modern Power Sources; Tartu, Estonia, 30 April – 3 May 2008, P-30.
11. Nerut, J.; Thomberg, T.; Härk, E.; Lust, K.; Jäger, R.; Kallip, S.; Kasuk, H.; Grozovski, V.; Romann, T.; Väärtnõu, M.; Lust, E. (2008). Adsorption kinetics and electroreduction of compex ions on the Bi(hkl) and Cd(0001) single crystal planes. In: 5th Baltic Conference on Electrochemistry: Functional Materials in Electrochemistry – from Fundamental problems to Molecular Electronics and Modern Power Sources; Tartu, Estonia; 30 April – 3 May, 2008, O-6.
12. T. Romann, E. Lust, Renewable Surface Microelectrode System for Research and Electroanalysis, In: Book of Abstracts: 6th Spring Meeting of the International Society of Electrochemistry, Foz do Iguacu, Brazil, 16–19 March, 2008, 74.
13. T. Romann, V. Grozovski, E. Lust, Formation of the bismuth thiolate compound layer on bismuth surface, Electrochem. Comm. 9 (2007) 2507.
14. T. Romann, M. Väärtnõu, E. Lust, In situ infrared spectroscopy characterization of bismuth-ethanol interface, In: Abstracts of Scientific Converence: 30th Estonian Chemistry Days; Tartu, Estonia; 16 November, 2007, 137.
15. Lust, E.; Grozovski, V.; Härk, E.; Jäger, R.; Kallip, S.; Kasuk, H.; Lust, K.; Nerut, J.; Romann, T.; Thomberg, T.; Väärtnõu, Kinetics of ionic and molecular adsorption and electroreduction mechanism of complex ions in relation to the surface structure of the Bi, Sb and Cd electrodes. 58th Annual Meeting of the International Society of Electrochemistry, Banff, Canada, September 9 to 14, 2007.
16. T. Romann, K. Lust, E. Lust, Adsorption of 1,6-hexanediol on Bi single crystal electrodes, Electrochim. Acta 52 (2007) 2612.

DISSERTATIONES CHIMICAE UNIVERSITATIS TARTUENSIS

1. **Toomas Tamm.** Quantum-chemical simulation of solvent effects. Tartu, 1993, 110 p.
2. **Peeter Burk.** Theoretical study of gas-phase acid-base equilibria. Tartu, 1994, 96 p.
3. **Victor Lobanov.** Quantitative structure-property relationships in large descriptor spaces. Tartu, 1995, 135 p.
4. **Vahur Mäemets.** The ^{17}O and ^{1}H nuclear magnetic resonance study of H_2O in individual solvents and its charged clusters in aqueous solutions of electrolytes. Tartu, 1997, 140 p.
5. **Andrus Metsala.** Microcanonical rate constant in nonequilibrium distribution of vibrational energy and in restricted intramolecular vibrational energy redistribution on the basis of slater's theory of unimolecular reactions. Tartu, 1997, 150 p.
6. **Uko Maran.** Quantum-mechanical study of potential energy surfaces in different environments. Tartu, 1997, 137 p.
7. **Alar Jänes.** Adsorption of organic compounds on antimony, bismuth and cadmium electrodes. Tartu, 1998, 219 p.
8. **Kaido Tammeveski.** Oxygen electroreduction on thin platinum films and the electrochemical detection of superoxide anion. Tartu, 1998, 139 p.
9. **Ivo Leito.** Studies of Brønsted acid-base equilibria in water and non-aqueous media. Tartu, 1998, 101 p.
10. **Jaan Leis.** Conformational dynamics and equilibria in amides. Tartu, 1998, 131 p.
11. **Toonika Rinken.** The modelling of amperometric biosensors based on oxidoreductases. Tartu, 2000, 108 p.
12. **Dmitri Panov.** Partially solvated Grignard reagents. Tartu, 2000, 64 p.
13. **Kaja Orupõld.** Treatment and analysis of phenolic wastewater with microorganisms. Tartu, 2000, 123 p.
14. **Jüri Ivask.** Ion Chromatographic determination of major anions and cations in polar ice core. Tartu, 2000, 85 p.
15. **Lauri Vares.** Stereoselective Synthesis of Tetrahydrofuran and Tetrahydropyran Derivatives by Use of Asymmetric Horner-Wadsworth-Emmons and Ring Closure Reactions. Tartu, 2000, 184 p.
16. **Martin Lepiku.** Kinetic aspects of dopamine D_2 receptor interactions with specific ligands. Tartu, 2000, 81 p.
17. **Katrin Sak.** Some aspects of ligand specificity of P2Y receptors. Tartu, 2000, 106 p.
18. **Vello Pällin.** The role of solvation in the formation of iotsitch complexes. Tartu, 2001, 95 p.

19. **Katrin Kollist.** Interactions between polycyclic aromatic compounds and humic substances. Tartu, 2001, 93 p.
20. **Ivar Koppel.** Quantum chemical study of acidity of strong and superstrong Brønsted acids. Tartu, 2001, 104 p.
21. **Viljar Pihl.** The study of the substituent and solvent effects on the acidity of OH and CH acids. Tartu, 2001, 132 p.
22. **Natalia Palm.** Specification of the minimum, sufficient and significant set of descriptors for general description of solvent effects. Tartu, 2001, 134 p.
23. **Sulev Sild.** QSPR/QSAR approaches for complex molecular systems. Tartu, 2001, 134 p.
24. **Ruslan Petrukhin.** Industrial applications of the quantitative structure-property relationships. Tartu, 2001, 162 p.
25. **Boris V. Rogovoy.** Synthesis of (benzotriazolyl)carboximidamides and their application in relations with *N*- and *S*-nucleophyles. Tartu, 2002, 84 p.
26. **Koit Herodes.** Solvent effects on UV-vis absorption spectra of some solvatochromic substances in binary solvent mixtures: the preferential solvation model. Tartu, 2002, 102 p.
27. **Anti Perkson.** Synthesis and characterisation of nanostructured carbon. Tartu, 2002, 152 p.
28. **Ivari Kaljurand.** Self-consistent acidity scales of neutral and cationic Brønsted acids in acetonitrile and tetrahydrofuran. Tartu, 2003, 108 p.
29. **Karmen Lust.** Adsorption of anions on bismuth single crystal electrodes. Tartu, 2003, 128 p.
30. **Mare Piirsalu.** Substituent, temperature and solvent effects on the alkaline hydrolysis of substituted phenyl and alkyl esters of benzoic acid. Tartu, 2003, 156 p.
31. **Meeri Sassian.** Reactions of partially solvated Grignard reagents. Tartu, 2003, 78 p.
32. **Tarmo Tamm.** Quantum chemical modelling of polypyrrole. Tartu, 2003. 100 p.
33. **Erik Teinemaa.** The environmental fate of the particulate matter and organic pollutants from an oil shale power plant. Tartu, 2003. 102 p.
34. **Jaana Tammiku-Taul.** Quantum chemical study of the properties of Grignard reagents. Tartu, 2003. 120 p.
35. **Andre Lomaka.** Biomedical applications of predictive computational chemistry. Tartu, 2003. 132 p.
36. **Kostyantyn Kirichenko.** Benzotriazole — Mediated Carbon–Carbon Bond Formation. Tartu, 2003. 132 p.
37. **Gunnar Nurk.** Adsorption kinetics of some organic compounds on bismuth single crystal electrodes. Tartu, 2003, 170 p.
38. **Mati Arulepp.** Electrochemical characteristics of porous carbon materials and electrical double layer capacitors. Tartu, 2003, 196 p.

39. **Dan Cornel Fara.** QSPR modeling of complexation and distribution of organic compounds. Tartu, 2004, 126 p.
40. **Riina Mahlapuu.** Signalling of galanin and amyloid precursor protein through adenylate cyclase. Tartu, 2004, 124 p.
41. **Mihkel Kerikmäe.** Some luminescent materials for dosimetric applications and physical research. Tartu, 2004, 143 p.
42. **Jaanus Kruusma.** Determination of some important trace metal ions in human blood. Tartu, 2004, 115 p.
43. **Urmas Johanson.** Investigations of the electrochemical properties of polypyrrole modified electrodes. Tartu, 2004, 91 p.
44. **Kaido Sillar.** Computational study of the acid sites in zeolite ZSM-5. Tartu, 2004, 80 p.
45. **Aldo Oras.** Kinetic aspects of dATPαS interaction with $P2Y_1$ receptor. Tartu, 2004, 75 p.
46. **Erik Mölder.** Measurement of the oxygen mass transfer through the air-water interface. Tartu, 2005, 73 p.
47. **Thomas Thomberg.** The kinetics of electroreduction of peroxodisulfate anion on cadmium (0001) single crystal electrode. Tartu, 2005, 95 p.
48. **Olavi Loog.** Aspects of condensations of carbonyl compounds and their imine analogues. Tartu, 2005, 83 p.
49. **Siim Salmar.** Effect of ultrasound on ester hydrolysis in aqueous ethanol. Tartu, 2006, 73 p.
50. **Ain Uustare.** Modulation of signal transduction of heptahelical receptors by other receptors and G proteins. Tartu, 2006, 121 p.
51. **Sergei Yurchenko.** Determination of some carcinogenic contaminants in food. Tartu, 2006, 143 p.
52. **Kaido Tämm.** QSPR modeling of some properties of organic compounds. Tartu, 2006, 67 p.
53. **Olga Tšubrik.** New methods in the synthesis of multisubstituted hydrazines. Tartu. 2006, 183 p.
54. **Lilli Sooväli.** Spectrophotometric measurements and their uncertainty in chemical analysis and dissociation constant measurements. Tartu, 2006, 125 p.
55. **Eve Koort.** Uncertainty estimation of potentiometrically measured ph and pK_a values. Tartu, 2006, 139 p.
56. **Sergei Kopanchuk.** Regulation of ligand binding to melanocortin receptor subtypes. Tartu, 2006, 119 p.
57. **Silvar Kallip.** Surface structure of some bismuth and antimony single crystal electrodes. Tartu, 2006, 107 p.
58. **Kristjan Saal.** Surface silanization and its application in biomolecule coupling. Tartu, 2006, 77 p.
59. **Tanel Tätte.** High viscosity $Sn(OBu)_4$ oligomeric concentrates and their applications in technology. Tartu, 2006, 91 p.

60. **Dimitar Atanasov Dobchev**. Robust QSAR methods for the prediction of properties from molecular structure. Tartu, 2006, 118 p.
61. **Hannes Hagu**. Impact of ultrasound on hydrophobic interactions in solutions. Tartu, 2007, 81 p.
62. **Rutha Jäger.** Electroreduction of peroxodisulfate anion on bismuth electrodes. Tartu, 2007, 142 p.
63. **Kaido Viht.** Immobilizable bisubstrate-analogue inhibitors of basophilic protein kinases: development and application in biosensors. Tartu, 2007, 88 p.
64. **Eva-Ingrid Rõõm.** Acid-base equilibria in nonpolar media. Tartu, 2007, 156 p.
65. **Sven Tamp.** DFT study of the cesium cation containing complexes relevant to the cesium cation binding by the humic acids. Tartu, 2007, 102 p.
66. **Jaak Nerut.** Electroreduction of hexacyanoferrate(III) anion on Cadmium (0001) single crystal electrode. Tartu, 2007, 180 p.
67. **Lauri Jalukse.** Measurement uncertainty estimation in amperometric dissolved oxygen concentration measurement. Tartu, 2007, 112 p.
68. **Aime Lust.** Charge state of dopants and ordered clusters formation in CaF_2:Mn and CaF_2:Eu luminophors. Tartu, 2007, 100 p.
69. **Iiris Kahn**. Quantitative Structure-Activity Relationships of environmentally relevant properties. Tartu, 2007, 98 p.
70. **Mari Reinik.** Nitrates, nitrites, N-nitrosamines and polycyclic aromatic hydrocarbons in food: analytical methods, occurrence and dietary intake. Tartu, 2007, 172 p.
71. **Heili Kasuk.** Thermodynamic parameters and adsorption kinetics of organic compounds forming the compact adsorption layer at Bi single crystal electrodes. Tartu, 2007, 212 p.
72. **Erki Enkvist.** Synthesis of adenosine-peptide conjugates for biological applications. Tartu, 2007, 114 p.
73. **Svetoslav Hristov Slavov**. Biomedical applications of the QSAR approach. Tartu, 2007, 146 p.
74. **Eneli Härk.** Electroreduction of complex cations on electrochemically polished Bi(*hkl*) single crystal electrodes. Tartu, 2008, 158 p.
75. **Priit Möller.** Electrochemical characteristics of some cathodes for medium temperature solid oxide fuel cells, synthesized by solid state reaction technique. Tartu, 2008, 90 p.
76. **Signe Viggor.** Impact of biochemical parameters of genetically different pseudomonads at the degradation of phenolic compounds. Tartu, 2008, 122 p.
77. **Ave Sarapuu.** Electrochemical reduction of oxygen on quinone-modified carbon electrodes and on thin films of platinum and gold. Tartu, 2008, 134 p.
78. **Agnes Kütt.** Studies of acid-base equilibria in non-aqueous media. Tartu, 2008, 198 p.

79. **Rouvim Kadis.** Evaluation of measurement uncertainty in analytical chemistry: related concepts and some points of misinterpretation. Tartu, 2008, 118 p.
80. **Valter Reedo.** Elaboration of IVB group metal oxide structures and their possible applications. Tartu, 2008, 98 p.
81. **Aleksei Kuznetsov.** Allosteric effects in reactions catalyzed by the cAMP-dependent protein kinase catalytic subunit. Tartu, 2009, 133 p.
82. **Aleksei Bredihhin.** Use of mono- and polyanions in the synthesis of multisubstituted hydrazine derivatives. Tartu, 2009, 105 p.
83. **Anu Ploom.** Quantitative structure-reactivity analysis in organosilicon chemistry. Tartu, 2009, 99 p.
84. **Argo Vonk.** Determination of adenosine A_{2A}- and dopamine D_1 receptor-specific modulation of adenylate cyclase activity in rat striatum. Tartu, 2009, 129 p.
85. **Indrek Kivi.** Synthesis and electrochemical characterization of porous cathode materials for intermediate temperature solid oxide fuel cells. Tartu, 2009, 177 p.
86. **Jaanus Eskusson.** Synthesis and characterisation of diamond-like carbon thin films prepared by pulsed laser deposition method. Tartu, 2009, 117 p.
87. **Margo Lätt.** Carbide derived microporous carbon and electrical double layer capacitors. Tartu, 2009, 107 p.
88. **Vladimir Stepanov.** Slow conformational changes in dopamine transporter interaction with its ligands. Tartu, 2009, 103 p.
89. **Aleksander Trummal.** Computational Study of Structural and Solvent Effects on Acidities of Some Brønsted Acids. Tartu, 2009, 103 p.
90. **Eerold Vellemäe.** Applications of mischmetal in organic synthesis. Tartu, 2009, 93 p.
91. **Sven Parkel.** Ligand binding to 5-HT_{1A} receptors and its regulation by Mg^{2+} and Mn^{2+}. Tartu, 2010, 99 p.
92. **Signe Vahur.** Expanding the possibilities of ATR-FT-IR spectroscopy in determination of inorganic pigments. Tartu, 2010, 184 p.